Identification and characterization of kinase-sparing aurora kinase A ligands for treatment of *TP53*-altered liver carcinomas

Dissertation

der Mathematisch-Naturwissenschaftlichen Fakultät

der Eberhard Karls Universität Tübingen

zur Erlangung des Grades eines

Doktors der Naturwissenschaften

(Dr. rer. nat.)

vorgelegt von

M. Sc. Melanie Henning

aus Augsburg

Tübingen

2022

Gedruckt mit Genehmigung der Mathematisch-Naturwissenschaftlichen Fakultät der Eberhard Karls Universität Tübingen.

Tag der mündlichen Qualifikation:	07.04.2022
Dekan:	Prof. Dr. Thilo Stehle
1. Berichterstatter:	Prof. Dr. Stefan Laufer
2. Berichterstatter:	Prof. Dr. Lars Zender

Declaration of previous data use

I declare, that the following data were already shown in the doctoral thesis of Dr. Dirk Flötgen, University of Tübingen, 2020, with the title “Design und Synthese konformationsändernder small molecules für die Aurora Kinase A als neuartige PPI Inhibitoren des AURKA/MYC-Komplexes in p53 defizientem HCC”.

FIGURE / TABLE	DATA GENERATION
FIGURE 5 E	Dr. Dirk Flötgen (Structures of LN3350 and LN3352)
TABLE 8 (PARTIALLY)	Melanie Henning
FIGURE 7 E	Melanie Henning (XTT), Katharina Bauer, AG Laufer (ADP-Glo^{TM}), Martin Schröder, AG Knapp (TSA)
FIGURE 8 B	ProQuinase
FIGURE 10 B AND C	Melanie Henning

Table of Contents

Abbreviations

°C	degree celsius
µL	microliter
µm	micrometer
µM	micromolar
ADP	adenosine diphosphate
AKI	AURKA kinase inhibitor
ARID1A	AT-rich interactive domain-containing protein 1A
ARID2	AT-rich interaction domain 2
ASH	alcoholic steatohepatitis
ATCC	American Type Culture Collection
ATP	adenosine triphosphate
AURKA	aurora kinase A
AURKB	aurora kinase B
AURKC	aurora kinase C
BAX	Bcl-2-associated X protein
BSA	bovine serum albumin
CCLE	cancer cell line encyclopedia
CDK1	cyclin-dependent kinase 1
cDNA	complementary DNA
CEP192	centrosomal protein of 192 kDa
CFU-GM	Colony-forming unit-granulocyte, macrophage
CIN	chromosome instability
CIP	calf intestinal alkaline phosphatase
CKAP5	cytoskeleton-associated protein 5
Co-IP	Co-immunoprecipitation
CTNNB1	catenin beta-1
d	day
DAPI	4',6-diamidino-2-phenylindole
DMEM	Dulbecco's Modified Eagle Medium
DMSO	dimethylsulfoxide
DOX	doxycycline
e.g.	exempli gratia
ED	effective dose
EDTA	ethylenediaminetetra-acetic acid
EGTA	ethylene glycol-bis(β-aminoethyl ether)-N,N,N′,N′-tetraacetic acid
FCS	fetal calf serum
FOXO	forkhead box protein O
h	hour
HBS	HEPES buffered saline
HBV	hepatitis B virus
HCC	hepatocellular carcinoma
HCV	hepatitis C virus
IARC	international agency for research on cancer
IC_{50}	half maximal inhibitory concentration
IF	immunofluorescence

IP	immunoprecipitation
LB	lysogeny broth
Mad2	mitotic arrest deficient 2
MCL1	induced myeloid leukemia cell differentiation protein
MDM2	E3 ubiquitin-protein ligase Mdm2
mg	milligram
min	minute
M phase	mitosis phase
MT	microtubule
MTD	maximum tolerated dose
MTOC	microtubule organizing center
mut	mutant
n	number
NaCl	sodium chloride
NAFLD	non-alcoholic fatty liver disease
NASH	nonalcoholic steatohepatitis
NEDD1	neural precursor cell expressed, developmentally down-regulated 1
NF-κB	nuclear factor kappa-light-chain-enhancer of activated B cells
nm	nanometer
nM	nanomolar
NOXA	phorbol-12-myristate-13-acetate-induced protein 1
ns	not significant
OE	overexpression
p	p-value
P21	cyclin-dependent kinase inhibitor p21
P38α	MAPK14, mitogen-activated protein kinase 14
PBS	phosphate buffered saline
PBST	phosphate buffered saline with tween
PCM	pericentriolar matrix
PCR	polymerase chain reaction
PFA	paraformaldehyde
PLA	proximity ligation assay
PLK1	polo-like kinase 1
PUMA	p53 upregulated modulator of apoptosis
PVDF	polyvinylidene difluoride
RanGTP	GTP-binding nuclear protein Ran
RB1	retinoblastoma protein 1
RHAMM	receptor for hyaluronan mediated motility
rpm	rounds per minute
R-spine	regulatory spine
RT	room temperature
SAC	spindle assembly checkpoint
SB	sleeping beauty
SCLC	small cell lung cancer
SDS-PAGE	sodium dodecyl sulphate polyacrylamide gel electrophoresis
TAE	tris-acetate-EDTA

TBS	tris-buffered saline
TBST	tris buffered saline with tween
TERT	telomerase reverse transcriptase
Tm	melting temperature
TNBC	triple negative breast cancer
TP53	tumor protein 53
TP63	tumor protein 63
TP73	tumor protein 73
TPX2	targeting-protein für Xklp2
TSA	thermal shift assay
TVDT	tumor volume doubling time
V	volt
VEGF	vascular endothelial growth factor
WB	western blot
wt	wildtype
XTT	2,3-Bis-(2-methoxy-4-nitro-5-sulfophenyl)-2H-tetrazolium-5-carboxanilide
γ-TuRC	γ-Tubulin ring complex

Summary

Hepatocellular carcinoma (HCC) represents a major and increasing health problem, however, the therapy options for advanced stage HCC are very limited. Recent studies highlight the use of conformation changing AURKA inhibitors, like MLN8237 and CD532, as novel treatment option of *TP53*-altered HCC. However, all existing AURKA inhibitors potently affect its kinase function, resulting in dose-limiting toxicities as shown in several clinical trials. To reduce such toxicities and thus enable the development of drugs with higher therapeutic index, we developed first-of-their-kind kinase-spearing AURKA-ligands which specifically modulate the AURKA conformation and interactome.

Specifically, using genetically defined murine HCC cell lines, I showed that the newly developed AURKA-ligands specifically kill *Trp53*-altered HCC cells with IC_{50} values in the low nanomolar range. This effect was independent of kinase inhibition, since neither the catalytic function of AURKA is reduced, nor that of any other of 320 tested wildtype kinases. In contrast to the clinically developed AURKA inhibitor MLN8237, neither non-tumorous cells nor liver cancer cells with *TP53* wildtype status were affected by treatment with Aurora-ligands, thus underlining their unprecedented therapeutic index.

Mechanistic analyses revealed, that the complex formation of AURKA and MYC was decreased by the AURKA-ligands, leading to MYC downregulation. However, stable MYC mutants showed that this downregulation was not responsible for the observed marked therapeutic effects. I found that the AURKA-ligands tethered the AURKA/TPX2 complex, thereby stabilizing both proteins resulting in an increase in AURKA activation. This robustly disturbed the mitotic spindle dynamics, leading to a continuous spindle assembly checkpoint activation, M phase arrest, mitotic defects and ultimately to cell death by mitotic catastrophe.

I could prove that also *TP53*-altered human HCC cell lines are sensitive towards AURKA-ligands and that they also show abnormal spindle formation upon treatment. Further, by probing a comprehensive panel of lung cancer cell lines I showed that *RB1* mutations in addition to *TP53* mutations further sensitize for AURKA-ligands.

Zusammenfassung

Das Hepatozelluläre Karzinom (HCC) stellt ein zunehmend großes Gesundheitsproblem dar, jedoch sind die Therapiemöglichkeiten für HCC im fortgeschrittenen Stadium sehr begrenzt. Ein kürzlich publizierter Behandlungsansatz beschreibt die Verwendung von Konformations-ändernden AURKA-Inhibitoren, MLN8237 und CD532, für die Behandlung von *TP53*-mutiertem HCC. Alle bisher entwickelten AURKA-Inhibitoren hemmen jedoch sehr effizient die Kinaseaktivität, was zu dosislimitierenden Toxizitäten führt, wie in mehreren klinischen Studien gezeigt wurde. Um diese Nebeneffekte zu minimieren, habe wir neuartige, nicht Kinase-hemmende AURKA-Liganden entwickelt, welche über eine Konformationsänderung des Proteins das AURKA-Interaktom modulieren.

Anhand genetisch-definierter muriner HCC-Zelllinien konnte ich zeigen, dass die neu entwickelten AURKA-Liganden, mit IC_{50}-Werten im niedrig-nanomolaren Bereich, *Trp53*-veränderte HCC-Zellen spezifisch abtöteten. Dieser Effekt war unabhängig von der Kinase-Hemmung, da weder die katalytische Funktion von AURKA, noch die einer anderen von 320 getesteten wildtyp Kinasen in bedeutender Weise beeinflusst wurde. Die Behandlung von nicht-tumorigenen Zelllinien zeigte, dass die AURKA-Liganden im Vergleich zum AURKA-Inhibitor MLN8237 einen höheren therapeutischen Index besaßen.

Mechanistische Analysen ergaben, dass die Komplexbildung von AURKA und MYC durch unsere AURKA-Liganden negativ beeinflusst wurde, was zu einer Herunterregulierung von MYC führte. Stabile MYC-Mutanten zeigten jedoch, dass diese Herunterregulierung nicht für die antitumorigene Wirkung unserer Liganden verantwortlich war. Stattdessen belegten meine Daten, dass der AURKA/TPX2-Komplex verstärkt und dadurch beide Proteine stabilisiert wurden. Dies, zusammen mit der induzierten AURKA-Aktivierung, stört die Dynamik der mitotischen Spindelbildung und führt zu einer kontinuierlichen „Spindle Assembly Checkpoint“-Aktivierung, einem M-Phasen Arrest, mitotischen Defekten und Zelltod durch „Mitotic Catastrophe“.

Ich konnte zeigen, dass auch *TP53*-veränderte humane HCC-Zelllinien sensitiv auf unseren AURKA-Liganden reagierten und die Behandlung ebenfalls eine abnormale

Spindelbildung induzierte. Durch Behandlung einer Reihe von humanen Lungenkrebszelllinien konnte ich außerdem nachweisen, dass *RB1* Mutationen *TP53*-mutierte Zellen zusätzlich für die Behandlung mit den AURKA-Liganden sensitivieren.

1 Introduction

1.1 Hepatocellular Carcinoma

1.1.1 Etiology and risk factors

Liver cancer represents a major and steadily increasing health problem and, according to the World Health Organization, is supposed to affect over 1 million patients annually by 2025[1]. It is the sixth most common cancer and the fourth leading cause for cancer-related deaths worldwide[1, 2].

Hepatocellular carcinoma (HCC) accounts for around 90% of liver cancer[1]. It develops mainly in patients suffering from liver disease like alcoholic steatohepatitis (ASH), non-alcoholic steatohepatitis (NASH), non-alcoholic fatty liver disease (NAFLD) and in particular in the context of liver cirrhosis[3, 4]. In addition to alcoholic and non-alcoholic steatohepatitis major risk factors for liver disease and HCC development include infections with Hepatitis B or C virus (HBV and HCV)[1, 2].

The highest incidence rates for HCC are present in Sub-Saharan Africa and Asia, due to the high number of HBV infections, which, despite an existing vaccine, still account for around 50% of HCC worldwide[5, 6]. In Western countries, HCV is the main cause for HCC development. However, the changed lifestyle will lead to a strong increase in NAFLD and NASH patients, thus, fatty liver disease will rapidly become the main cause for HCC in these countries[7-10].

1.1.2 Diagnosis and treatment options

The major problem with HCC diagnosis and treatment is the time point of tumor detection. The only potentially curative therapy options for HCC are surgical resection and liver transplantation[11]. However, these treatment options are restricted to patients with early stage HCC and due to the symptom-free course of disease at early stages it is estimated that around 50% of patients present with advanced HCC[1, 12]. Also the limited number of donor organs narrows the number of suitable patients for surgery[13, 14]. Since HCC is genetically very heterogeneous and resistant to standard chemotherapies, the treatment options for advanced HCCs are limited[15]. First-line

therapies approved for HCC are the multi-kinase inhibitors sorafenib and lenvatinib, or the anti-PD-L1 antibody atezolizumab (in combination with the anti-VEGF antibody bevacizumab)[16-18]. However, the survival benefit upon sorafenib treatment is on average only 2.8 months, due to the rapid development of therapy-resistance[16]. A noninferiority trial showed that lenvatinib confers an improved median overall survival compared to sorafenib of 1.2 months (13.6 months vs. 12.3 months). Although the side effects are different, both drugs are accompanied with grade 3–4 adverse events in about 50% of the treated patients[17]. Atezolizumab in combination with bevacizumab showed an elevated overall survival at 12 months of 67.2% compared to 54.6% with sorafenib[18]. However, both treatments provoked grade 3-4 adverse events in about 55% of patients[18].

The multi-kinase inhibitor regorafenib and the tyrosine kinase inhibitor cabozantinib were the first drugs approved for second-line therapy for patients after tumor progression upon sorafenib or lenvatinib treatment. They increased survival for another 2.8 and 2.2 months[19, 20]. Recently, also the VEGF receptor 2 inhibitor ramucirumab and the PD-1 immune checkpoint blocking antibody nivolumab were approved as second-line treatment options in the US[21, 22].

However, the modest prolongation of survival as well as the severe side-effects for all approved drugs show the need for novel therapeutic strategies.

1.1.3 Molecular pathogenesis

HCC develops in a background of chronic inflammation, fibrosis and aberrant hepatocyte regeneration. Although the liver harbors an extraordinary regeneration capacity, the sustained damage can favor cirrhosis and the accumulation of mutations and epigenetic alterations, leading to the formation of preneoplastic lesions which can progress to HCC[3]. The three most frequently activating mutations found in HCC are the telomerase reverse transcriptase (*TERT,* 60%), which is a recurrent insertion site for HBV, catenin beta-1 (*CTNNB1,* 30%) and the vascular endothelial growth factor (*VEGF*, 5-10%)[2]. Although the high mutation rate renders them attractive targets, TERT and CTNNB1 still remain undruggable. Therefore, HCC is one of the solid tumors with the fewest somatic mutations that can be targeted with molecular therapies[2, 23].

Interestingly, a study found that in 61% of the analyzed HCC aurora kinase A (AURKA) was overexpressed and that this correlates with high grade HCC and poor clinical outcome[24]. Since AURKA is an actionable protein, it therefore resembles a promising target for HCC therapy.

Inactivating mutations regularly found in HCC occur in *AXIN1* (10%), in AT-rich interactive domain-containing protein 1A (*ARID1A*, 10%), and in AT-rich interaction domain 2 (*ARID2*, 5%)[2]. The most frequently mutated tumor suppressor is the Tumor protein p53 (*TP53*, 30%), however, p53 is also not druggable to restore its tumor-suppressive function[2, 23].

1.2 The P53 tumor suppressor

1.2.1 Physiological function

P53, also called “guardian of the genome”, is a transcription factor which is regulated in a feedback loop by the E3 ubiquitin ligase MDM2, which keeps p53 levels low under normal cellular conditions[25-27]. Upon diverse stress stimuli, like DNA damage, replication stress or oncogene activation, MDM2 and p53 become phosphorylated, which prevents MDM2 binding and ubiquitination of p53, leading to p53 acetylation, stabilization and activation[28, 29]. The transactivation of p53 downstream targets can lead to the induction of DNA repair[30], cell cycle arrest[31, 32], senescence[33, 34] or apoptosis[35-38] (Figure 1).

P53-dependent cell cycle arrest is initiated upon DNA damage to allow for DNA repair or upon defective mitosis to prevent DNA re-replication[31, 39]. It is mainly mediated by induction of cyclin-dependent kinase inhibitor 1 ($p21^{Waf1/Cip1/Sdi1}$, in the following referred to as p21), which binds to the cyclin E/CDK2 and cyclin D/CDK4 complexes, thereby inhibiting CDK2 and CDK4[32, 40]. This blocks the phosphorylation of retinoblastoma protein 1 (RB1), preventing the dissociation of RB1 from the transcription factor E2F1. As a result, the expression of genes important for cell cycle progression and DNA replication are inhibited, leading to a G1 phase arrest[32].

A p53-dependent induction of p21 can also lead to a G2/M cell cycle arrest by inhibiting cyclin B/CDC2, however, other p53 targets might also be involved in preventing G2/M-transition[41]. In addition to halting the cell cycle and allowing for DNA repair, p53 also has direct functions in several DNA-repair mechanisms[30].

Upon excessive cell damage, p53 can also induce a stable or irreversible arrest, called senescence, however, reversibility is still under debate[42-44]. Senescent cells are characterized by morphological changes, chromatin remodeling, metabolic reprogramming, and secretion of senescence associated secretory phenotypes (SASP)[45]. The p53-dependent induction of senescence is dependent on p21, but also involves RB1[33, 46]. The senescent state ensures genomic integrity by preventing further proliferation of damaged cells[47].

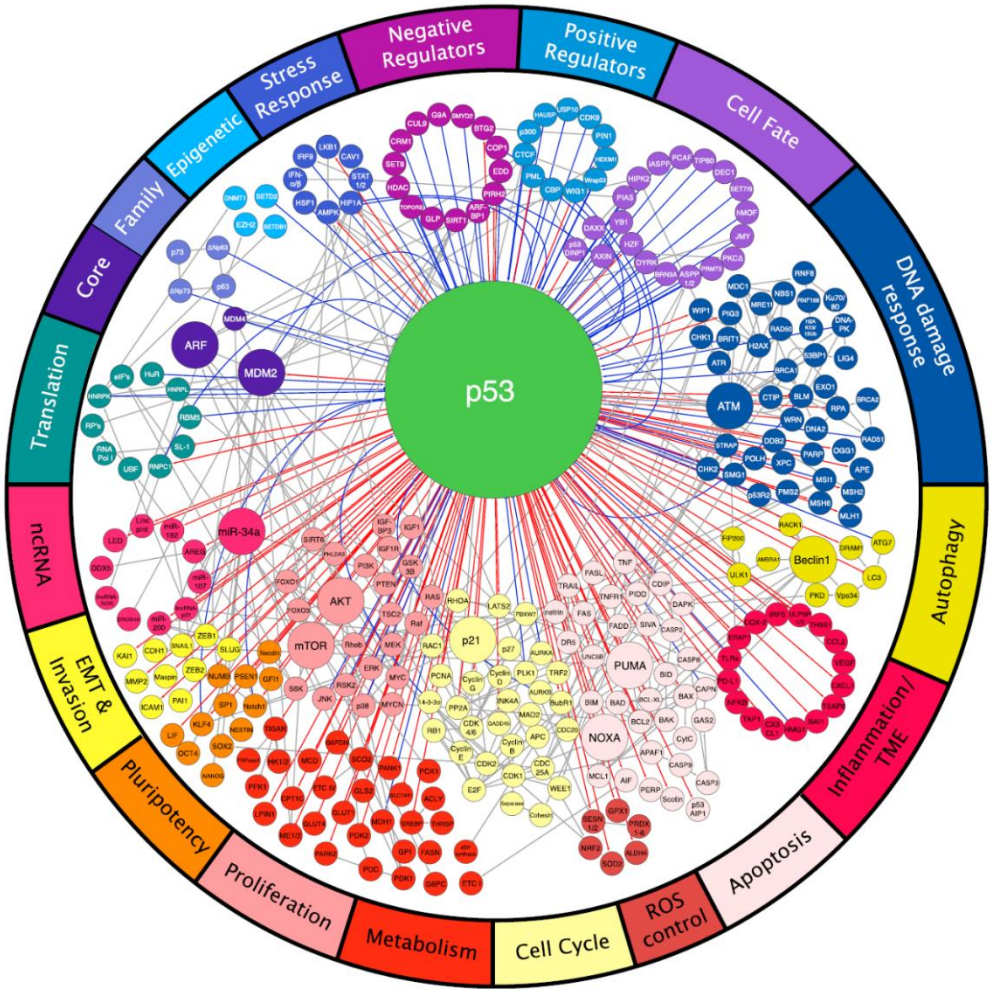

Figure 1: The p53 network. Overview of regulators (top) and biological processes (bottom) of p53. Each circle displays a gene, each line shows an interaction. Blue lines represent direct p53 inputs and red lines represent direct p53 outputs. Grey lines show interconnections of downstream pathways. Interactions are annotated as negative (T-bar), positive (arrow) or modifying (solid dot). (adapted from [48])

Another way of how p53 facilitates elimination of seriously damaged cells and prevention of chromosomal instability is the induction of apoptosis[35-38]. Thereby, p53 induces the B3 domain-only proteins Bcl-2-like protein 11 (BIM), p53 upregulated modulator of apoptosis (PUMA) and NOXA[49]. These pro-apoptotic factors inhibit the pro-survival proteins B-cell lymphoma-extra large (BCL-XL), B-cell lymphoma 2 (BCL-

2) and myeloid cell leukemia 1 (MCL1), thereby releasing the cell death effectors and Bcl-2-associated X protein (BAX) and Bcl-2 homologous antagonist killer (BAK). BAX and BAK then lead to the permeabilization of the mitochondrial outer membrane, which is followed cytochrome c release and apoptosome assembly. The apoptosome then recruits and activates caspase 9, which in turn activates caspase 3 and 7 leading to cell death[49].

Besides the induction of those three main outputs, p53 also has several non-canonical functions as summarized in Figure 1.

1.2.2 Role of p53 in development and treatment of cancer

TP53 is regarded as the most frequently mutated gene across tumors with a strong selective pressure for inactivating mutations. Although around 42% of all tumors carry a *TP53* mutation, the frequency and distribution show a huge variation across different tumor types, e.g. 95% of high grade serous ovarian carcinoma, 90% of small cell lung carcinoma (SCLC), 69.8% of head and neck squamous cell carcinoma and only 2.2% of renal clear cell carcinoma[50-52]. Most mutations of *TP53* are found to be missense mutations mainly located in the DNA binding core domain[50, 53]. These can lead to destabilization of p53 or disruption of DNA binding resulting in complete loss-of-function or selection-of-function[48]. However, also gain-of-function mutations can be found, allowing for neomorphic p53 outputs, e.g. the ability to inactivate other p53 family members like p63 or p73, thereby acting as an oncogene[54, 55]. Only around 25% are nonsense mutations or frame shift mutations leading to a truncated version of the p53 protein with impaired wildtype functions[48, 56]. Due to its importance in G1 and G2/M checkpoints, mutations of p53 facilitate the accumulation of further mutations and promote the generation and survival of aneuploid cells, as well as intratumoral heterogeneity[48]. Also, loss of functional p53 does not only impede DNA repair upon DNA damage, but can also impair the spindle assembly checkpoint (SAC) by derepressing MAD2, a member of the mitotic checkpoint complex (MCC), inducing chromosome miss-segregation and subsequent polyploidy or aneuploidy[57]. The accumulation of mutations and aneuploidy leads to loss of genomic integrity, as well as uncontrolled cell function and proliferation. The insufficient induction of senescence and apoptosis due to *TP53* loss further increases uncontrolled cell proliferation eventually resulting in tumor formation.

In vivo studies demonstrating that reinstatement of wildtype *TP53* efficiently eliminates cancer cells in lymphomas[58], soft tissue sarcomas[59], and liver carcinomas[60], render p53 a promising cancer target. Mutant non-functional *TP53* is often highly expressed in tumor tissue, raising the hope that a therapeutic strategy to refold it in order to reconstitute DNA binding and regain wildtype functions could lead to tumor cell death[52, 61, 62]. However, direct p53 targeting is difficult since the re-establishment of a mutated, inactive tumor suppressor is by far more challenging than the inactivation of an oncogene, e.g. a kinase. To date, several refolding small molecules have been tested in preclinical studies, including cysteine binding or zinc chelating compounds[52]. However, the underlying mechanism is often not fully understood and only two compounds have made it to clinical trials[52, 63, 64]. COTI-2, a 3rd generation thiosemicarbazone is currently in a clinical phase II trial (NCT02433626)[65-67]. However, it functions not only in p53-dependent ways but also via p53-independent redox homeostatic mechanisms[65-67]. Further, it is known that thiosemicarbazones have nonspecific cytotoxicity and affect iron metabolic pathways[65-67]. APR-246 is currently being tested in combination with azacitidine in a clinical phase III trial (NCT03745716) for the treatment of *TP53*-mutated myelodysplastic syndromes[67]. As a pro-drug, APR-246 is converted to the reactive methylene quinuclidinone (MQ) within the cell. MQ then covalently binds to surface-exposed cysteines of mutated, but also wildtype p53[68]. However, it was shown that MQ also functions at least partially via a mechanism independent of p53[69].

Besides the often unclear mode of action, specific mutations can induce different folding and need distinct small molecules for refolding, generating another level of complexity.

However, a study published by our group in 2016 could show that *TP53*-altered HCC harbor specific vulnerabilities that can be exploited therapeutically. One such "synthetic lethality" of *TP53*-altered HCC that we characterized is their dependency on AURKA[70].

1.3 Aurora Kinase A

1.3.1 Physiological function in mitosis

Aurora kinase A (AURKA) together with AURKB and AURKC belongs to the aurora kinase family of serine-threonine kinases. AURKA and AURKB have essential but distinct roles in mitosis, while AURKC primarily functions in meiotically-active germ

cells[71]. Accordingly, the expression levels of AURKA differ throughout the cell cycle, showing an upregulation at the end of S phase, peak in G2 and M phase and proteasome-mediated degradation after mitotic exit and in G1 phase[72]. The main functions of AURKA in mitosis include G2/M transition by ensuring timely mitotic entry, centrosome maturation, centrosome segregation and bipolar spindle assembly in order to ensure proper cell division[73, 74]. Although AURKA interacts with a big network of proteins, there are three main interaction partners that are regarded as core co-factors: Bora, centrosomal protein of 192 kDa (CEP192) and targeting protein for Xklp2 (TPX2) (see Figure 2). Those proteins, that lead to the formation of functionally distinct complexes, compete with each other for AURKA binding and are primarily responsible for the localization and activation of AURKA throughout mitosis[74].

The cytoplasmic cofactor Bora is able to bind AURKA and polo-like-kinase 1 (PLK1), one of the main downstream targets of AURKA, thereby rendering the activation loop of PLK1 accessible to AURKA[75, 76] (see Figure 2). Phosphorylation of Thr210 of PLK1 in G2 phase by AURKA ensures timely mitotic entry of the cell. Via several target proteins phosphorylated PLK1 then leads to the activation of CDK1, inducing the G2/M transition[73]. Then CDK1 phosphorylates Bora at Ser252 in a positive feedback loop, which promotes the binding of PLK1 to Bora and subsequent activation by AURKA[77]. However, PLK1 is able to phosphorylate Bora, leading to its ubiquitination via the $SCF^{\beta TrCP}$ E3 ubiquitin ligase and proteasome-mediated degradation upon mitotic entry[78]. This decrease of Bora protein levels might be essential to render AURKA free for complex formation with other co-factors important for centrosomal processes and spindle assembly.

CEP192, another AURKA core co-factor, is responsible for targeting and activating AURKA at centrosomes, leading to centrosome maturation and separation[79,80] (see Figure 2). Centrosomes, that function as microtubule organizing centers (MTOC), are non-membrane bound organelles, that play a role in spindle assembly, cell division, polarity and motality[79]. Depending on the cell cycle phase, they consist of one or two centrioles, which are surrounded by the pericentriolar matrix (PCM)[81]. The PCM contains proteins essential for microtubule (MT) nucleation and anchoring. Centrosome maturation is characterized by a substantial PCM expansion and increase in microtubule-nucleating capacity[82]. The subsequent centrosome separation creates two nascent spindle poles with nucleating microtubules, allowing for bipolar spindle formation[79]. Starting in the G2 phase, pericentrin-dependent recruitment of CEP192 to

the centrosomes triggers the accumulation of AURKA and PLK1 at centrosomes, which induces AURKA autophosphorylation at Thr288 and subsequent PLK1 activation through phosphorylation at Thr210[79, 83]. PLK1, in turn, phosphorylates CEP192 at several serine sites, creating docking-sites for the complex consisting of γ-tubulin ring complex and neural precursor cell expressed developmentally down-regulated gene 1 (γ-TuRC/NEDD1) and cytoskeleton associated protein 5 (CKAP5), initiating centrosome maturation, separation and centrosome-mediated MT nucleation[79, 83].

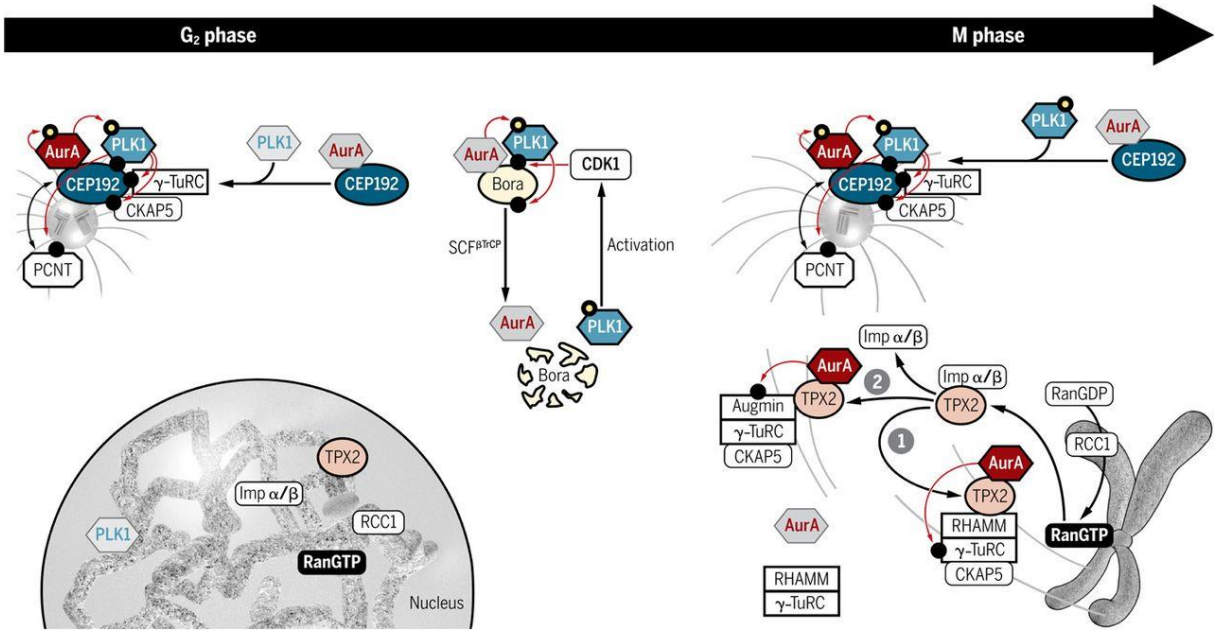

Figure 2: Functions of the AURKA core co-factors Overview of the main functions of AURKA in complex with its core co-factors Bora, CEP192 and TPX2 in G2 and M phase. Inactive forms are depicted in grey, active forms in color, phosphate groups are shown as black circles, activating phosphate groups as black circles with yellow center (adapted from [74])

TPX2, the third and best characterized core co-factor of AURKA is responsible for chromatin-mediated spindle assembly and targeting AURKA to the spindles[74, 84]. In the mitotic cytoplasm, TPX2 is inhibited through the binding to importin β and the importin α/β heterodimer. Upon nuclear envelope breakdown, RanGTP leads to the release of TPX2 from the importins, allowing TPX2 to interact with AURKA. This complex formation induces a kinase-independent activation of AURKA by stabilizing AURKA in an active conformation and preventing the dephosphorylation of Thr288 by the protein-phosphatase 1[85]. Additionally, binding of TPX2 targets AURKA to the spindle MTs, where the complex oligomerizes, and binds a complex consisting of receptor for hyaluronan-mediated motility (RHAMM) and γ-TuRC[86] (Figure 2). After AURKA-mediated phosphorylation, the complex becomes capable of initiating MT nucleation

for chromatin-driven spindle assembly[87, 88]. Besides this, the AURKA/TPX2 complex is also capable to induce spindle assembly by MT nucleation from preexisting MTs via the augmin/γ-TuRC complex[89] (Figure 2).

1.3.2 Role of AURKA in tumor development

Due to the essential role of AURKA in mitosis, AURKA overexpression was found to be oncogenic and promote tumorigenesis by favoring cell proliferation, metastasis, epithelial-mesenchymal transition and self-renewal of cancer stem cells[90, 91]. AURKA overexpression has been found in a wide range of tumor types and often correlates with a poor clinical outcome[90], e.g. in HCC[24], non-small lung cancer (NCSLC)[92, 93], bladder cancer[94], pancreatic cancer[95] and kidney cancer[90]. AURKA overexpression is mainly due to AURKA gene amplification, gene mutations, transcriptional or posttranslational modifications or inhibition of degradation (Figure 3). This can lead to supernumerary centrosomes, multipolar spindles, aneuploidy and resistance to apoptosis[72]. Increased AURKA activity can also overcome the prevention of G2/M transition upon DNA damage, which usually is mediated via AURKA inactivation[96]. Further, elevated AURKA levels are able to overcome spindle poison induced SAC[97, 98]. The abrogation of the SAC, activated upon abnormal mitotic spindle formation, favors tetraploidy by inducing cytokinesis failure or mitotic slippage. This normally activates the p53-dependent post-mitotic G1 checkpoint. However, in cells that lack p53, this checkpoint is not activated, thereby allowing for DNA endoreduplication, centrosome overamplification and subsequent aneuploidy[39, 99].

Interestingly, it was found that also the overexpression of a kinase-dead AURKA mutant leads to tetraploidization and centrosomal amplification[99], suggesting that not only the kinase-related functions, but also the catalytic-independent activities of AURKA might contribute to tumor development. In line with this, it was recently found that AURKA stabilizes the oncogenes N-MYC in neuroblastoma and MYC in HCC in a kinase-independent manner through direct binding, thereby supporting the tumor development and maintenance[70, 100].

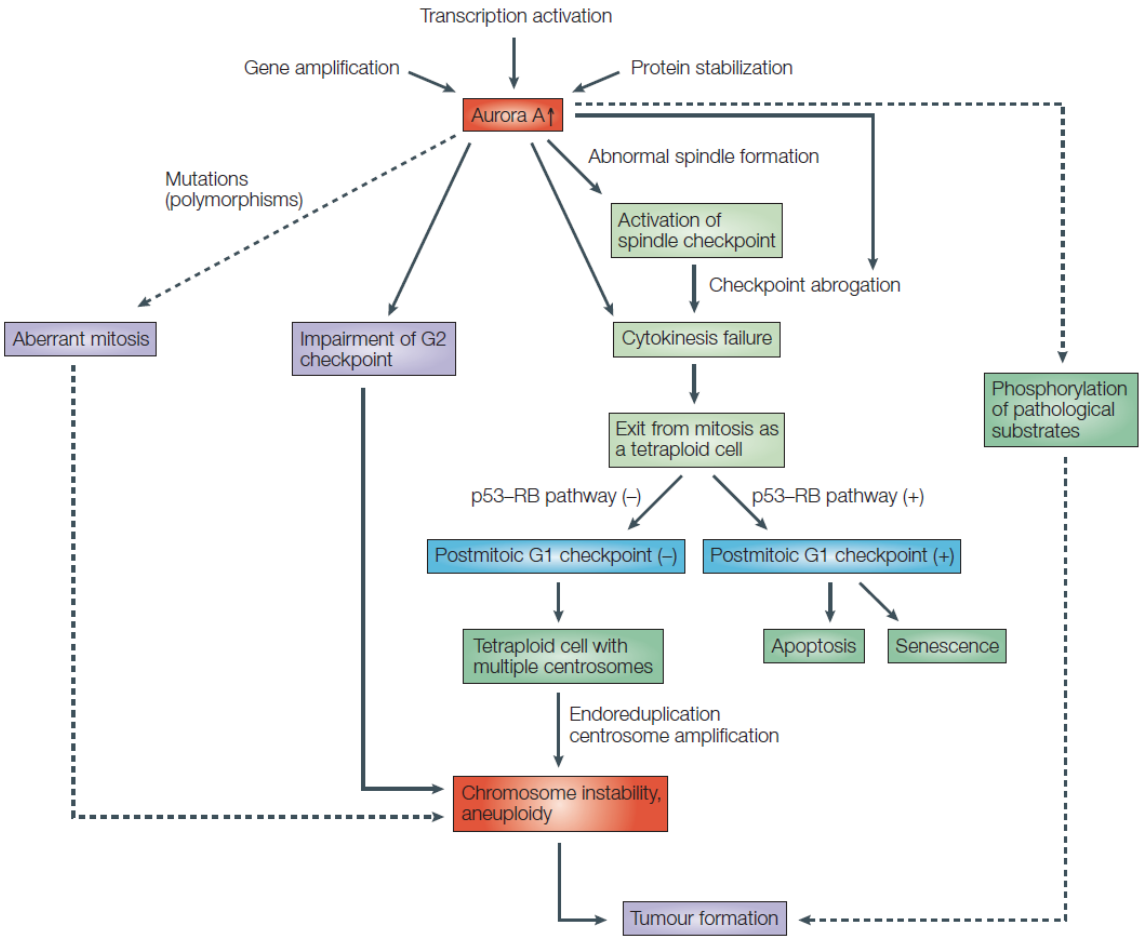

Figure 3: Tumorigenesis induced by AURKA overexpression (adapted from [91])

1.3.3 AURKA drug development for cancer treatment

To date, numerous 1st and 2nd generation inhibitors of AURKA (AKI) have been developed and were tested in preclinical studies or clinical trials (see Figure 4)[90, 101]. MLN8237, which is also known as alisertib, is the most advanced amongst the AKIs and the only one that has proceeded to clinical phase III trials[90]. In several phase II studies MLN8237 showed encouraging results, including objective response in breast and small cell lung cancer[102], advanced neuroendocrine prostate cancer with AURKA and N-MYC activation[103], relapsed or refractory peripheral T-cell non-Hodgkin lymphoma[104] and occasional responses in advanced sarcoma[105]. However, like all AURKA inhibitors of the 1st and 2nd generation, MLN8237 appears to have dose-limiting toxicities like (febrile) neutropenia, leukopenia, thrombocytopenia, somnolence and mucositis, so that it can only be administered 7 days is a 21-day cycle[106, 107]. The low therapeutic index observed for AURKA inhibitors might be caused by the additional inhibition of other members of the aurora kinase family, especially AURKB, as well as

other potential kinase-related off-targets, since the ATP binding pocket is highly conserved between kinases[108]. Although MLN8237 is widely regarded as a specific AURKA inhibitor, it was shown that the IC_{50} ratio in NCI-H446 cells of AURKB to AURKA inhibition with 13 is rather low[109]. Therefore, the newly developed and highly selective AURKA inhibitor LY3295668, with an AURKB/AURKA ratio of 2370 in NCI-H446, is a promising candidate for an improved therapeutic index[109]. However, since AURKA represents an essential kinase, whose inhibition itself targets a myriad of signaling pathways (see Figure 4), it remains questionable, if inhibitors of its catalytic activity will ever have a satisfying therapeutic window.

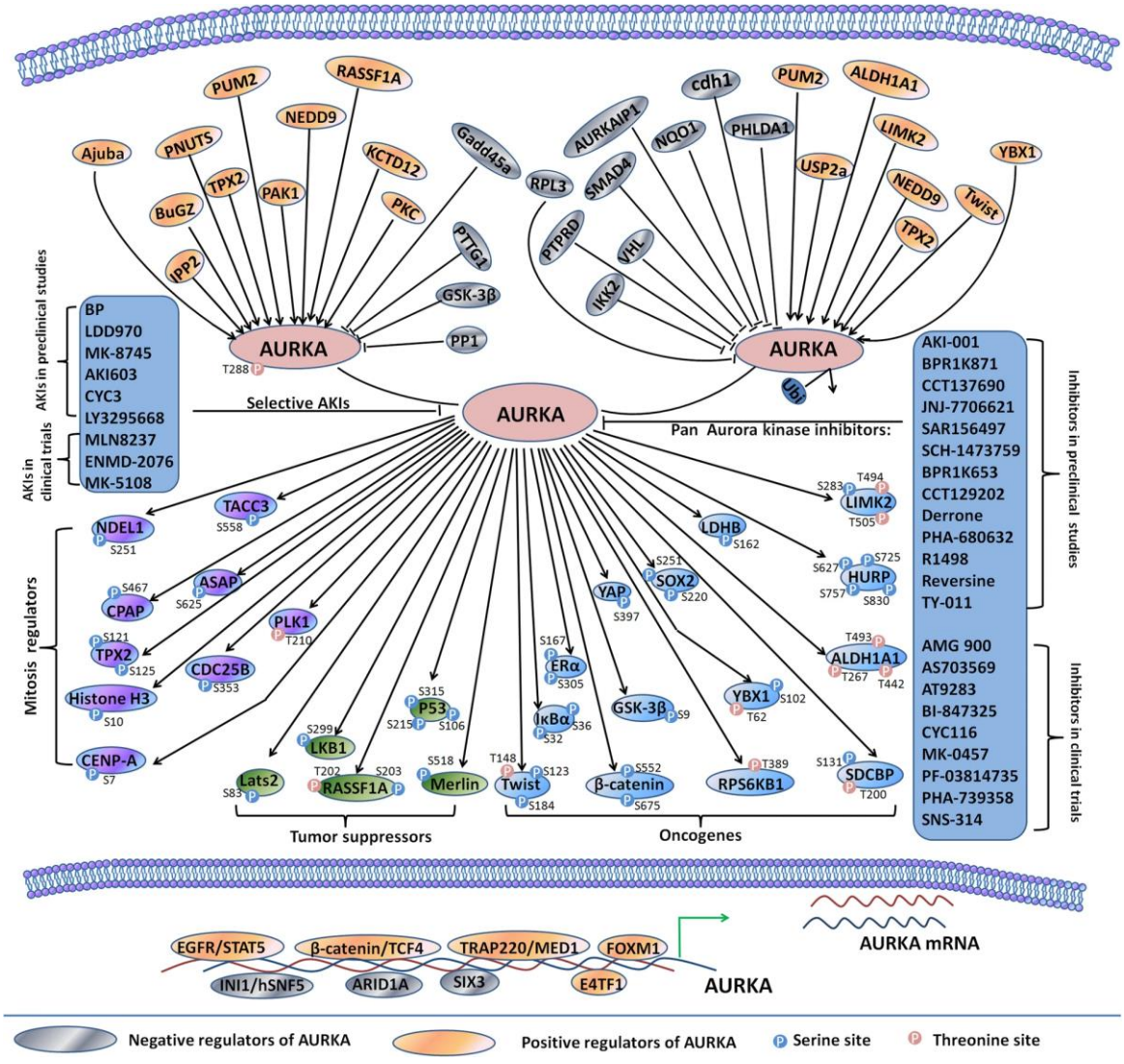

Figure 4: Overview of AURKA kinase inhibitors and interacting proteins. Shown are selective AURKA inhibitors (left side) and pan aurora kinase inhibitors (right side) in preclinical and clinical studies, as well as the network of AURKA interacting proteins (adapted from[90])

Interestingly, the AURKA inhibitors CD532 and most probably also MLN8237, additionally to the kinase inhibition, induce a change in the native conformation of AURKA[110, 111]. This shift was shown to prevent the binding of N-MYC and MYC to AURKA in a kinase-independent manner, thereby inducing the proteasome-mediated degradation of the two MYC proteins[70, 110, 111]. In contrast to normal AURKA inhibitors, those conformation changing compounds suppress the growth of *MYCN* amplified neuroblastoma and *Trp53*-deficient HCC *in vitro* and *in vivo* [70, 110]. These observations suggest, that the modulation of the AURKA interactome by targeting AURKA's conformation, rather than inhibiting the kinases catalytic function, might serve as a new strategy for compound development, that promises an excellent therapeutic index.

1.4 Aim of the study

AURKA represents an attractive target for cancer therapy. However, although clinical trials for AURKA inhibitors showed promising results, it became clear that the catalytic inhibition of AURKA leads to dose-limiting toxicities[101].

In order to overcome these limitations first-of-their-kind kinase-spearing AURKA-ligands specifically targeting the AURKA interactome were developed.

The first aim of my study was to determine the efficacy and selectivity of the newly developed kinase-spearing AURKA-ligands in genetically defined *Trp53* null and wildtype murine HCC cell lines. Then, I set out to analyze if the AURKA-ligands possess an improved therapeutic index compared to the kinase inhibitor MLN8237 by probing non-malignant cells. Further, I wanted to elaborate if AURKA/MYC interactions are responsible for the inhibitory effects of the newly developed AURKA-ligands or other proteins of the AURKA interactome. The next step was to identify the effects on mitosis and spindle architecture upon alteration of these interactions in the *Trp53* null and wildtype murine HCC cell lines. Then, I aimed to work out the role of *Trp53* for the sensitivity of cells towards the AURKA-ligands. I then set out to analyze if human HCC cell lines do also respond to the AURKA-ligands and if other tumor entities are sensitive to the newly developed treatment. Finally, I aimed to examine the pharmacologic properties of the AURKA-ligands.

2 Material and Methods

2.1 Material

2.1.1 Chemicals

If not stated differently, all chemicals and solutions used in this study were supplied by AppliChem, Biosciences, Carl Roth, Fermentas, GE Healthcare, Invitrogen, Life Technologies, Merck, Millipore, Promega, Peqlab, Serva and Sigma Aldrich.

2.1.2 Enzymes

All restriction enzymes, DNaseI, calf intestinal alkaline phosphatase (CIP) and T4-DNA-ligase were purchased from NEB (New England Biolabs).

2.1.3 Kits

The following kits were used in this study

Table 1: Kits used in this study

Kit	Company
DC-Protein Assay	Biorad
Plasmid Maxi Kit	Qiagen
QIAquick Gel Extraction Kit	Qiagen
Duolink™ In Situ PLA® Probe Anti-Mouse PLUS	Sigma Aldrich
Duolink™ In Situ PLA® Probe Anti-Rabbit MINUS	Sigma Aldrich
Duolink™ In Situ Detection Reagents Red	Sigma Aldrich
Duolink™ In Situ Wash Buffers, Fluorescence	Sigma Aldrich
ADP-Glo™ Kinase Assay	Promega
Aurora A Kinase Enzyme System	Promega
XTT	Invitrogen
Clarity Western ECL Substrate	Biorad

2.1.4 Buffers and Solutions

The following buffers were used in this study (Table 2). All buffers were prepared using deionized water.

Table 2: Buffers and solutions used in this study

Buffer/Solution	Composition
HBS (2x)	12 mM Dextrose, 10 mM KCl (best out of pH 6.96; 7.00; 7.04; 7.08)
Laemmli-buffer (4x)	200 mM Tris/HCl (pH 6.8), 8% SDS, 20 mM DTT, 40% glycerol, 0.33% bromophenol blue
DNA loading buffer (5x)	0.25% orange G, 15% (w/v) Ficoll type 400
LB-medium	1 l H_20, 20 g LB-powder, 50 mg/l ampicillin
Cell lysis buffer	20 mM TrisHCl (pH 7.5), 150 mM NaCl, 1 mM Na_2EDTA, 1 mM EGTA, 1% Triton X-100, 1 x Complete mini® (Roche), 1 x PhosSTOP® (Roche)
PBS (10x)	100 mM Na_2HPO_4*$2H_2O$, 20 mM KH_2PO_4, 1.37 M NaCl, 27 mM KCl (pH 7.4)
PBST	0.1% Tween 20 in PBS
Permeabilization-buffer	5% BSA, 0.2% Triton X-100, 0.1% Tween 20 in TBS
PFA in PBS	4% PFA in PBS (pH 7.4)
SDS-running buffer (10x)	250 mM Tris Base, 1.92 M Glycine, 1% SDS
TAE (50x)	2 M Tris Base (pH 8.5), 1 M glacial acetic acid, 50 mM EDTA
TBS (10x)	500 mM Tris-HCl, (pH 7.4), 1500 mM NaCl
TBST	0.1% Tween 20 in TBS
Transfer buffer	48 mM Tris-HCl (pH 8.3), 39 mM Glycine, 20% Methanol, 0.037% SDS
Immunofluorescence antibody solution	1% BSA, 0.1% Tween 20 in TBS
Co-IP Lysis Buffer	PBS + 1% Triton X-100, 1 x Complete mini® (Roche), 1 x PhosSTOP® (Roche)
Co-IP elution buffer	250 mM Tris-HCl pH 6.8, 4% SDS, 25% glycerol, 0.02% bromophenol blue, 100 mM DTT

2.1.5 Cell Culture Media

The following cell culture media were used in this study:

Table 3: Media used in this study

Medium	Supplements
DMEM	10% FCS (PAN Biotech), 1 mM sodium pyruvate, 0.1 mM Non-Essential Amino Acids Solution, 1 x Penicillin/Streptomycin
DMEM (NIH 3T3)	10% Calf Bovine Serum (ATCC), 1 x Penicillin/Streptomycin
DMEM (BNL CL.2)	10% FCS (PAN Biotech), 1 x Penicillin/Streptomycin
RPMI-1640	10% FCS (PAN Biotech), 1 x Penicillin/Streptomycin
Waymouth's MB 752/1 Medium	10% FCS (PAN Biotech), 1 x Penicillin/Streptomycin
McCoy's 5a Medium	10% FCS (PAN Biotech), 1 x Penicillin/Streptomycin
Eagle's Minimum Essential Medium	10% FCS (PAN Biotech), 1 x Penicillin/Streptomycin

If not mentioned elsewise, the media and supplements were purchased from Life Technologies, California, USA.

2.1.6 Antibodies

The following antibodies were used in this study:

Table 4: Antibodies used in this study

Primary antibodies

Antigen	Catalog name	Species	Supplier	Application	Dilution
Vinculin	V9131	mouse	Sigma Aldrich	WB	1:10000
α-Tubulin	NB100-690	mouse	Novus Biologicals	IF	1:1000
MYC	ab32072	rabbit	Abcam	WB IF, PLA	1:1000 1:200
MYC (pT58)	ab28842	rabbit	Abcam	WB	1:1000
AURKA	ab13824	mouse	Abcam	WB IF, PLA	1:1000 1:200
AURKA	NBP1-51843	rabbit	Novus Biologicals	WB IF	1:1000 1:200

Pan pAurora	2914S	rabbit	Cell Signaling	WB	1:1000
TPX2	NB5000-179	rabbit	Novus Biologicals	WB IF	1:1000 1:200
PLK1	PA5-96158	rabbit	Thermo Fisher	WB	1:1000
PLK1 (pThr210)	ab155095	rabbit	Abcam	WB	1:1000
FLAG	F1804	mouse	Sigma Aldrich	Co-IP	0.75µg
MCL1	5453S	rabbit	Cell Signaling	WB	1:1000
p38α MAPK	9218s	rabbit	Cell Signaling	WB	1:1000
p38 MAPK (pT180, Y182)	4511s	rabbit	Cell Signaling	WB	1:1000
Cleaved caspase 3	9661	rabbit	Cell Signaling	WB	1:1000

Secondary antibodies:

Antigen	**Name**	**Species**	**Supplier**	**Application**	**Dilution**	**Conjugation**
Anti-mouse	115-035-062	goat	Dianova	WB	1:10000	Peroxidase
Anti-rabbit	111-035-045	goat	Dianova	WB	1:10000	Peroxidase
Anti-rabbit	A-11034	goat	Invitrogen	IF	1:10000	Alexa 448
Anti-mouse	A-11032	goat	Invitrogen	IF	1:10000	Alexa 594

2.1.7 Oligonucleotides

The following Oligonucleotides were used in this study:

Table 5: Primers used for cloning and sequencing

Cloning of FLAG-tagged *Aurka* in RT3GcDPIR	
Name	Sequence
FLAG_fw_new	TTAGCGATCGCCATGGACTACAAAGACGATGA
FLAG-AURKA_rev_new	ATCTGGCGCGCCCTAAGATGATTTGCTGGTTG
Cloning of FLAG-tagged *Tpx2* in RT3GcDPIR	
TPX2_fw	TGAAGGAATTCGGTACCATGTCACAAGTCCCTACTAC
TPX2_rev	GCACTCGAGCTACTGGAACCGAGTGGA
FLAG_fw_new	TTAGCGATCGCCATGGACTACAAAGACGATGA
FLAG-TPX2_rev	ATCTGGCGCGCCCTA CTG GAA CCG AGT GGA

Sequencing primer	
GFP_for	CATGGTCCTGCTGGAGTTCG

2.1.8 Plasmids

For stable transduction of doxycycline inducible cDNA in cell lines the retroviral vector including TRE3G promotor, EGFP sequence, P2A site, PGK promotor, puromycin resistance cassette, IRES and an rtTA3 coding sequence (RT3GP2APIR) was used, which contained the cDNA for *CXCR4*. The RT3GP2APIR backbone was cloned by Dr. Aylin Yigitliler under the supervision of Dr. Florian Heinzmann by using the RT3GEPIR vector[112], which was kindly provided by Prof. Dr. Johannes Zuber. The RT3GP2APIR plasmid containing *CXCR4* cDNA was cloned by Dr. Marco Seehawer.

2.1.8.1 Cloning FLAG-tagged *Aurka* in RT3GP2APIR

The sequence for FLAG-tagged *Aurka* was taken from the pEZ-M11 vector including the murine *Aurka* transcript variant 1 containing a FLAG-tag at the N-terminus (EX-Mm05501-M11, GeneCapoeia). In a polymerase chain reaction (PCR) using the primers FLAG_fw_new and FLAG-AURKA_rev_new (Table 5) the FLAG-tagged *Aurka* sequence was amplified and then digested with AsisI and AscI. The RT3GP2APIR was digested with AsisI and MluI to cut out the *CXCR4* cDNA and replace it with the FLAG-tagged *Aurka* insert.

2.1.8.2 Cloning FLAG-tagged *Tpx2* in RT3GP2APIR

The sequence for *Tpx2* was taken from the PCMV6-Kan/Neo vector containing the murine *Tpx2* transcript variant 2 (MC202638, Origene). In order to introduce a N-terminal FLAG-tag, the *Tpx2* sequence was PCR amplified using the primers TPX2_fw and TPX2_rev (Table 5) and cut with KpnI and XhoI. The pEZ-M11 vector containing the murine *Aurka* transcript variant 1 with a N-terminal FLAG-tag (2.1.8.1) was digested with KpnI and XhoI and ligated with the TPX2 insert in order to replace *Aurka* with *Tpx2*. Using the Primers FLAG_fw_new and FLAG-AURKA_rev_new (Table 5) the FLAG-tagged *Tpx2* sequence was PCR amplified and digested with AsisI and AscI.

The RT3GP2APIR was digested with AsisI and MluI to cut out the *CXCR4* cDNA and replace it with the FLAG-tagged *Tpx2* insert.

2.1.9 Bacteria

For plasmid production Subcloning Efficiency DH5α Competent *Escherichia coli* cells (Invitrogen) were used.

2.1.10 Cell lines

The following cell lines were used in this study. For medium composition see Table 3.

Table 6: Cell lines used in this study

Cell line	Source	Culture Medium	Freezing Medium
NMP53$^{-/-}$ (murine HCC, *Nras^{G12V};Myc^{OE};Trp53$^{-/-}$*)	Dauch et al., 2016	DMEM complete	90% FCS + 10% DMSO
NMP19$^{-/-}$ (murine HCC, *Nras^{G12V};Myc^{OE};Cdkn2A$^{ARF-/-}$*)	Dauch et al., 2016	DMEM complete	90% FCS + 10% DMSO
NP53$^{-/-}$ MYC^{wt} lines 1-3 (murine HCC, *Nras^{G12V};MYC^{OE};Trp53$^{-/-}$*)	generated by Dr. Ramona Rudalska	DMEM complete	90% FCS + 10% DMSO
NP53$^{-/-}$ MYC^{T58A} lines 1-3 (murine HCC, *Nras^{G12V};MYC$^{T58A\ OE}$;Trp53$^{-/-}$*)	generated by Dr. Ramona Rudalska	DMEM complete	90% FCS + 10% DMSO
NMP19$^{-/-}$x53$^{-/-}$ (murine HCC, *Nras^{G12V};Myc^{OE};Cdkn2A$^{ARF-/-}$;Trp53$^{-/-}$*)	generated by Dr. Ramona Rudalska	DMEM complete	90% FCS + 10% DMSO
Hep3B	ATCC: HB-8064	DMEM complete	90% FCS + 10% DMSO
Huh7	kindly provided by Prof. Dr. Zucman-Rossi	DMEM complete	90% FCS + 10% DMSO
HLF	kindly provided by Prof. Dr. Zucman-Rossi	DMEM complete	90% FCS + 10% DMSO
HLE	kindly provided by Prof. Dr. Zucman-Rossi	DMEM complete	90% FCS + 10% DMSO
HepG2	ATCC: HB-8065	DMEM complete	90% FCS + 10% DMSO
JHH1	kindly provided by Prof. Dr. Zucman-Rossi	DMEM complete	90% FCS + 10% DMSO

NCI-H446	ATCC: HTB-171	RPMI-1640 complete	95% culture medium + 5% DMSO
DMS-53	ATCC: CRL-2062	Waymouth's MB 752/1 medium complete	95% culture medium + 5% DMSO
NCI-H69	ATCC: HTB-119	RPMI-1640 complete	95% culture medium + 5% DMSO
NCI-H1299	ATCC: CRL-5803	RPMI-1640 complete	95% culture medium + 5% DMSO
Calu-1	ATCC: HTB-54	McCoy's 5a Medium complete	95% culture medium + 5% DMSO
COR-L279	Sigma Aldrich: 96020724	RPMI-1640 complete	95% culture medium + 5% DMSO
A549	kindly provided by Prof. Dr. Lauer	RPMI-1640 complete	90% FCS + 10% DMSO
NCI-H226	kindly provided by Prof. Dr. Lauer	RPMI-1640 complete	90% FCS + 10% DMSO
NCI-H23	kindly provided by Prof. Dr. Lauer	RPMI-1640 complete	90% FCS + 10% DMSO
NCI-H460	kindly provided by Prof. Dr. Lauer	RPMI-1640 complete	90% FCS + 10% DMSO
NIH 3T3	ATCC: CRL-1658	DMEM (NIH 3T3)	90% Calf Bovine Serum + 10% DMSO
BNL CL.2	ATCC: TIB-73	DMEM (BNL CL.2)	90% FCS + 10% DMSO
Phoenix-ECO	ATCC: CRL-3214	DMEM complete	90% FCS + 10% DMSO

2.2 Cell culture

2.2.1 Standard cell culture

All cells were incubated at 37°C with 7.5% CO_2 in a water-saturated atmosphere. They were maintained in modified DMEM, RPMI-1640, McCoy's 5a Medium, Eagle's Minimum Essential Medium or Waymouth's MB 752/1 Medium (2.1. Materials). Cells

were split by adding 0.05% trypsin/EDTA solution (Gibco). For storage, around 1 x 10^6 cells were frozen in 1ml freezing medium (90% FCS and 10% DMSO or 95% culture medium and 5%DMSO) at -80°C. Cells were thawed in a water bath at 37°C and seeded in a 10cm^2 dish.

2.2.2 Production of retroviral particles

Retroviral particles were produced using ecotropic phoenix cells. At around 70% confluency a 6-well plate was pre-incubated with 25 µM chloroquine for 15 min at 37°C. 5 µg of plasmid was mixed with 12.5 µL 2M $CaCl_2$ and filled up with water to 100 µL. The Plasmid/$CaCl_2$ mixture was then drop wise added to 100 µL of 2 x HBS buffer while constantly producing air bubbles to receive a precipitate. After 5 min incubation at RT, the mix was drop wise added to the cells. Media was refreshed after 12 h and the supernatant was harvested after another 24 h and filtered through a 0.45 µm filter.

2.2.3 Infection of cells

Cells were grown to 15-30% confluency and pre-incubated with 10 µg/mL polybrene for 15 min before 1.5 mL of viral supernatant were added per 6-well. After 48 h cells were selected with 4-6 µg/mL puromycin for another 48 h

2.2.4 Colony formation assay

Cells were seeded at a density of 50.000 cells per 6-well and next day treated with a 2-fold dilution series of the indicated compounds or the highest corresponding DMSO concentration. After 5 days cells were fixed with a 10% formaldehyde solution for 30 min, washed once with water, stained with a 0.5% crystal violet solution for 30 min and washed twice with water.

2.2.5 XTT assay

Cells were seeded in a 96-well plate and next day treated with a 2-fold dilution series of the compounds. As controls cells were treated with DMSO according to the highest compound concentration (negative control) or 1.5 mM chloroquine (positive control).

3-5 days after treatment the XTT assay was conducted according to the manufacturer's instructions. Absorbance was measured with the Infinite M Plex plate reader (Tecan) at 450 nm. Each measurement was conducted in triplicates and the IC_{50} was calculated with GraphPad Prism using variable slope nonlinear regression, with DMSO treated cells resembling 100% cell viability and chloroquine treated cells resembling 0% cell viability.

2.2.6 Cell cycle analysis

For the determination of the cell cycle state of cells a propidium iodide staining with subsequent flow cytometry analysis was conducted. For this, 1 x 10^6 cells were harvested and centrifuged at 1200 rpm for 5 min. After washing the pellet with PBS cells were again centrifuged at 1200 rpm for 5 min. The pellet was resuspended in 250 µL PBS and fixed by adding 750 µL ice cold 100% ethanol dropwise while vortexing. After incubation overnight, cells were centrifuged at 1200 rpm for 5 min, washed once with 1% BSA in PBS, pelleted again at 1200 rpm for 5 min and resuspended in 1mL PBS with 50 µg/mL propidium iodide and 250 µg/mL RNase. After incubation overnight at 4°C, cell cycle was measured using FacsCanto II with DIVA software version 8.0.1 (BD Biosciences) and analyzed with FlowJo version 10 (Tree Star).

2.2.7 Immunofluorescence staining (IF) on cells

Cells were plated on 8-well Tissue Culture Chambers (Sarstedt), incubated overnight and treated as indicated. Cells were then fixed with either 4% PFA at 4°C for 10 min or 100% methanol at -20°C for 10 min. After washing the cells three times with TBST, permeabilization buffer (see 0) was added for 60 min at RT on a shaker. Cells were washed once with TBST and incubated with the primary antibody in 1% BSA in TBST for another 60 min at RT on a shaker. After washing three times with TBST, the cells were incubated with a secondary antibody, which was fluorescent dye-labelled, together with 1 µg/mL DAPI in 1% BSA in TBST for 60 min at RT on a shaker in the dark. After washing three times with TBST, the slide was mounted with VECTASHIELD HardSet mounting medium with DAPI (Vector Laboratories) using a coverslide.

2.2.8 Proximity ligation assay (PLA)

PLAs were performed to detect protein-protein interactions. 50.000 cells were seeded on round 12 mm glass slides placed in 6-well plates. After incubation overnight, cells were treated with the indicated compounds or DMSO and fixed for 10 min in 100% methanol at -20°C. Glass slides were removed from the 6-well plates and cells permeabilized with TBS + 0.3% Triton X-100 for 5 min. After washing with PBS and blocking with 5% BSA in TBST for 30 min, slides were incubated with primary antibodies in 1% BSA in TBST for 120 min at RT and washed three times with PBS for 5 min. After a 20 min pre-incubation of the two PLA probes at RT (diluted 1:10 in 1% BSA in TBST), slides were incubated with probes for 60 min at 37°C in a humidified chamber. Slides were washed three times with 1x wash buffer A for 5 min and incubated with ligase solution (ligase diluted 1:40 in 5x ligase buffer and ddH_2O) for 60 min at 37°C in a humidified chamber. After washing the slides two times for 5 min, they were incubated with polymerase solution (polymerase diluted 1:80 in 5x polymerase buffer and ddH_2O) light protected for 2 h at 37°C in a humidified chamber. Slides were washed two times in 1x wash buffer B for 10 min and once in 0.01x wash buffer B for 1 min and mounted on a cover slip using Duolink i*n situ* Mounting Medium with DAPI. Nail polish was used to seal the edges. PLA foci were visualized with an Olympus BX63 microscope equipped with an Olympus DP80 camera, 60x objective and 10x eyepiece (600-fold magnification). Foci were annotated to the cells with the closest nucleus (DAPI). Significance was calculated using Graph Pad Prism and the nonparametric Mann Whitney test.

2.3 Molecular biology techniques

2.3.1 Polymerase chain reaction (PCR)

To amplify DNA fragments a PCR was conducted using CloneAmp HIFI PCR MM (2x) (Takara). Specifically designed primers were used to add additional restriction sites (***Table 5***). PCR was conducted as follows (X= melting temperature):

Component	Amount
H_2O (RNase/DNase-free)	Ad up to 50µL
Takara CloneAmp HIFI PCR MM (2x)	25 µL
Forward Primer (10µM)	3 µL
Reverse Primer (10µM)	3 µL
Template	100 ng

PCR program		
94 °C	2 min	
94 °C	10 sec	} 25-35 cycles
X °C	20 sec	
72 °C	1 min per kb	
72 °C	2 min	
4 °C	∞	

2.3.2 DNA digestion with restriction enzymes

5 µg of DNA was digested with 0.5 µL restriction enzyme (NEB) and 2 µL of the corresponding buffer (NEB) in a total volume of 20 µL for 2 h at 37°C. The DNA fragments were purified via gel electrophoresis and/or column as described in 2.3.4.

2.3.3 Dephosphorylation of DNA fragments

For dephosphorylation of digested plasmid backbones 2 µL calf intestinal alkaline phosphatase (CIP) (NEB) and 2 µL CutSmart reaction buffer (NEB) were added to the backbone to a total volume of 20 µL. The mix was incubated at 37°C for 2 h and purified as described in 2.3.4.

2.3.4 DNA-Purification

After every cloning step, DNA was purified. If size separation was needed, the sample was run in an agarose gel electrophoresis. Purification was done with the QIAquick Gel Extraction Kit (Qiagen) according to the manufacturer's instructions.

2.3.5 Ligation of DNA fragments

DNA fragments were ligated by using 0.5 µL T4-ligase (NEB) and 1µL ligase buffer (NEB) in a total volume of 10 µL. The amount of backbone and insert was calculated with the following formula: $\mathrm{m(insert)} = \frac{\mathrm{bp(Insert)}}{\mathrm{bp(backbone)}} * 6 * 100\ \mathrm{ng}$. Ligation was performed either at 16°C for 2-4 h or overnight with increasing temperatures ranging from 4°C to RT.

2.3.6 Agarose gel electrophoresis

To determine the size of DNA-fragments, first gels with 1-2% agarose and around 0.01% ethidium bromide in 1x TAE buffer were cast. The sample was diluted in DNA loading buffer and loaded on the gel, together with the 1kb DNA ladder or the peqGOLD low range DNA ladder (Peqlab). Samples were separated for 30 min at 120 V in 1x TAE buffer and analyzed under UV light. If needed, the correct band was cut out of the gel and purified using the QIAquick Gel Extraction Kit (Qiagen).

2.3.7 Measuring DNA concentration

DNA concentrations were measured using NanoDrop1000 (PEQLAB) and 1 µL of the solution.

2.3.8 Bacteria transformation

Plasmid solutions were mixed with Subcloning Efficiency DH5α cells in a 1:10 ratio and incubated 5-30 min on ice. To induce transformation the mix was heat-shocked for 20 sec at 42°C followed by 2 min incubation on ice. The solution was plated on a LB-agar plate containing either ampicillin or neomycin and incubated overnight at 37°C.

2.3.9 Plasmid preparation from bacterial cultures

For high yield maxi-preparations 400 mL LB-medium containing ampicillin or neomycin were inoculated with a single bacteria colony and incubated overnight at 37°C in a shaker. For plasmid isolation the MaxiPrep Kit from Qiagen was used according to the manufacturer’s instructions.

For low yield mini-preparations 5mL LB-medium containing ampicillin or neomycin were inoculated with a single bacteria colony and incubated overnight at 37°C in a shaker. Bacteria were harvested by centrifugation with 4000 rpm for 5 min, resuspended in 200 µL P1 buffer (Qiagen), lysed with 200 µL P2 buffer (Qiagen) for 5 min and neutralized with 200 µL P3 buffer (Qiagen). The solution was centrifuged for 10 min at 13.000 rpm and 500 µL of supernatant were transferred into a new reaction tube. After 400 µL isopropanol were added, the samples were centrifuged for 15 min at 13.000 rpm. The pellet was washed with 70% ethanol, centrifuged at 13.000 rpm for 5 min and the supernatant discarded. The pellet was air-dried and resuspended in 30 µL RNase/DNase-free water. If necessary DNA was sent to Seqlab/Microsynth (Göttingen) for Sanger sequencing.

2.3.10 DNA sequencing

Sanger sequencing of DNA was done by Seqlab/Microsynth (Göttingen) with specific sequencing primers according to the company's instructions.

2.4 Biochemical methods

2.4.1 Protein isolation

For isolating proteins, cells were washed with PBS and collected in Lysis buffer (see 0) mixed with 8M Urea at a 5:1 ratio. The sample was sonicated on ice for 10 min using the GT Sonic 3L Sonicator. After 10 min centrifugation at 13.000 rpm at 4°C, supernatant was transferred into a new reaction tube.

2.4.2 Measuring of protein concentration

The measurement of protein concentrations was conducted using the DC Protein Assay (Biorad) according to the manufacturer's instructions. Absorbance was measured with the Infinite M Plex plate reader (Tecan) at 690 nm.

2.4.3 Sodium dodecyl sulphate polyacrylamide gel electrophoresis (SDS-PAGE)

To separate protein samples according to their molecular weight SDS-PAGE was conducted using the Mini-PROTEAN Tetra Vertical Electrophoresis Cell device (Biorad). After casting the SDS-gels as described in ***Table 7***, 10-25 µg of protein sample was mixed with Laemmli-Buffer (4x), denaturized at 95°C for 10 min and loaded on the gel. To determine the size of the protein band the pre-stained protein marker Spectra Multicolor Broad Range Protein Ladder or High Range Protein Ladder (Thermo Scientific) was used. The gel was run in 1x SDS running buffer at 90 V in the stacking gel and at 120 V in the separation gel.

Table 7: Composition of the SDS gel

10% separation gel (2 gels)		**5% stacking gel (2 gels)**	
Water, deionized	6.1 mL	Water, deionized	3.1 mL
Tris-HCl buffer (1.5M, pH8.8)	3.7 mL	Tris-HCl buffer (1M, pH 6.8)	1.25 µL
Acrylamide/Bis-acrylamide (37.5:1)	4.9 mL	Acrylamide/Bis-acrylamide (37.5:1)	1.34 mL
10% SDS	150 µL	10% SDS	0.5 mL
10% APS	75 µL	10% APS	25 µL
TEMED	10 µL	TEMED	5 µL

2.4.4 Western blot

Western blot was conducted using a wet blot device (Biorad). After activating PVDF membranes in methanol for 1 min, PVDF membranes, Whatman papers and gels were incubated in transfer buffer (see 0) for 5 min. The blotting cassette was assembled accordingly and protein transfer was done at 100 V for 70 min at 4°C. Membranes were blocked with 5% BSA or 5% milk in TBST for 1 h at RT and incubated with a primary antibody against the protein of interest in TBST overnight at 4°C. After washing the samples three times with TBST for 5-10 min each, they were incubated for 1 h at RT with HRP-conjugated secondary antibody. Then, membranes were washed three times with TBST for 5-10 min each and specific signals were visualized using Clarity Western

ECL Substrate (Biorad), the ChemiDoc Imaging System (Biorad) and the software Image Lab 5.2.1 (Biorad).

2.4.5 Co-Immunoprecipitation (Co-IP)

After washing once with cold PBS, cells were collected in Co-IP lysis buffer and incubated on ice for 15 min. After centrifugation for 10 min at 13.000 rpm at 4°C supernatant was collected in a new reaction tube. 1 mg of protein was incubated in a new reaction tube with 3 µg of FLAG-antibody and 30 µL Dynabeads Protein G (Thermo Fisher) in a total volume of 1 mL. After incubation overnight at 4°C on a rotation wheel, beads were washed three times with Co-IP lysis buffer for 5 min at 4°C on a rotation wheel and transferred into a new reaction tube. After separating beads from supernatant, proteins were eluted with 35 µL Co-IP elution buffer for 10 min at 70°C. 10 µL of Co-IP sample were loaded on an SDS-gel and analyzed with SDS-PAGE and western blot. As input control, 15 µg protein of initial supernatant mixed with Laemmli-buffer (4x) was used.

2.4.6 ADP-Glo™ assay

For determination of kinase inhibition (IC_{50}) of the compounds, the ADP-Glo™ Kinase Assay (Promega) and the Aurora A Kinase Enzyme System (Promega) were used. The assay was performed according to the manufacturer's instructions in a 384-well format by using 1.4 ng/µL Aurora A, 25 mM ATP and 0.1 µg/µL MBP substrate. To generate a dose-response curve a 1:3 serial dilution of the compounds was tested starting from 1 µM. Kinase was pre-incubated for 10 min with compound, before substrate mix containing MBP and ATP was added. After 60 min ADP-Glo reagent was added and incubated for another 60 min. Afterwards detection reagent was added and incubated for 30 min before luminescence was measured with an integration time of 500 ms by using a Filter Max F5 multi-mode microplate reader (Molecular Devices). As a negative control, the reaction was performed with MBP, ATP and Aurora A only. The positive control was performed with inactive Aurora A (boiled for 10 min), MBP and ATP. Each measurement was conducted in quadruplicates and the IC_{50} was calculated with GraphPad Prism using slope nonlinear regression, with the negative

control resembling 0% kinase inhibition and the positive control resembling 100% kinase inhibition.

2.5 Co-IP and mass spectrometry (LC-MS/MS)

For Co-IP assays of FLAG-tagged AURKA, cells stably expressing DOX-inducible FLAG-AURKA were grown in DMEM SILAC media (PAN Biotech) lacking arginine and lysine. SILAC medium was supplemented with penicillin/streptomycin (100 U/mL, PAN), dialyzed FBS (10% (v/v), PAN) and stable isotope-encoded arginine and lysine. 'Light' SILAC medium was supplemented with L-[12C6,14N2] lysine (Lys0) and L-[12C6,14N4] arginine (Arg0) (Cambridge Isotope Laboratories), 'medium' SILAC media with L-[2H4] lysine (Lys4) and L-[13C6] arginine (Arg6) and 'heavy' SILAC media L-[13C6,15N2] lysine (Lys8) and L-[13C6,15N4] arginine (Arg10).

For pool 1, FLAG-AURKA expression was induced in cells cultured in medium and heavy SILAC medium for 24 h. Afterwards, 50 ng/mL nocodazole was added to all three conditions (light, medium and heavy SILAC) for 6 h. Then, cells were washed once with PBS and medium was replaced, thereby adding DMSO to cells in light and medium SILAC medium, and LN3352 to cells in heavy SILAC medium for 2 h. Co-IP was then performed as described in 2.4.5. The SILAC Co-IP eluates were then mixed in the ration of 1:1:1 (light:medium:heavy). For pool 2, the procedure was repeated, with adding LN3352 to the medium SILAC sample and DMSO to light and heavy SILAC samples.

The preparation of protein samples from Co-IP experiments for liquid chromatography-MS (LC-MS/MS) was done using in-gel digestion. Both, the preparation and the LC-MS/MS analysis were performed by the Proteome Center Tübingen (PCT). The samples were boiled at 70°C for 10 min and proteins were separated on a NuPAGE Bis-Tris 4-12% gradient gel (Thermo Fisher Scientific). After staining the samples with Coomassie Brilliant Blue solution, the gel lanes were cut into fragments and washed three times with washing buffer (5 mM AmBiC, 50% (v/v) ACN). Then 10 mM dithiothreitol (DTT) in 20 mM AmBiC was added and incubated at 56°C for 1 h. After adding iodoacetamide (55 mM (IAA) in 20 mM AmBiC) for 30 min at RT, gel pieces were washed with washing buffer and dehydrated with 100% (v/v) ACN and vacuum centrifugation for 10 min. After protein digestion with trypsin (12.5 ng/mL in 20 mM AmBiC, Promega Corporation) at 37°C overnight, the peptides were extracted with 3%

(v/v) TFA in 30% (v/v) ACN, followed by 0.5% (v/v) acetic acid in 80% (v/v) ACN and 100% (v/v) ACN. All extracts were mixed, concentrated by vacuum centrifugation and purified on C18 StageTips.

LC-MS/MS runs were performed as described priviously[113]. For this study, peptides were eluted with a 60 min gradient and full MS scans were acquired with a resolution of 60,000 and within a mass range of m/z 200 to 2,000 (AGC target 3e6, maximum IT 20 ms). For higher-energy collisional dissociation (HCD), the 12 most intensive peptides were selected and MS/MS spectra were recorded with a resolution of 30,000 (AGC target 1e5, maximum IT 110 ms).

The raw data files were processed as described priviously[113], using the Uniprot *Mus Musculus* (UP000000589_10090_complete_2020-02_13) database. Carbamidomethylation of cysteine (C) was set as fixed modification and oxidation of methionine was defined as variable modifications.

Co-IP targets of interest were selected based on their intensity values and the significance, represented by the false discovery rate (FDR) values. Interesting targets were to be significantly detected in the LN3352/DMSO samples (H/M in the pool 1 and pool 2, FDR < 0.1) and not significantly detected in the CO-IP control channels DMSO/noDOX (H/L in the pool 1 and M/L in the pool 2, FDR >0.05). Selected target also had higher raw intensity values in the LN3352 treated samples in comparison to the DMSO controls, as an additional filtering on condition.

2.6 Statistics

Normal distribution was calculated using the D'Agostino & Pearson test or, if not possible, the Shapiro-Wilk test. For calculation of significance, student's t test, Mann-Whitney test and one-way ANOVA were used. If significant differences by ANOVA were found, group wise comparison was performed (Holm-Sidak's multiple comparison test). All statistical tests were considered statistically significant when *P* was below 0.05. Statistical analysis was performed using GraphPadPrism (v.8.4.0).

3 Results

3.1 Development and characterization of kinase-sparing AURKA-ligands

Inhibiting AURKA represents a promising cancer therapy, however, the dose-limiting toxicities of existing drugs due to catalytic inhibition is a major obstacle. To overcome this limitation and improve the therapeutic index, in collaboration with Dr. Dirk Flötgen and Juliander Reiner from the group of Prof. Dr. Stefan Laufer, as well as Dr. Tatu Pantsar, we set out to develop kinase-sparing AURKA-ligands that target essential kinase and signal transduction independent functions of AURKA via the modulation of AURKA's interactome. It was shown that the interaction of N-MYC and MYC, two AURKA binding partners, can be modulated by a small subfraction of AURKA inhibitors, MLN8237 and CD532, leading to their destabilization and degradation[70, 111] (Figure 5 A and B). This modulation was induced due to a conformational shift in AURKA[70, 111] and we reasoned that this shift could serve as a starting point for the development of kinase-sparing AURKA-ligands. Unpublished molecular dynamics simulations, performed by Dr. Tatu Pantsar, suggested that the AURKA/MYC interaction site is located next to the αC-helix, where AURKA's regulatory spine (R-spine) is connected[70] (Figure 5 C). We hypothesized that compounds targeting this R-spine region would lead to the desired conformational alteration of AURKA (Figure 5 D). Since the R-spine of AURKA and the p38α MAP-kinase differ only in one amino acid (glutamine in AURKA, leucine in p38α), I wanted to address this hypothesis by screening a focused library of proprietary p38α MAP-Kinase inhibitors which were equipped with R-spine-interacting moieties, previously generated in the group of Prof. Dr. Laufer[114, 115]. Since the library consisted of p38α targeting small molecules, the resulting hits were structurally adapted towards AURKA. For this the initial hits generated from type 1 ½ p38α MAP-Kinase inhibitors were split into different modules (hinge binder, linker fragment, aromatic core structure and an R-spine interacting moiety) (Figure 5 E). Different modules were merged to yield *in silico* libraries with which a virtual screening was conducted by Dr. Tatu Pantsar. The resulting hits were synthesized and further optimized by Dr. Dirk Flötgen and Juliander Reiner. The combination of structural features that were expected to have a strong effect on the kinases R-spine region with a simplified version of CD532's hinge binding moiety

resulted in both, highly active and selective, amphosteric inhibitors (like LN3352) and AURKA-ligands (like LN3350)[116].

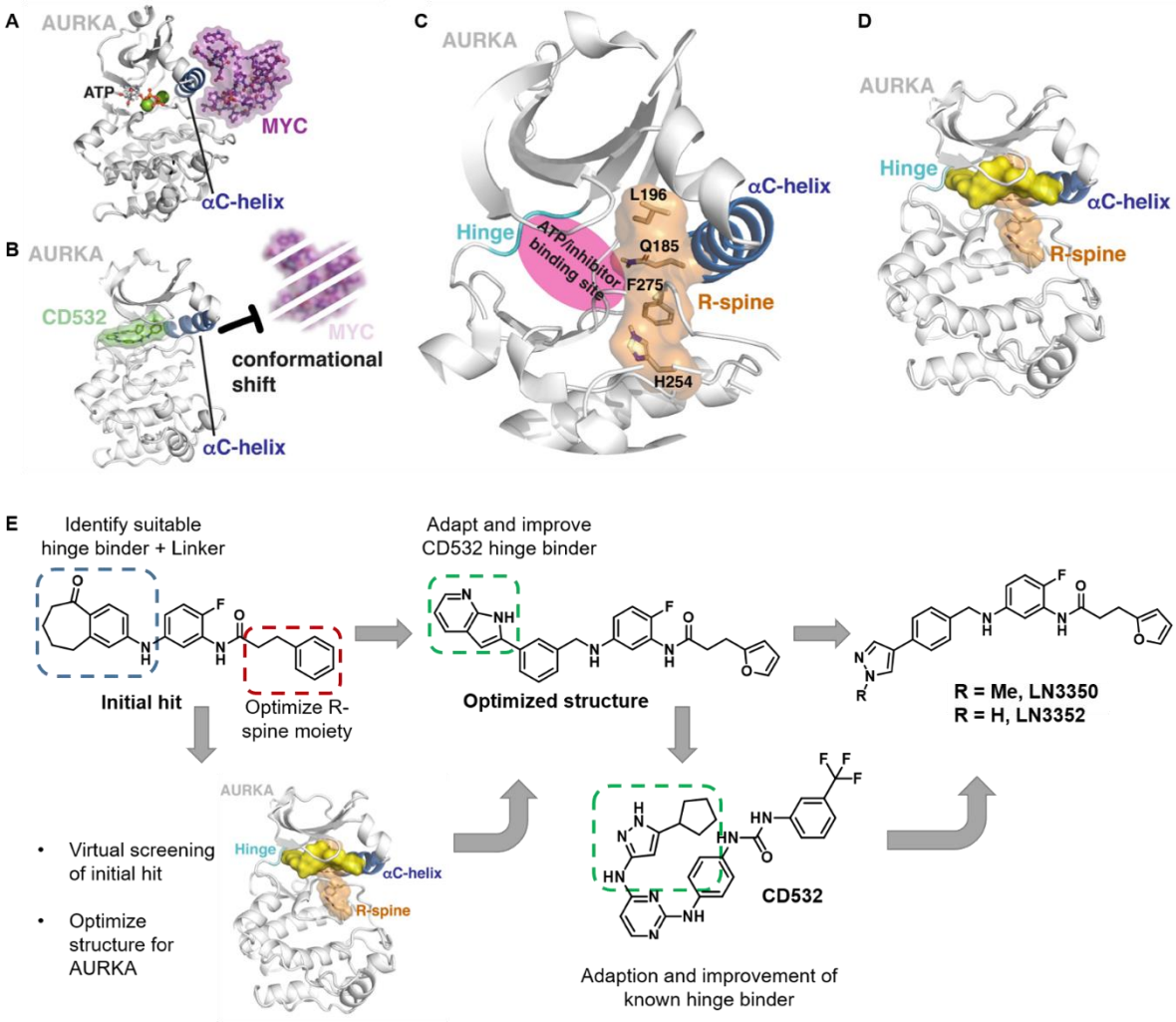

Figure 5: A-D) Molecular dynamics simulation approach for the development of kinase-spearing AURKA-ligands. (A) AURKA in complex with MYC (purple). (B) Small molecules, like CD532 (green), change AURKA's conformation, thereby preventing MYC binding. (C) *In silico* predictions suggest the interaction site of AURKA/MYC being located next to the αC-helix (blue), where the R-spine (orange) is anchored. (D) Compounds targeting the R-spine region presumably lead to the desired conformational alteration of AURKA (generated by Dr. Tatu Pantsar) **E)** Development approach for improved small molecules that target AURKA without inhibiting its intrinsic kinase activity. In a first step virtual screening of an *in silico* library based on an initial hit resulted in potent compounds. For further optimization the hinge binding moiety of a kinase inhibitor (CD532) with known AURKA conformation disrupting properties was adapted and improved to spare kinase activity (generated by Dr. Dirk Flötgen).

During iterative cycles of testing and improvement, the small molecules were optimized by Dr. Dirk Flötgen, Juliander Reiner and Dr. Tatu Pantsar. To simultaneously guide the improvement strategy with functional *in vitro* data, I tested the compounds via colony formation screening assays (Figure 6 A). Therefore, I used the murine HCC cell lines *Nras*^{G12V}*;Myc*^{OE}*;Trp53*$^{-/-}$ (in the following called NMP53$^{-/-}$) and *Nras*^{G12V}*;Myc*^{OE}*;Cdkn2a*$^{ARF-/-}$ (in the following called NMP19$^{-/-}$), where the selectivity of conformation-changing AURKA inhibitors to kill NMP53$^{-/-}$ cells was described before[70].

Table 8: Exemplary depiction of generated compounds tested in the colony formation assay. Shown are the effective doses (ED) of each compound in NMP53$^{-/-}$ and NMP19$^{-/-}$ cells, as well as the calculated selectivity towards NMP53$^{-/-}$ cells.

Name	ED [nM] NMP53$^{-/-}$	ED [nM] NMP19$^{-/-}$	Selectivity	Name	ED [nM] NMP53$^{-/-}$	ED [nM] NMP19$^{-/-}$	Selectivity
LN3177	4000	4000	equal	**LN3354**	2000	2000	equal
LN3178	2000	2000	equal	**LN3355**	> 2000	> 2000	n.d.
LN3179	1000	2000	2-fold	**LN3356**	1000	1000	equal
LN3180	> 4000	> 4000	n.d.	**LN3357**	500	1000	2-fold
LN3198	> 4000	> 4000	n.d.	**LN3358**	> 2000	> 2000	n.d.
LN3199	2000	4000	2-fold	**LN3359**	125	250	2-fold
LN3200	2000	4000	2-fold	**LN3360**	125	125	equal
LN3201	2000	4000	2-fold	**LN3361**	> 2000	> 2000	n.d.
LN3274	> 4000	> 4000	n.d.	**LN3362**	500	1000	2-fold
LN3275	> 4000	> 4000	n.d.	**LN3363**	1000	> 1000	n.d.
LN3276	4000	8000	2-fold	**LN3364**	500	> 1000	n.d.
LN3277	> 4000	> 4000	n.d.	**LN3365**	250	> 1000	n.d.
LN3278	2000	4000	2-fold	**LN3366**	250	> 1000	n.d.
LN3279	500	500	equal	**LN3367**	> 2000	> 2000	n.d.
LN3280	> 4000	> 4000	n.d.	**LN3368**	250	> 250	n.d.
LN3281	> 4000	> 4000	n.d.	**LN3369**	> 250	> 250	n.d.
LN3282	125	1000	8-fold	**LN3370**	62.25	500	8-fold
LN3283	1000	1000	equal	**LN3371**	250	> 250	n.d.
LN3284	> 4000	> 4000	n.d.	**LN3372**	62.25	500	8-fold
LN3285	4000	> 4000	n.d.	**LN3373**	500	> 1000	n.d.
LN3286	1000	1000	equal	**LN3374**	62.25	250	4-fold
LN3278	> 4000	> 4000	n.d.	**LN3375**	> 1000	> 1000	n.d.
LN3288	2000	2000	equal	**LN3447**	125	500	4-fold
LN3289	31.25	62.5-125	2- to 4-fold	**LN3448**	> 1000	> 1000	n.d.
LN3290	4000	4000	equal	**LN3789**	500	4000	8-fold
LN3291	125	250	2-fold	**LN3790**	> 4000	> 4000	n.d.
LN3292	500	1000	2-fold	**LN3791**	125	1000	8-fold
LN3293	> 4000	> 4000	n.d.	**LN3792**	1000	2000	2-fold
LN3350	62.25	500-1000	8- to 16-fold	**LN3825**	15.5	15.5	equal
LN3351	125-250	1000	4- to 8-fold	**LN3826**	500	500	equal
LN3352	125-250	2000	8- to 16-fold	**LN3828**	500	1000	2-fold
LN3353	> 2000	> 2000	n.d.	**LN4617**	4	4	equal

I treated both cell lines with the small molecules using 2-fold serial dilutions for 5 days and analyzed colony formation ability. The lowest concentration of the compounds which inhibited colony formation was defined as the effective dose (ED). ED was determined for each cell line and each small molecule and the ratio of ED NMP19$^{-/-}$ vs ED NMP53$^{-/-}$ was defined as selectivity (Table 8). In total I tested about 300 compounds. Based on the highest selectivity and lowest ED values in NMP53$^{-/-}$, LN3350 and LN3352, synthesized by Dr. Dirk Flötgen, were characterized further.

LN3350 and LN3352 showed ED values for NMP53$^{-/-}$ cells at a low nanomolar range (ED in NMP53$^{-/-}$ 62 nM for LN3350 and 125 nM - 250 nM for LN3352), which were comparable to the reference compound MLN8237, as determined in colony formation assays (Figure 6 B-D). LN3350 and LN3352 possessed a much higher selectivity towards NMP53$^{-/-}$ cells (around 8- to 16-fold), compared to MLN8237 (around 2-fold) (Figure 6 B-D). To elaborate if the inhibitory effect in NMP53$^{-/-}$ cells is caused by induction of growth arrest or cell death, I conducted cell death analysis using propidium iodide stainings 5 days post treatment, which were analyzed by flow cytometry. While in NMP19$^{-/-}$ cells almost no cell death was observed, treatment with LN3350 and LN3352 increased cell death in NMP53$^{-/-}$ 8- and 5-fold to 87.2% ± 0.9% and 86.8% ± 1.7% compared to control treated cells, respectively. MLN8237 increased cell death in NMP53$^{-/-}$ cells to 68% ± 4.6% compared to 2.5% ± 1.3% in control treated cells (Figure 6 E-G). However, in contrast to the AURKA-ligands, MLN8237 also increased cell death in NMP19$^{-/-}$ cells more than 2-fold up to 22% ± 2.2% compared to control treated cells.

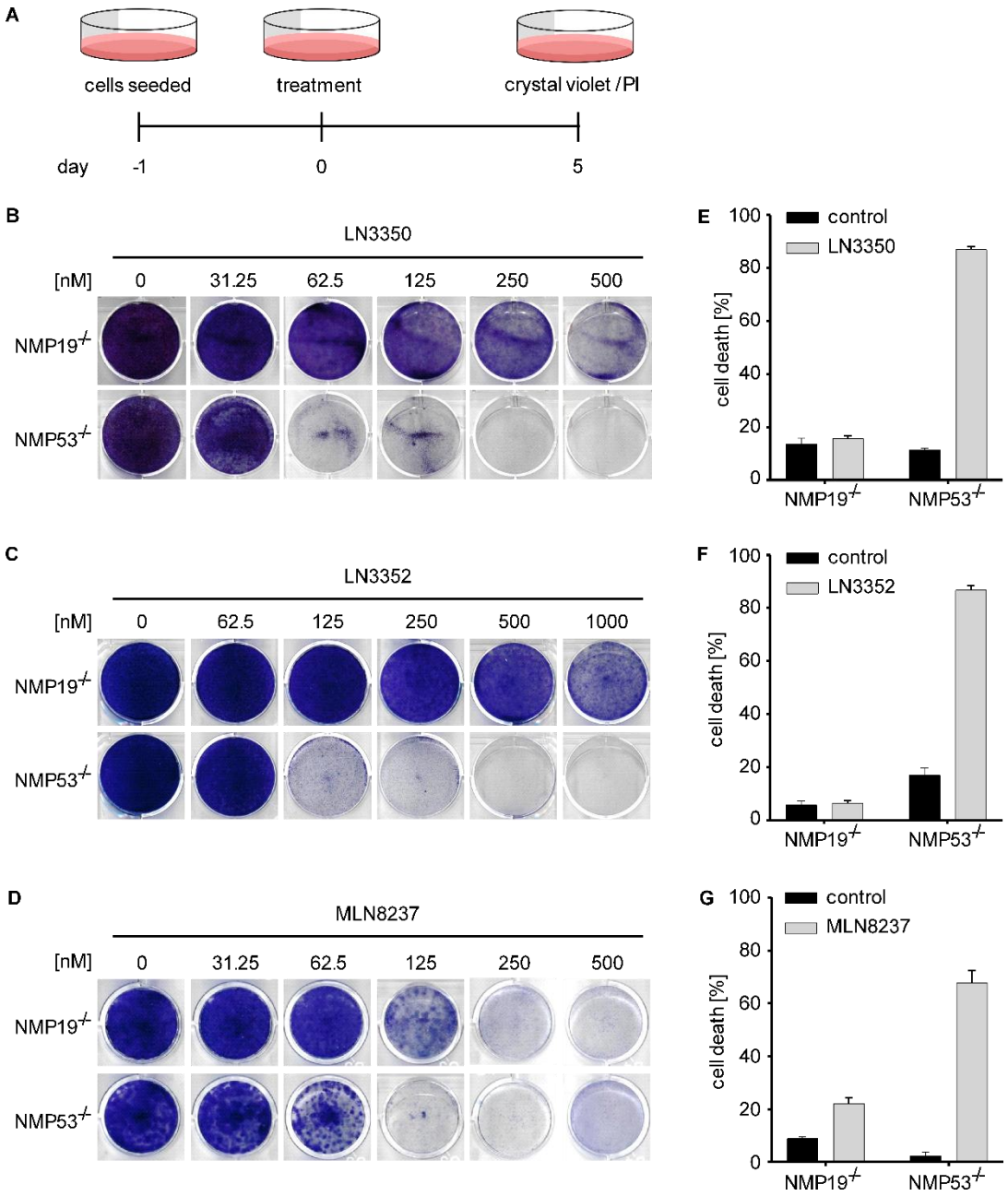

Figure 6: A) Experimental outline of the colony formation assay and the determination of cell death using propidium iodide upon treatment as depicted. **B-D)** Representative colony formation assay of NMP19$^{-/-}$ (top) and NMP53$^{-/-}$ (bottom) cells after 5 d of treatment with the indicated concentrations of LN3350 (B), LN3352 (C), MLN8237 (D), or the corresponding DMSO concentrations (n = 3 for LN3350 and LN3352, n = 2 for MLN8237). **E-G)** Quantification of propidium iodide positive NMP19$^{-/-}$ and NMP53$^{-/-}$ cells after 5 d of treatment with 60 nM LN3350 (E), 240 nM LN3352 (F), 200 nM MLN8237 (G) or the corresponding DMSO concentrations. Mean with SEM is shown (n = 1-2; 2-4 technical replicates each).

Since the aim of this study was to generate small molecules that target AURKA without inhibiting its kinase activity, I generated dose-response curves using the XTT and ADP-Glo™ assay to determine the cellular IC_{50} in NMP53$^{-/-}$ cells and the IC_{50} of the catalytic inhibition of the isolated AURKA kinase (Figure 7 A and B). LN3350 and LN3352 inhibited NMP53$^{-/-}$ cells with an IC_{50} of 13 nM ± 1 nM and 60 nM ± 8 nM, which was

lower than MLN8237 with 70 nM ± 8 nM (Figure 7 C and E). Strikingly, while MLN8237 inhibited AURKA's catalytic activity with an IC_{50} of less than 5 nM, LN3350 did not and LN3352 only merely (IC_{50} = 260 nM ± 5 nM) interfered with the kinase function of AURKA (Figure 7 D-E, data generated by Katharina Bauer). However, the IC_{50} of the catalytic inhibition of LN3352 on the isolated kinase is more than 4 times higher than the cellular IC_{50}. Therefore, since LN3350 and LN3352 exert their effect independently of kinase inhibition, I define both as AURKA-ligands.

In order to prove the actual binding of the AURKA-ligands to AURKA, we next conducted thermal shift assays (TSA) in collaboration with the group of Prof. Dr. Stefan Knapp (performed by Martin Schröder). In this assay the melting temperature of AURKA is measured with and without compound. If the compound binds AURKA, the melting temperature increases compared to the free enzyme (ΔTm). Thereby, the degree of increase in ΔTm correlates with the binding affinity of the compound to AURKA[117]. For LN3352 we could prove a good binding to AURKA by an induced ΔTm of about 10°C. Contrarily, with a ΔTm of 0.5°C we did not detect a strong binding affinity for LN3350 (Figure 7 E).

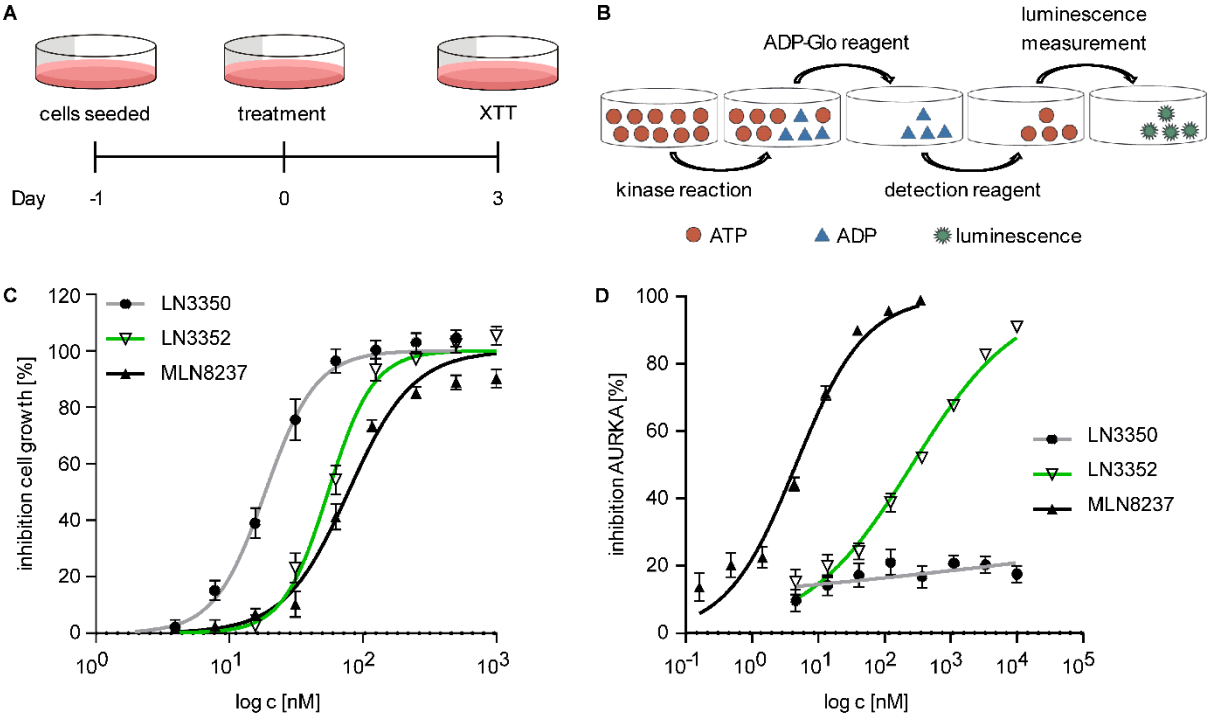

E

compound	IC_{50} NMP53$^{-/-}$ (XTT)	IC_{50} AURKA (ADP-Glo)	DeltaTm AURKA (TSA)
LN3350	13 nM +/- 1 nM	> 10^4 nM	0.5°C
LN3352	60 nM +/- 8 nM	260 nM +/- 5 nM	9.5°C
MLN8237	70 nM +/- 8 nM	4.5 nM +/- 0.01 nM	23.4°C

Figure 7: A) Experimental outline of the XTT viability assay. **B)** Schematic representation of the ADP-Glo™ kinase assay (adapted from Promega). **C)** Determination of the growth inhibition dose-response curves conducted with XTT viability assays of NMP53$^{-/-}$ cells after 3 d treatment with a 2-fold serial dilution of LN3350, LN3352 and MLN8237. Shown is the summary of 4 independent measurements with SEM. **D)** Dose-response curves of the AURKA kinase inhibition after addition of a 3-fold serial dilution of LN3350, LN3352 and MLN8237 conducted with ADP-Glo™ kinase assays. Shown is the summary of 2 independent measurements with SEM. **E)** Summary of the mean IC_{50} values of LN3350, LN3352 and MLN8237 on NMP53$^{-/-}$ cells (XTT, n = 4) and the isolated AURKA kinase (ADP-Glo™, n = 2), as well as the thermal shift on AURKAs melting temperature induced upon addition of each compound as determined by the thermal shift assay (TSA, n = 1).

Although I could prove that LN3350 and LN3352 do not inhibit the catalytic function of AURKA at concentrations of cellular IC_{50} values, I wanted to rule out the possibility that other kinases are affected as off-targets, since the ligands structure originated from classical kinase inhibitors. For this, a functional kinome screen with 320 wildtype kinases was conducted at 100 nM and 500 nM compound concentration (ProQinase) (Figure 8 A). LN3350 did not inhibit any of the kinases at the tested concentrations while LN3352 displayed an inhibition of 6 kinases to a rest activity of less than 50% only at 500 nM. Amongst those are the three members of the aurora kinase family (AURKA, AURKB and AURKC), as well as GRK2, GRK3 and ROCK1 (Figure 8 B).

Notably, the inhibition of these kinases only occurred at concentrations which were around 8 times higher than the cellular IC_{50} value (60 nM ± 8 nM).

A

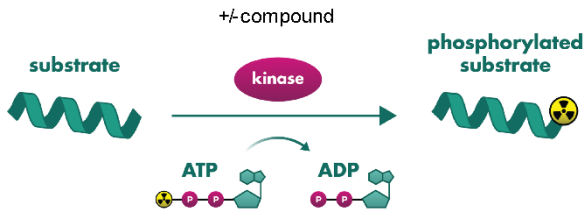

B

kinase name	residual activity [%]			
	LN3350		LN3352	
	100 nM	500 nM	100 nM	500 nM
AURKA	84	91	78	37
AURKB	106	112	81	38
AURKC	92	100	76	37
GRK2	101	111	84	38
GRK3	115	110	75	23
ROCK1	98	90	66	39
selectivity score for 320 wildtype kinases (< 50 % residual activity):	0.000	0.000	0.000	0.019

Figure 8: A) Schematic depiction of the kinase reactions measured in the kinome screen (radiometric assay, adapted from ProQinase). **B)** Summary of a kinome screen including 320 wildtype kinases performed with LN3350 and LN3352 at 100 nM and 500 nM. Shown is the catalytic rest activity of kinases that were inhibited more than 50%. Only LN3352 at a concentration of 500 nM inhibited 6 kinases more than 50%. Those kinases are AURKA, AURKB, AURKC, GRK2 (G-protein-coupled receptor kinase 2), GRK3 (G-protein-coupled receptor kinase 3) and ROCK1 (Rho-Kinase 1). Hits are shown in alphabetical order for all compound conditions. The selectivity score is calculated by dividing the number of kinases with a rest activity of 50% by the total number of kinases measured.

After proving the lack of AURKA kinase inhibition I aimed to analyze putative toxicities of LN3350 and LN3352 on non-tumorigenic cell lines. For this, I used the immortalized, non-tumorigenic murine embryonic liver cell line BNL CL.2, embryonic fibroblast cell line NIH 3T3 and NMP53$^{-/-}$ as reference cells. I first calculated the IC_{95} of each compound with XTT assays on the NMP53$^{-/-}$ cell line (LN3350: 73 nM, LN3352: 312 nM, MLN8237: 750 nM, Figure 9 A-C) and then determined the inhibitory effect of these concentrations on BNL CL.2 and NIH 3T3 cells. For all three compounds I observed a significantly stronger inhibitory effect on the tumor cell line NMP53$^{-/-}$ as compared to the non-tumorigenic lines BNL CL.2 and NIH 3T3 (Figure 9 D-F). LN3350 and LN3352 inhibited the non-tumorigenic cell lines 3-fold to 19-fold less than NMP53$^{-/-}$ cells, while MLN8237 induced a 2-fold lower inhibition. However, when comparing LN3350 and LN3352 with MLN8237, I strikingly found a 3- and 8-fold lower efficacy in BNL CL.2 cells and a 1.7- and 5-fold lower efficacy in NIH 3T3 cells (Figure 9 G and H). These results suggest, that the newly developed AURKA-targeting small molecules have an improved therapeutic index, compared to the kinase-inhibiting MLN8237.

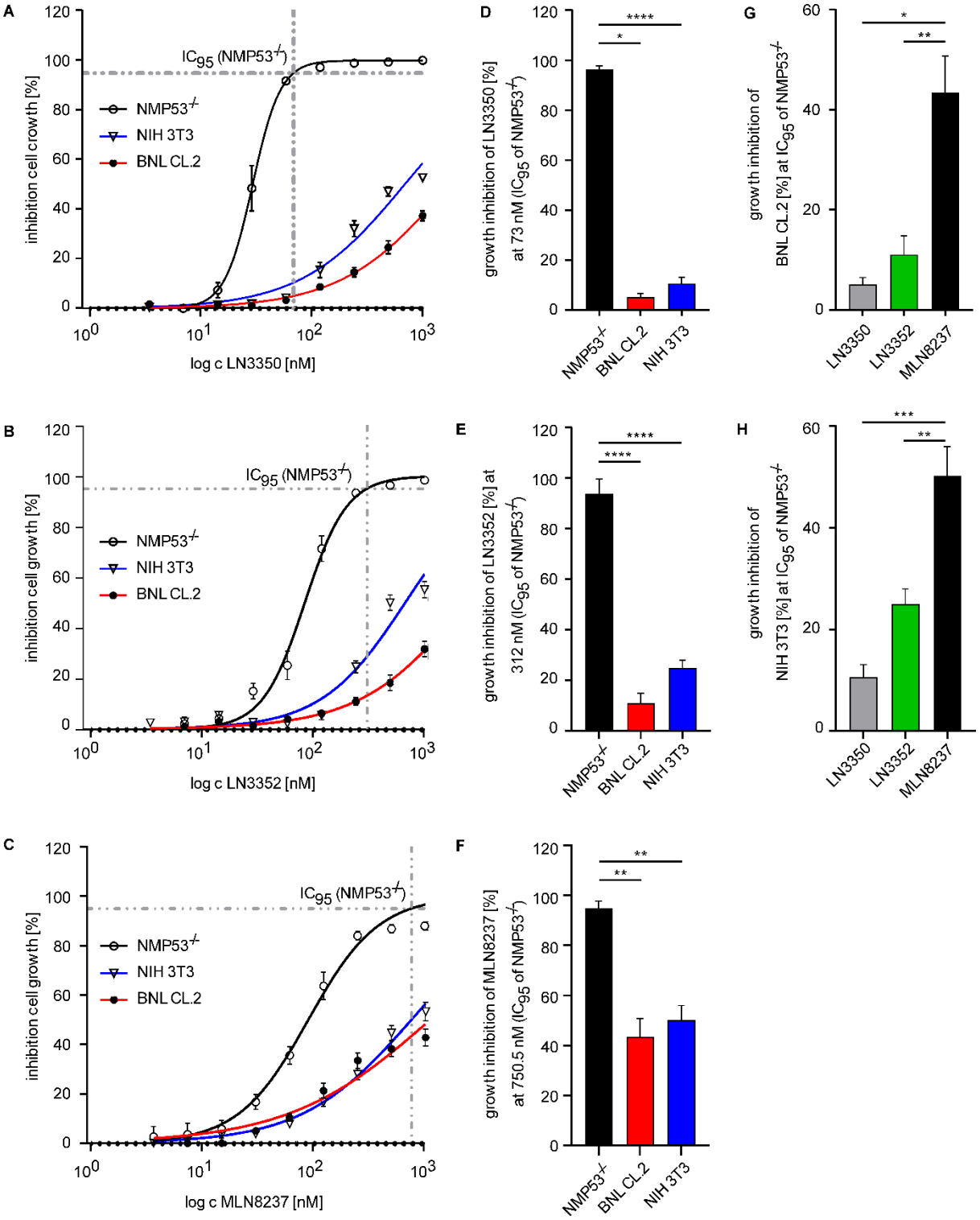

Figure 9: A-C) Determination of the growth inhibition dose-response curves conducted with XTT viability assays of NMP53$^{-/-}$, NIH 3T3 and BNL CL.2 cells after 3 d treatment with a 2-fold serial dilution of LN3350 (A), LN3352 (B) and MLN8237 (C), starting from 1 µM. Shown is the summary of 3-5 independent measurements with SEM, as well as the interpolated IC_{95} for NMP53$^{-/-}$ cells (grey dashed lines). **D-F)** Quantification of the growth inhibition of LN3350 (D), LN3352 (E) and MLN8237 (F) in NMP53$^{-/-}$, NIH 3T3 and BNL CL.2 cells at the IC_{95} concentrations of each compound in NMP53$^{-/-}$ as determined in A-C. The effect in NMP53$^{-/-}$ was compared with the one in NIH 3T3 and BNL CL.2. Shown is the mean with SEM. **G and H)** Comparison of the growth inhibitory effect of MLN8237 with LN3350 and LN3352 in BNL CL.2 (G) and NIH 3T3 (H) cells at the IC_{95} of each Compound in NMP53$^{-/-}$ cells. Shown is the mean with SEM. For normal distributed data the student's t-test was used, for non-normal distributed data the Mann-Whitney Test was used, n = 3-5 each, * p<0.05, ** p<0.01, *** p<0.001, **** p<0.0001

3.2 Induced AURKA/MYC complex disruption by AURKA-ligands does not inhibit cell growth

Next, I wanted to unravel the underlying mechanism leading to cell death in the sensitive NMP53$^{-/-}$ cells. The AURKA-ligands generated in this study were initially designed to interfere with the R-spine region of AURKA. This interference is needed to abolish the interaction of AURKA and MYC, leading to MYC degradation. Therefore, I analyzed MYC and AURKA protein levels 8 h after treatment with LN3350 and LN3352 using western blot analysis (Figure 10 A). I observed a dose-dependent reduction of MYC and an increase of AURKA protein levels (Figure 10 B and C). In order to confirm that the observed MYC downregulation is due to a disruption of the AURKA/MYC complex, I performed proximity ligation assays (PLA). The PLA is an *in situ* method used to detect the interaction between two proteins, which therefore are in very close proximity to each other. The two proteins are labeled with specific antibodies from different species, followed by an incubation with oligonucleotide-labeled secondary antibodies (probes) against the respective species. In the next steps, probes of interacting proteins ligate and are amplified by PCR. At last, fluorochrome labeled oligonucleotides hybridize to the amplicon which can then be detected as fluorescent spots (PLA foci) under the microscope (Figure 10 D). To exclude that a decrease in the AURKA/MYC interaction was caused by altered AURKA or MYC protein expression, I first determined the timepoint where MYC degradation starts to occur. For both compounds, LN3350 and LN3352, 4 h post treatment was the earliest tested timepoint when MYC degradation occurred (Figure 10 E and F). For this reason, I performed the PLA 2 h post treatment, where MYC and AURKA levels were comparable to the DMSO control. Indeed, I found that LN3350 (Figure 10 G and H) and LN3352 (Figure 10 I and J) led to a significant reduction of the number of PLA foci compared to the DMSO control (from a mean of 4.5 to 2.8 foci for LN3350 and from a mean 4.2 to 1.6 foci for LN3352), suggesting the disruption of the AURKA/MYC complex.

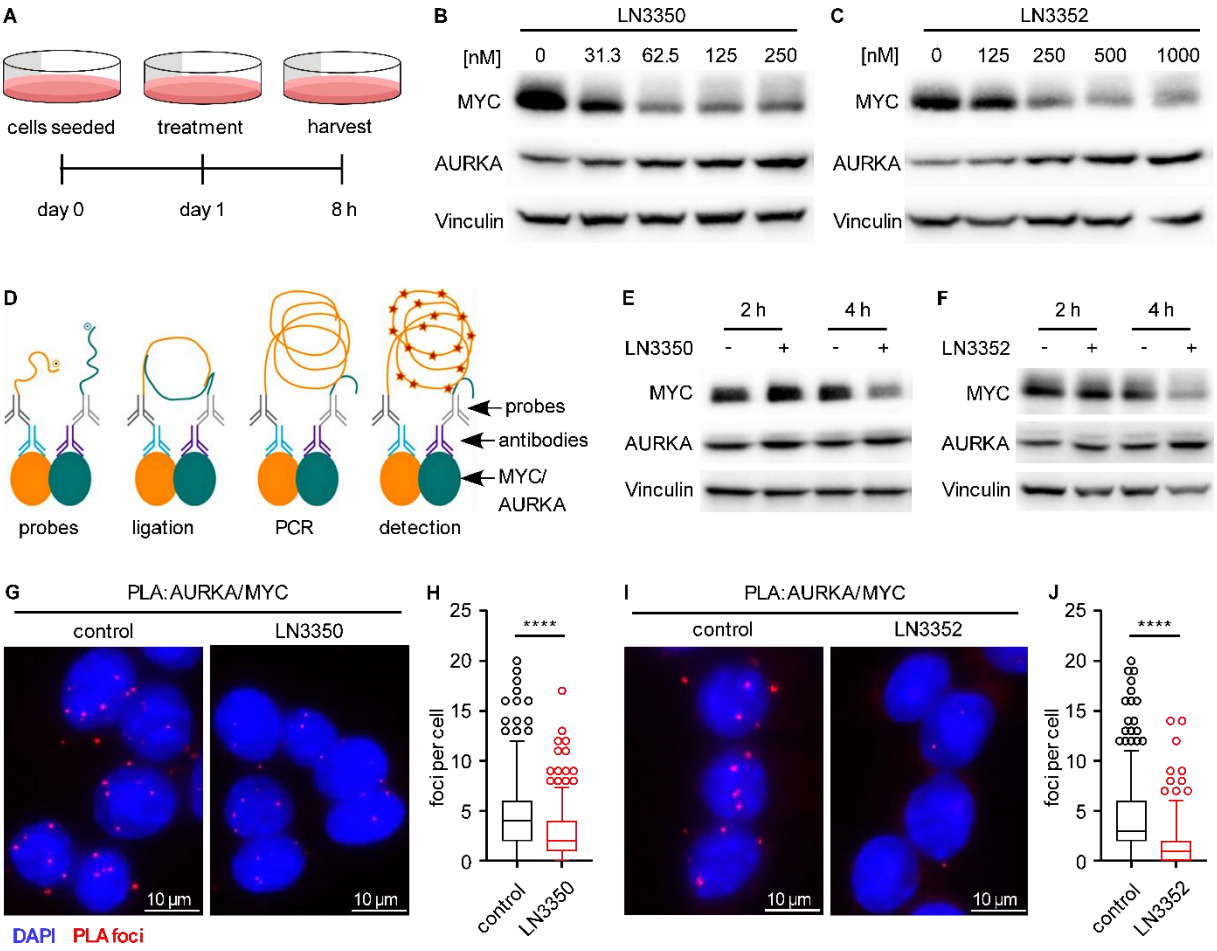

Figure 10: A) Experimental outline of western blot analyses of NMP53$^{-/-}$ upon treatment. **B and C)** Representative western blot for MYC and AURKA on lysates from NMP53$^{-/-}$ cells 8 h after treatment with the indicated concentrations of LN3350 (B) and LN3352 (C) or the highest corresponding DMSO concentration. Vinculin served as loading control. (n = 2) **D)** Schematic representation of the PLA assay (adapted from Sigma Aldrich). **E and F)** Representative western blot for MYC and AURKA on lysates from NMP53$^{-/-}$ cells at the indicated timepoints after treatment with 60 nM of LN3350 (E) and 240 nM of LN3352 (F) or the corresponding DMSO concentration. Vinculin served as loading control (n = 2). **G and H)** Representative images (G) and quantification (H) of the PLA on NMP53$^{-/-}$ cells 2 h after treatment with 60 nM LN3350 or DMSO as control. red = PLA foci, blue = DAPI. Scale bar = 10 µm. Shown is the mean of 3 independent experiments each. **I and J)** Representative images (G) and quantification (H) of the PLA on NMP53$^{-/-}$ cells 2 h after treatment with 240 nM LN3352 or DMSO as control. red = PLA foci, blue = DAPI. Scale bar = 10 µm. Shown is the mean of 3 independent experiments each. Significance was calculated using the Mann-Whitney Test, **** p<0.0001.

I next investigated, if the induced AURKA/MYC complex disruption and MYC degradation is also the reason for the observed growth inhibitory and cytotoxic effects. To test this, I took advantage of a stable MYC mutant, where the threonine on position 58 was exchanged with an alanine, MYC^{T58A}. This mutant cannot be phosphorylated on position 58, and subsequently cannot be ubiquitinated, preventing proteasomal degradation[118] (Figure 11 A). I used murine *Nras^{G12V};Trp53$^{-/-}$* HCC cell lines, either overexpressing the human wildtype *MYC* (in the following called NP53$^{-/-}$ MYC^{WT}) or T58A mutant *MYC* (in the following called NP53$^{-/-}$ MYC^{T58A}), previously generated by Dr. Ramona Rudalska from tumor tissue. Three different cell lines of each genotype

were analyzed regarding MYC phosphorylation at position 58. As expected, only the cell lines expressing wildtype MYC protein showed a phosphorylation at position 58, whereas the cells expressing MYC^{T58A} protein were not phosphorylated. Notably, there was no difference in AURKA levels between these cell lines (Figure 11 B). Next, I treated $NP53^{-/-}$ MYC^{WT} and $NP53^{-/-}$ MYC^{T58A} cells with increasing concentrations of LN3352 and analyzed the MYC protein levels. I could confirm, that in contrast to cells expressing wildtype MYC protein, which showed a dose-dependent reduction of MYC and induction of AURKA (Figure 11 C), both protein levels remained unchanged in MYC^{T58A} cells (Figure 11 D). However, colony formation assays and cell viability assays using XTT revealed, that there was no difference in the response between $NP53^{-/-}$ MYC^{WT} and $NP53^{-/-}$ MYC^{T58A} cells upon treatment with LN3350 and LN3352 (Figure 11 E-G).

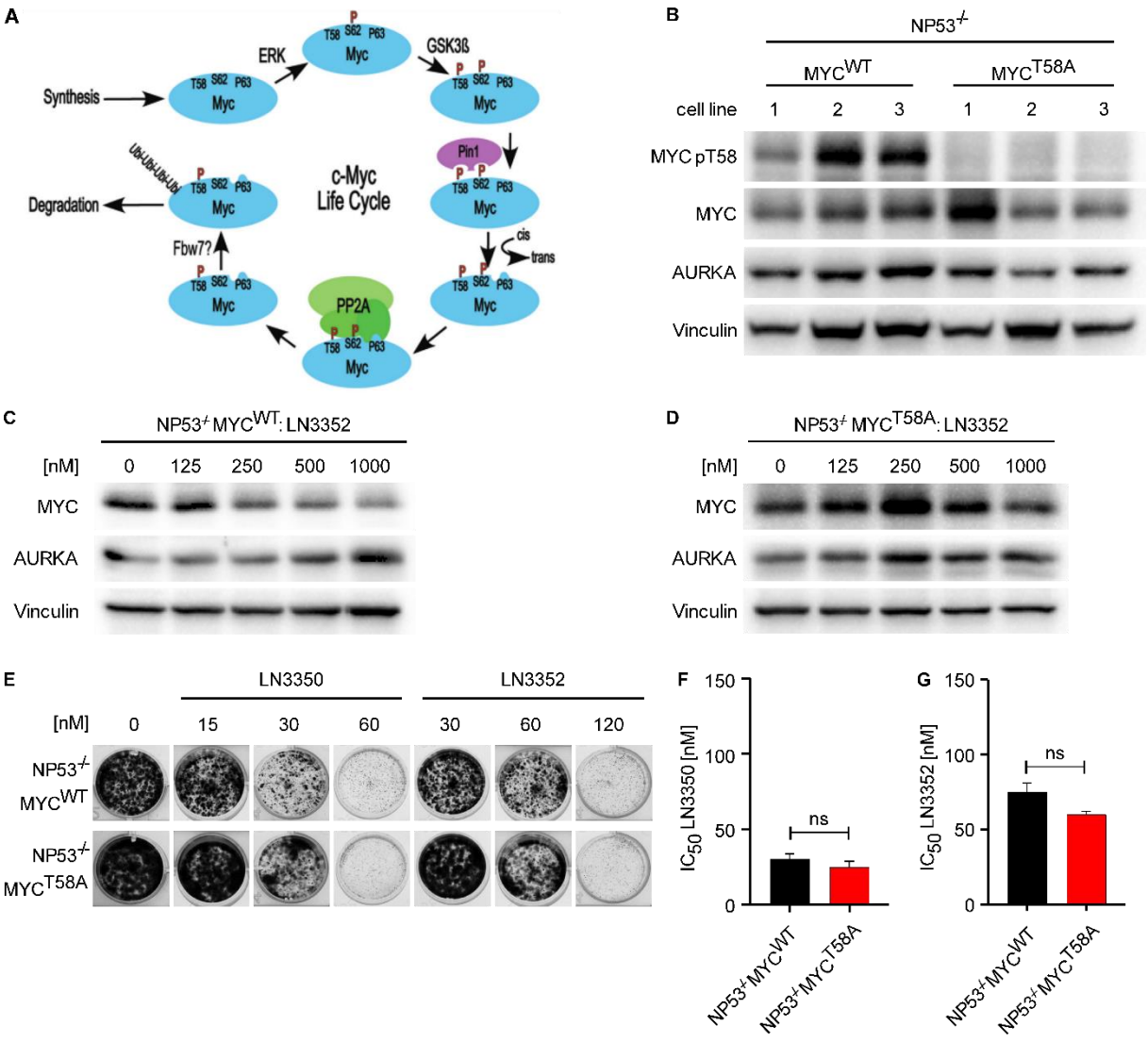

Figure 11: A) Schematic representation of the lifecycle of MYC (adapted from [119]). **B)** Western blot for pMYC (T58), MYC and AURKA with lysates from 3 cell lines of NP53$^{-/-}$ MYC^{WT} and NP53$^{-/-}$ MYC^{T58A} cells. Vinculin served as loading control. **C and D)** Representative western blot for MYC and AURKA with lysates from NP53$^{-/-}$ MYC^{WT} and NP53$^{-/-}$ MYC^{T58A} cells 8 h after treatment with the indicated concentrations of LN3352 or the highest corresponding DMSO concentration. Vinculin served as loading control. (n = 2 different cell lines each). **E)** Representative colony formation assay of NP53$^{-/-}$ MYC^{WT} (top) or NP53$^{-/-}$ MYC^{T58A} (bottom) cells after 5 d of treatment with the indicated concentrations of LN3350 and LN3352, or the highest corresponding DMSO concentrations. (n = 3 different cell lines each). **F and G)** Quantification of the IC_{50} values of LN3350 (F) and LN3352 (G) on NP53$^{-/-}$ MYC^{WT} and NP53$^{-/-}$ MYC^{T58A} using the XTT viability assay. Shown is the mean of 3 different cell lines each and 2 independent experiments per cell line with SEM. For normal distributed data student's t-test was used, for non-normal distributed data Mann-Whitney Test was used. n = 6 each. ns, not significant.

MYC is a transcription factor that needs access to the nucleus in order to function. Since the novel compounds exerted their therapeutic effects also without MYC degradation, I set out to analyze potential other modes of action. First, I wanted to test if the AURKA-ligands exert their function by altering the MYC localization within the cell. So, I treated NMP53$^{-/-}$ cells for one day with either DMSO as control or LN3350 and LN3352 and performed immunofluorescence staining for MYC (Figure 12 A). Even 24 h after addition of LN3350 and LN3352 MYC showed a normal localization mainly in the nuclei of the cells, as it is observed in DMSO-treated control cells (Figure 12 B). Therefore, an alteration of MYC localization could be excluded as a mechanism of action.

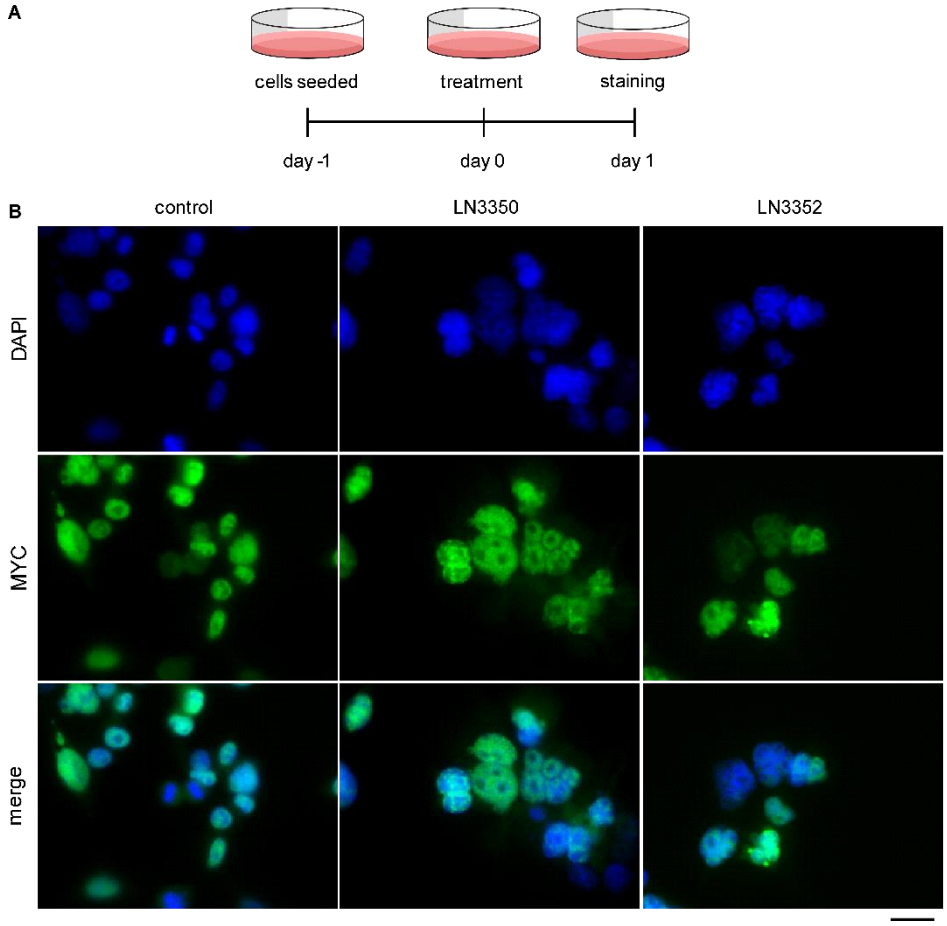

Figure 12: A) Experimental outline of MYC stainings. **B)** Representative photographs of NMP53$^{-/-}$ cells stained for MYC 24 h after treatment with 60 nM LN3350 or 240 nM LN3352. green = MYC, blue = DAPI. n = 2, scale bar = 20 µm.

3.3 AURKA-ligands increased AURKA/TPX2 interaction, TPX2 stabilization and AURKA kinase activity

After showing a decreased AURKA/MYC complex formation, I elaborated which other interaction partners of AURKA are affected by the small molecules. I performed a FLAG-AURKA co-immunoprecipitation (Co-IP) followed by mass spectrometry analysis. For the generation of a stable NMP53$^{-/-}$ cell line expressing doxycycline (DOX)- inducible FLAG-AURKA I first cloned the FLAG-tagged *Aurka* cDNA into the RT3GP2APIR plasmid, which was previously generated in the laboratory (Figure 13 A, for cloning strategy see methods 2.1.8.1). Phoenix Eco cells were transfected via the $CaPO_3$ method to produce viral particles containing the plasmid. Viral supernatant was harvested after 36 h and NMP53$^{-/-}$ were infected. To ensure stable integration of the FLAG-AURKA construct in all cells, they were selected with puromycin for 48 h (Figure 13 A). The expression of FLAG-AURKA was validated via western blot 24 h after

addition of DOX using FLAG and AURKA antibodies. The FLAG-tagged AURKA showed a slight increase in the molecular weight compared to the endogenous AURKA in DOX-treated cells (Figure 13 B). Since AURKA mainly functions and interacts with its partners in mitosis (M phase), I synchronized the cells in M phase using 50 ng/mL nocodazole for 6 h. After labeling cells with PI, I performed flow cytometry analysis which showed a decrease in G1 and S phase peaks and an increase in G2/M peak in nocodazole treated cells compared to controls (Figure 13 C). For the Co-IP with subsequent mass spectrometry analysis, NMP53$^{-/-}$ expressing the DOX-inducible FLAG-AURKA were separately cultured for at least 2 weeks with three different SILAC media (light, medium, heavy). This leads to the incorporation of distinct isotopically labeled amino acids, allowing afterwards to pool cells with different treatment conditions for the mass spectrometry and separate them in the following analysis according to the incorporated isotopes.

After induction of FLAG-AURKA with DOX in SILAC-labeled NMP53$^{-/-}$ cells (light: no DOX, IP control; medium and heavy: plus DOX) and synchronization with 50 ng/mL nocodazole for 6 h, the cells were released from nocodazole and treated with either LN3352 or DMSO as control (Figure 13 D). 2 h after treatment the Co-IP was performed and the lysates analyzed via mass spectrometry by the Proteome Centre Tübingen. By calculating the intensity ratio between LN3352 and DMSO treated samples, which was done by Dr. Thales Kronenberger, we could elaborate the proteins that showed an increased (Figure 13 E) or decreased (Figure 13 F) interaction with AURKA upon treatment. Using the BioGRID database, a repository for known protein-protein interactions, I found that TPX2 is the only identified protein, whose interaction to AURKA was described before.

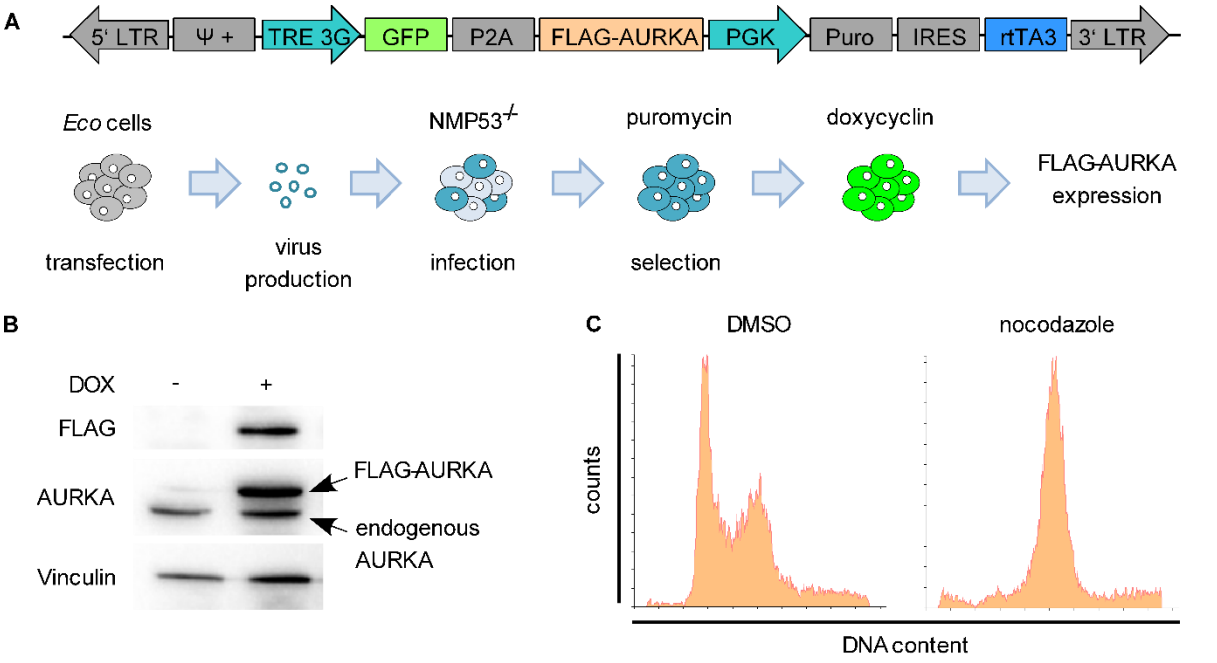

E

increased AURKA-interaction	ratio LN3352/DMSO
ANXA2;ANXA2P2	3.03
TPX2	2.27
SRSF7	2.10
ALYREF	1.41
JAK1	1.36

F

decreased AURKA-interaction	ratio LN3352/DMSO
ENO1	-1.56
PGK1	-1.35
CCT8	-1.34
GNB1	-1.28
DYNLL2;DYNLL1	-1.20
CCT4	-1.04
LMNA	-0.98

Figure 13: A) Schematic representation of the generation of stable cell lines with genomically integrated DOX-inducible FLAG-AURKA. NMP53$^{-/-}$ cells were infected with retroviral particles produced in Eco Phoenix cells and selected with puromycin. FLAG-AURKA expression was induced with DOX for 24 h. **B)** Western blot for FLAG and AURKA on lysates of NMP53$^{-/-}$ cells stably expressing DOX-inducible FLAG-AURKA 24 h after DOX addition. Vinculin served as loading control. **C)** Representative cell cycle analysis, as determined by DNA staining with propidium iodide, of NMP53$^{-/-}$ cells 6 h after treatment with 50 ng/mL nocodazole, or DMSO as control. (n = 2). **D)** Experimental setup of the Co-IP experiment analyzed with mass spectrometry. (n = 2). **E and F)** Results of the mass spectrometry analysis as depicted in D). Shown are the proteins with increased (E) or decreased (F) AURKA interaction upon treatment with 240 nM LN3352 for 2 h compared to DMSO treated cells.

To validate AURKA/TPX2 interactions, I repeated the experiment depicted in Figure 13 D with normal medium and analyzed the input and Co-IP lysates with western blots using antibodies against TPX2 and AURKA (Figure 14 A). To allow for comparison between both the AURKA-ligands and the reference compound MLN8237, I also treated cells with LN3350 and MLN8237. I found that LN3350 and LN3352 showed an increase in TPX2 levels in Co-IP lysates compared to DMSO control while MLN8237 had levels comparable to DMSO control. Interestingly, TPX2 levels in the input also had increased levels for LN3350 and LN3352 compared to DMSO while MLN8237 treated samples again showed comparable levels (Figure 14 B).

Since I showed that in contrast to NMP53$^{-/-}$ cells, NMP19$^{-/-}$ cells do not respond to AURKA-ligands, I aimed to compare the effect on the AURKA/TPX2 interaction in both cell lines. For this I generated a NMP19$^{-/-}$ cell line stably expressing the DOX-inducible FLAG-AURKA construct shown in Figure 13 A and validated the FLAG-AURKA expression with western blot analysis 24 h after induction (Figure 14 C).

I treated the NMP19$^{-/-}$ cells as depicted in Figure 13 D with normal media and performed Co-IP and western blot experiments. The Co-IP revealed that also in the non-sensitive NMP19$^{-/-}$ cells the AURKA-ligands induced an increased binding of TPX2 to AURKA, which is not the case for MLN8237, similar to NMP53$^{-/-}$ cells. Again, TPX2 levels in the input were increased in LN3350 and LN3352 treated cells, while MLN8237 did not show an increase compared to DMSO control (Figure 14 D).

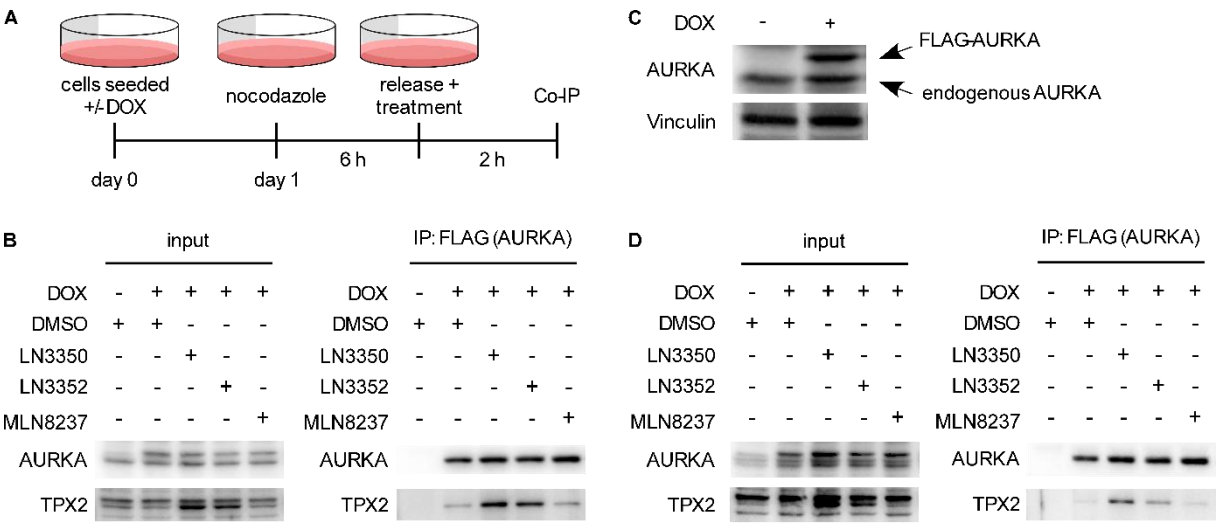

Figure 14: A) Experimental outline of the Co-IP analysis of NMP53$^{-/-}$ and NMP19$^{-/-}$ cells stably expressing DOX-inducible FLAG-AURKA upon treatment using a FLAG antibody. **B)** Western blot for AURKA and TPX2 on Co-IP and input lysates from NMP53$^{-/-}$ cells stably expressing DOX-inducible FLAG-AURKA after synchronization with nocodazole followed by release and treatment with 60 nM LN3350, 240 nM LN3352 and 200 nM MLN8237 or the highest corresponding DMSO concentration. (n = 2). **C)** Western blot for AURKA on lysates of NMP19$^{-/-}$ cells stably expressing DOX-inducible FLAG-AURKA 24 h after DOX addition. Vinculin served as loading control. **D)** Western blot for AURKA and TPX2 on Co-IP and input lysates from NMP19$^{-/-}$ cells stably expressing DOX-inducible FLAG-

AURKA after synchronization with nocodazole followed by release and treatment with 60 nM LN3350, 240 nM LN335 and 200 nM MLN8237 or the highest corresponding DMSO concentration. (n = 4)

To further validate those findings, I repeated the Co-IP with a RT3GP2APIR FLAG-TPX2 construct (Figure 15 A, for cloning strategy see 2.1.8.2). For this I generated NMP53$^{-/-}$ and NMP19$^{-/-}$ cell lines stably expressing DOX-inducible FLAG-TPX2 according to the strategy shown in Figure 13 A. Western blot analysis 24 h after DOX induction showed increased levels of FLAG-TPX2 bands, with slightly increased molecular weight compared to endogenous TPX2 (Figure 15 B and C). Co-IP analysis of nocodazole synchronized and released cells confirmed the enhanced TPX2/AURKA binding upon treatment with LN3350 and LN3352 in both cell lines, as shown by the increased AURKA protein levels (Figure 15 D and E). Interestingly, also the exogenously expressed FLAG-TPX2 showed higher TPX2 levels after treatment. MLN8237, in line with the previous result, showed no altered binding of AURKA to TPX2 in Co-IP lysates from both cell lines and no increase in TPX2 levels (Figure 15 D and E).

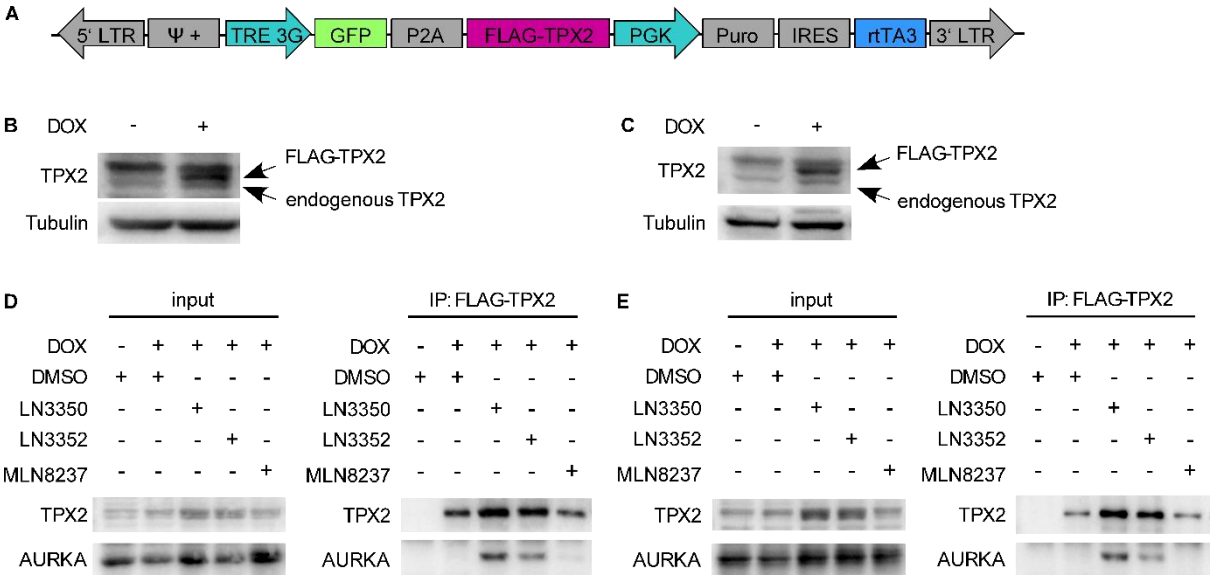

Figure 15: A) Schematic representation of the vector used to generate cell lines stably expressing DOX-inducible FLAG-TPX2. **B and C)** Western blot for TPX2 on lysates of NMP53$^{-/-}$ cells (B) and NMP19$^{-/-}$ (C) stably expressing DOX-inducible FLAG-TPX2 24 h after DOX addition. Tubulin served as loading control. **D and E)** Western blot for TPX2 and AURKA on Co-IP and input lysates from NMP53$^{-/-}$ (D) and NMP19$^{-/-}$ (E) cells stably expressing DOX-inducible FLAG-TPX2 after synchronization with nocodazole followed by release and treatment with 60 nM LN3350, 240 nM LN3352 and 200 nM MLN8237 or the highest corresponding DMSO concentration. (n = 1 for D, n = 2 for E).

Since TPX2 is known to localize AURKA to the mitotic spindles upon complex formation[74, 84], I next wanted to determine if the AURKA-ligands induce any

abnormalities in the localization of the AURKA/TPX2 complex. Therefore, I performed AURKA and TPX2 co-stainings in NMP53$^{-/-}$ and NMP19$^{-/-}$ cells 2 h post treatment, which showed that the co-localization of AURKA and TPX2 to the spindles of mitotic cells is comparable to controls (Figure 16 A and B). However, upon treatment with MLN8237, I observed in both cell lines that only TPX2 localized to the spindles, but not AURKA. This was in line with the results from the Co-IP experiments (Figure 14 B and D and Figure 15 D and E), where I did not observe an increased AURKA/TPX2 binding. Additionally, I found that the treatment with AURKA-ligands induced the formation of non-bipolar, abnormal spindles in both cell lines.

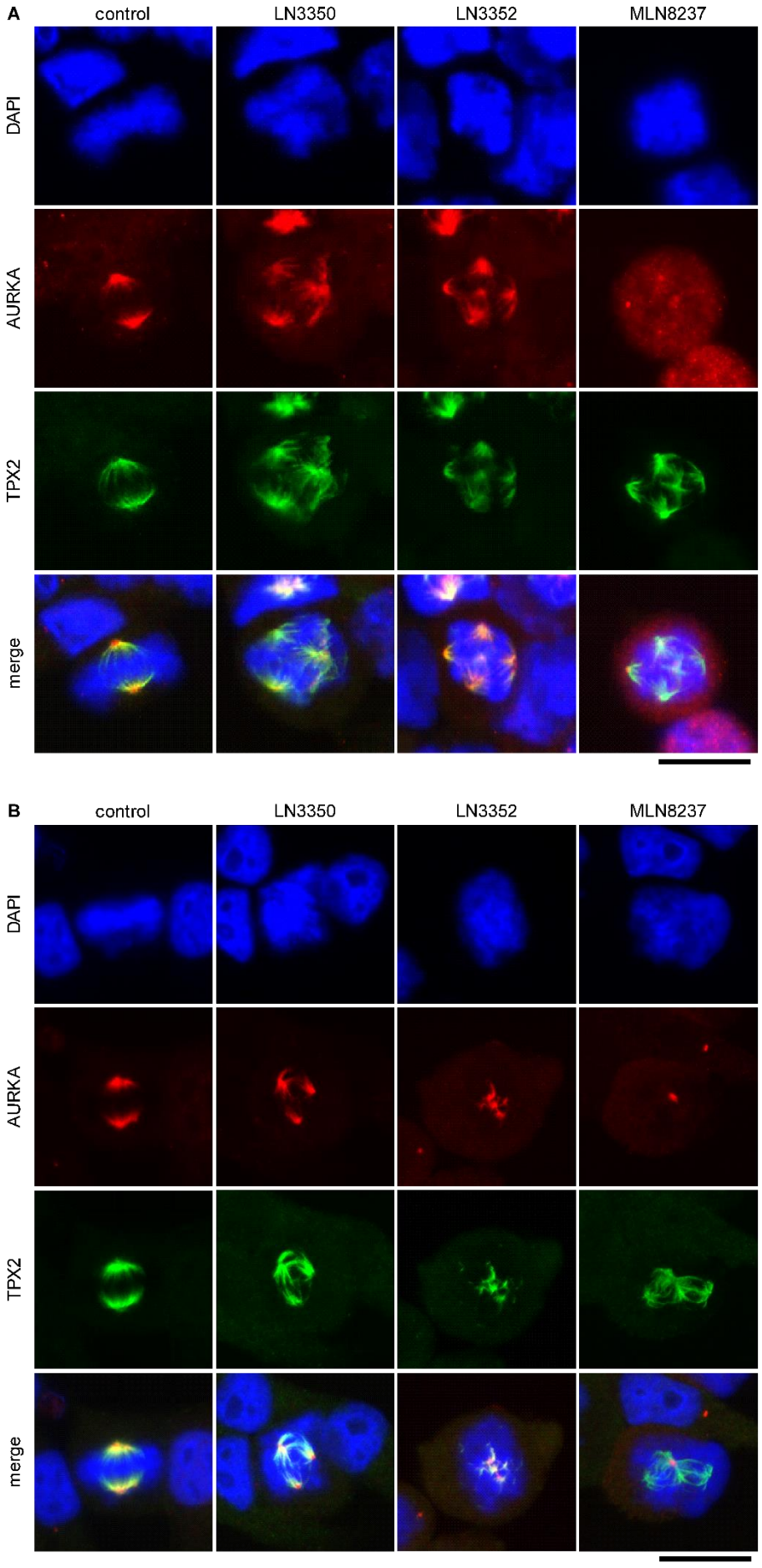
A
control
LN3350
LN3352
MLN8237
DAPI
AURKA
TPX2
merge
B
control
LN3350
LN3352
MLN8237
DAPI
AURKA
TPX2
merge

Figure 16: Representative photographs of AURKA and TPX2 double staining on NMP53$^{-/-}$ cells **(A)** and NMP19$^{-/-}$ cells **(B)** 2 h after treatment with 60 nM LN3350, 240 nM LN3352 and 200 nM MLN8237. DMSO served as control. red = AURKA, green = TPX2, blue = DAPI. Scale bar = 20 µm.

It is described, that the binding of TPX2 to AURKA renders AURKA in an active conformation and prevents dephosphorylation at Threonine 288 (Thr288; Thr279 in murine AURKA as determined using the Phosphosite Plus database; in the following referred to as Thr288) by the protein phosphatase 1 (PP1), leading to an increased phosphorylation and activation of AURKA[85]. Since the AURKA-ligands stabilized the AURKA/TPX2 complex, I analyzed the phosphorylation status at Thr288 of AURKA upon treatment (Figure 17 A). Western blot analysis revealed that the pThr288 increased in a concentration-dependent manner upon treatment with LN3350 (Figure 17 B) and LN3352 (Figure 17 C) in NMP53$^{-/-}$ cells. Accordingly, the phosphorylation of PLK1 on Threonine 210, a downstream target of AURKA, also increased concentration-dependently. In contrast, MLN8237, which is a strong AURKA kinase inhibitor, led to concentration-dependent decrease in pThr288 AURKA and unaltered pThr210 PLK1 levels (Figure 17 D).

I next determined the AURKA activation in NMP19$^{-/-}$ cells upon treatment. Comparable to NMP53$^{-/-}$ cells, the treatment of LN3350 and LN3352 led to an increased AURKA phosphorylation at Thr288 and phosphorylation of the downstream target PLK1 at Thr210 (Figure 17 E and F). In contrast, MLN8237 again led to an AURKA dephosphorylation on Thr288 and did not change phosphorylation of PLK1 Thr210 (Figure 17 G).

The observed identical effects of the AURKA-ligands on the AURKA/TPX2 complex, TPX2 stabilization and AURKA activation raise the question why only TP53-altered cells but not p19^{ARF}-altered cells die upon exposure to AURKA-ligands.

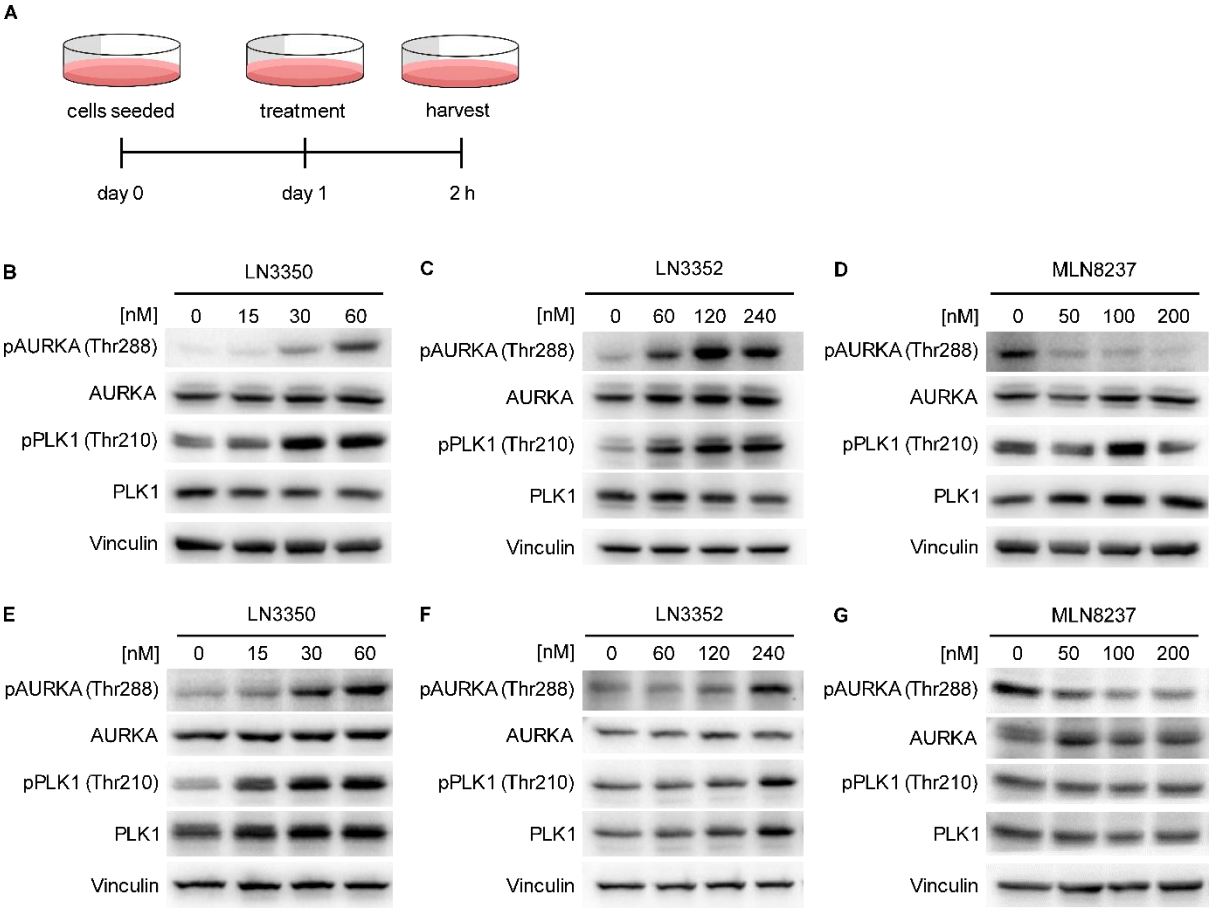

Figure 17: A) Experimental outline of western blot analyses of NMP53$^{-/-}$ and NMP19$^{-/-}$ upon treatment. **B-D)** Western blot for pAURKA (Thr288), AURKA, pPLK1 (Thr210) and PLK1 on lysates from NMP53$^{-/-}$ cells 2 h after treatment with the indicated concentrations of LN3350 (B), LN3352 (C), MLN8237 (D) or the highest corresponding DMSO concentration. Vinculin served as loading control. (n = 2 for LN3350 and LN3352, n = 1 for MLN8237). **E-G)** Western blot for pAURKA (Thr288), AURKA, pPLK1 (Thr210) and PLK1 on lysates from NMP19$^{-/-}$ cells 2 h after treatment with the indicated concentrations of LN3350 (E), LN3352 (F), MLN8237 (G) or the highest corresponding DMSO concentration. Vinculin served as loading control. (n = 1)

3.4 *Trp53*-deficiency prevents rescue of cell cycle arrest and abnormal spindle formation upon AURKA-ligand treatment

Mitotic processes are tightly regulated in a cell in order to ensure a normal mitosis and the formation of two daughter cells with the correct genome. Thus, the activation changes in mitosis-regulating proteins like AURKA and PLK1 are likely to provoke mitotic defects, leading to the activation of the mitotic cell cycle checkpoint. To test this hypothesis, I conducted cell cycle analyses of PI-labeled NMP53$^{-/-}$ cells upon treatment for up to 48 h using flow cytometry (Figure 18 A). Indeed, I could show that LN3350 (Figure 18 B) and LN3352 (Figure 18 C) induced a pronounced G2/M arrest at 6 h post treatment. However, between 16 h and 48 h cells accumulated DNA contents, leading to polyploid cells. Additionally, I observed an increasing subG1 fraction in NMP53$^{-/-}$

cells, representing dead cells, which is in line with the results from Figure 6, showing that AURKA-ligands lead to cell death in NMP53$^{-/-}$ cells. Moreover, also MLN8237 led to a G2/M arrest 6 h after treatment, followed by the acquisition of a polyploid status and cell death between 16 h and 48 h after treatment (Figure 18 D).

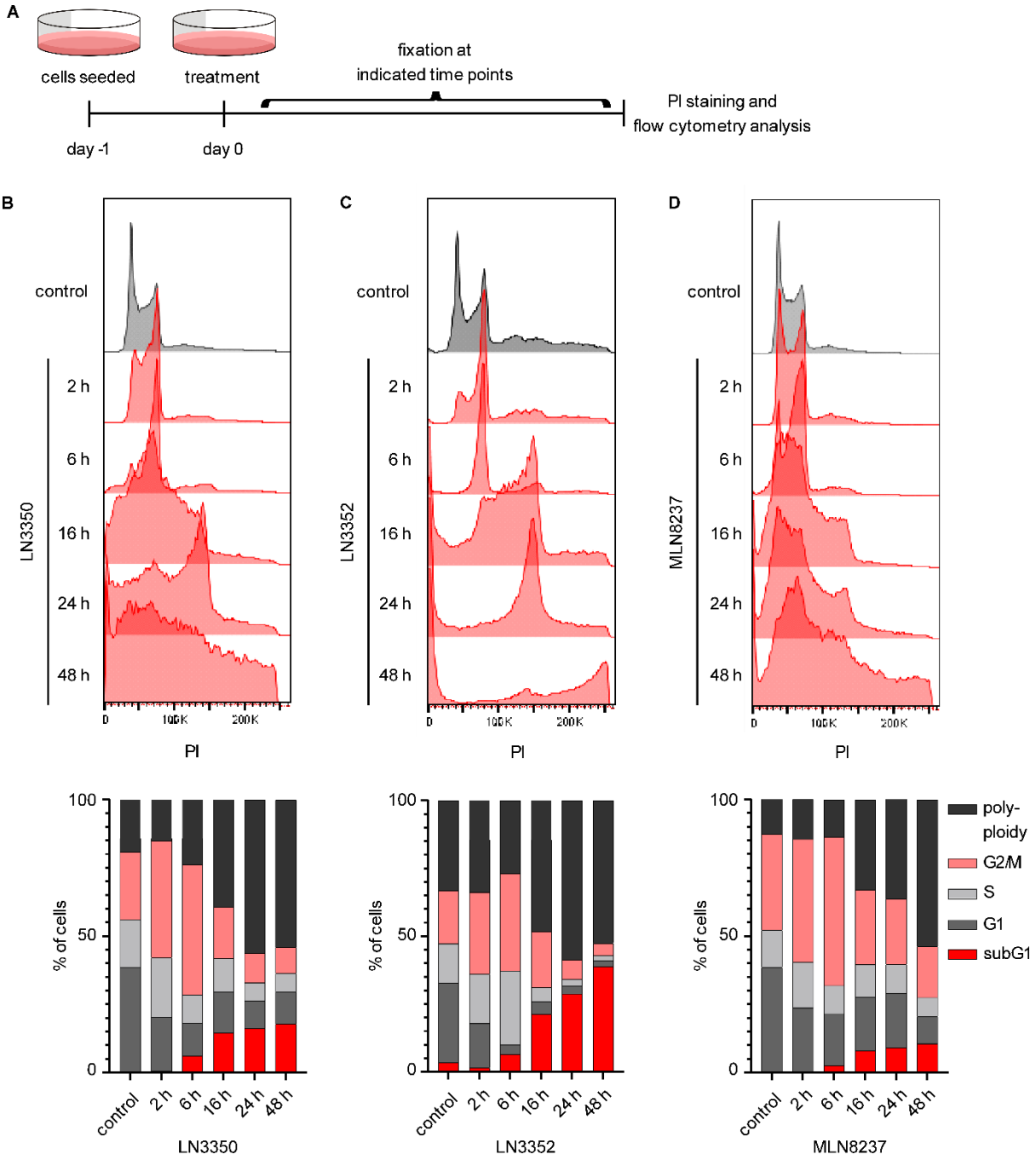

Figure 18: A) Experimental outline of cell cycle analyses, as conducted by flow cytometry measurement of propidium iodide stained cells. **B-D)** Representative cell cycle analysis and quantification of the cell cycle distribution of NMP53$^{-/-}$ cells at the indicated time points after treatment with 60 nM LN3350 (B), 240 nM LN3352 (C), 200 nM MLN8237 (D) or DMSO as control. (n = 2 for LN3350 and MLN8237, n = 1 for LN3352).

To elaborate the differences that render NMP19$^{-/-}$ cells resistant to the AURKA-ligands, I next conducted cell cycle analysis of the NMP19$^{-/-}$ cells. Again, 6 h after treatment LN3350 (Figure 19 A) and LN3352 (Figure 19 B) induced a transient G2/M arrest, although, contrary to NMP53$^{-/-}$ cells (Figure 18 B and C) a portion of cells still were in G1 or S phase. Strikingly, in contrast to the sensitive NMP53$^{-/-}$ cells, I did not observe polyploid cells between 10 h and 48 h after treatment and only a slight increase in the subG1 fraction. Instead, the G2/M peak decreased and G1 fraction increased again. This was in line with the previously described colony formation and cell death analysis (Figure 6 C and F), which showed that the AURKA-ligands did not induce cell death in NMP19$^{-/-}$ cells which continued to grow. In MLN8237-treated cells I also saw an increase in the G2/M peak after 6 h (Figure 19 C), however it was less compared to LN3350 or LN3352 treatment. Between 10 h and 48 h ratios between G1, S and G2/M phase did not change, however, there was a slight increase in polyploid cells.

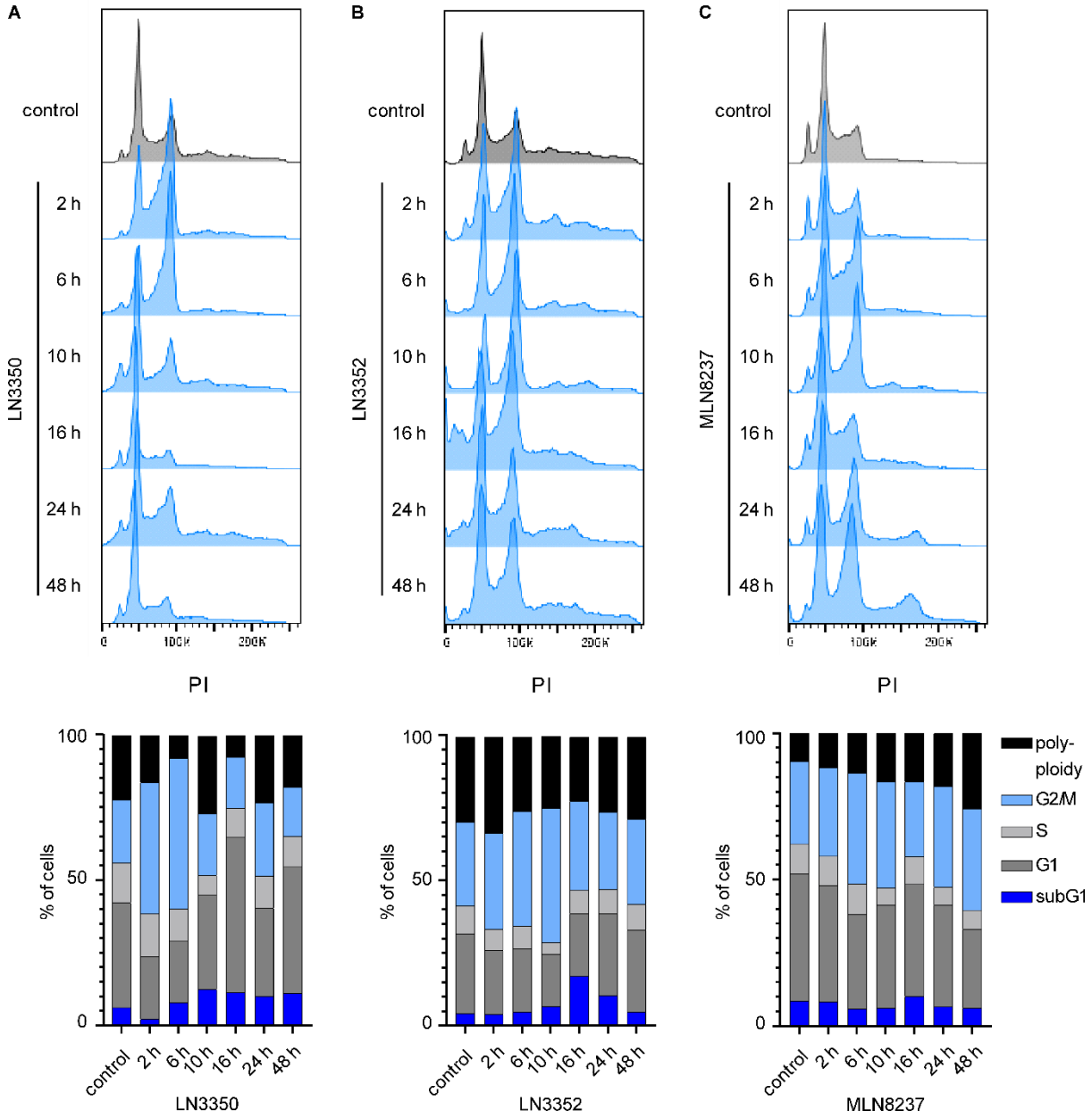

Figure 19: A-C) Representative cell cycle analysis and quantification of the cell cycle distribution, as determined by DNA staining with propidium iodide, of NMP19$^{-/-}$ cells at the indicated time points after treatment with 60 nM LN3350 (B), 240 nM LN3352 (C), 200 nM MLN8237 (D) or DMSO as control. (n = 2 for LN3350 and MLN8237, n = 1 for LN3352).

The fact that compared to NMP53$^{-/-}$ cells, NMP19$^{-/-}$ cells divide and cycle normally after an initial mitotic arrest is surprising since I found the formation of abnormal spindles upon treatment in both cell lines (Figure 16). A possible explanation could be that NMP19$^{-/-}$ are able to resolve the abnormal spindles over time, allowing for proper cell division, while NMP53$^{-/-}$ cells cannot. In order to test this, I performed α-tubulin staining to visualize the spindles of treated NMP53$^{-/-}$ and NMP19$^{-/-}$ cells at 1 h, 24 h and 48 h post treatment. Then, I calculated the percentage of mitotic cells (defined as cells being

in prometaphase or metaphase as determined by α-tubulin immunofluorescence staining) with abnormal spindles (defined as multipolar, monopolar, weak or no spindle formation) (Figure 20 A and B).

Already 1 h post treatment of NMP53$^{-/-}$ cells, LN3350 and LN3352 lead to a concentration-dependent formation of abnormal spindles. When using the highest selected concentration 100% of the mitotic cells showed abnormal spindle formation compared to 26% in DMSO controls (Figure 20 C and D). Those spindle defects were robust and maintained until the latest analyzed time point of 48 h. MLN8237 also induced the formation of abnormal spindles in 68% of mitotic NMP53$^{-/-}$ cells 1 h post treatment. The number of mitotic cells with abnormal spindles further increased until 48 h, reaching 94% with the highest MLN8237 concentration (Figure 20 E). I also observed a concentration-dependent formation of abnormal spindles in up to 100% of mitotic NMP19$^{-/-}$ cells 1 hour after treatment with LN3350 and LN3352 compared to around 14% in control cells (Figure 20 F and G). However, I found a time-dependent recovery of the spindles, shown by the reduction of abnormal spindles down to baseline levels (23%) in LN3350 and 38% in LN3352 treated cells, respectively, after 48 h. Similar to NMP53$^{-/-}$ cells, MLN8237 led to the induction of abnormal spindles in 85% of mitotic spindles after 1 h, which further increased concentration-dependent to 100% at 48 h post treatment (Figure 20 H).

Taken together, my data suggest, that despite the fact that the newly developed AURKA-ligands share similarities with the reference compound MLN8237, like the disruption of the AURKA/MYC complex, there are main differences in the way they influence mitosis, highlighting a novel mode of action of the AURKA-ligands.

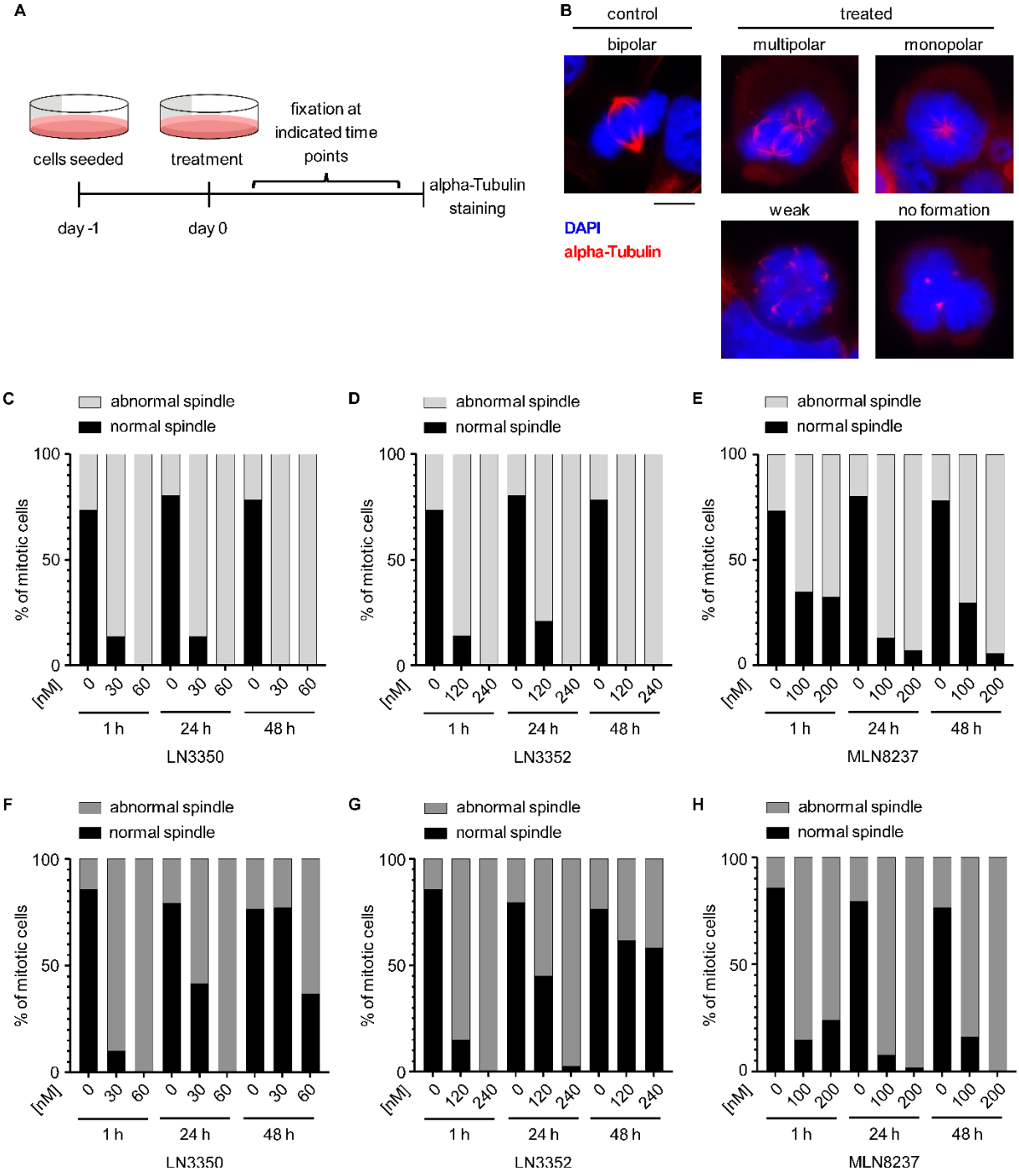

Figure 20: A) Experimental outline of α-Tubulin staining experiments. **B)** Representative images of an α-Tubulin staining on NMP53$^{-/-}$ cells 24 h after treatment with 60 nM LN3350 or DMSO as control. red = α-Tubulin, blue = DAPI. Scale bar, 10 µm. **C-H)** Representative quantification of normal or abnormal spindles (multipolar, monopolar, weak, no formation) in mitotic NMP53$^{-/-}$ (C-E) or NMP19$^{-/-}$ (F-H) cells after 1 h, 24 h and 48 h post treatment with the indicated concentration of LN3350 (C and F), LN3352 (D and G), MLN8237 (E and H) or the highest corresponding DMSO concentration. (n = 2). 15 to 60 cells per condition were counted.

3.5 AURKA-ligands lead to cell death due to mitotic catastrophe in *Trp53*-deficient cells

Showing the ability of *Trp53* wildtype tumor cells to recover from the cell cycle arrest and spindle defects I aimed to identify the underlying mechanism. I reasoned, that there might be a difference in the duration of the enforced AURKA/TPX2 complex formation, being shorter in NMP19$^{-/-}$ cells and thereby allowing the mitotic cells to repair the defects. For this I took advantage of the DOX-inducible FLAG-AURKA expressing NMP53$^{-/-}$ and NMP19$^{-/-}$ cell lines (see Figure 13 B and Figure 14 C) and performed a Co-IP kinetic for FLAG-AURKA of synchronized cells for up to 12 h with and without LN3350 treatment (Figure 21 A). I found that in NMP53$^{-/-}$ cells the tethered AURKA/TPX2 interaction is maintained until 8 h post treatment (Figure 21 B). In line with this, I also observed a stabilization of TPX2 up to 8 h and AURKA up to 6 h in the input samples (Figure 21 C). Similarly, in NMP19$^{-/-}$ cells the compound-induced AURKA/TPX2 complex maintained until 8 h post treatment (Figure 21 D) and also AURKA and TPX2 were stabilized up to 6 h and 8 h in the input samples, respectively (Figure 21 E).

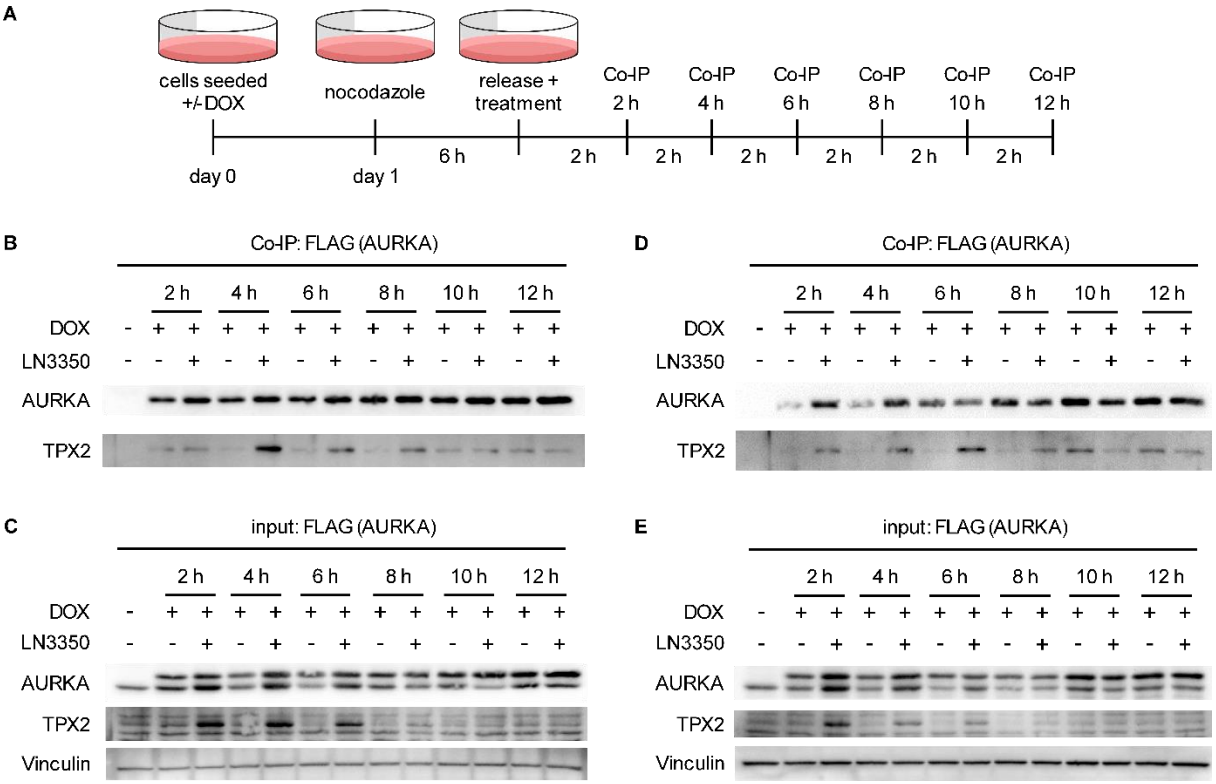

Figure 21*: A)* Experimental outline of the Co-IP kinetic experiments of NMP53$^{-/-}$ and NMP19$^{-/-}$ cells upon treatment with 60 nM LN3350 or DMSO. **B and C)** Western blot for AURKA and TPX2 of Co-IP kinetic lysates (B) and the corresponding input (C) lysates from NMP53$^{-/-}$ cells stably expressing DOX-inducible FLAG-AURKA after synchronization with nocodazole followed by release and treatment with 60 nM LN3350 or DMSO as control for the

indicated timepoints. (n = 1 each) **D and E)** Western blot for AURKA and TPX2 of Co-IP kinetic lysates (D) and the corresponding input (E) lysates from NMP19$^{-/-}$ cells stably expressing DOX-inducible FLAG-AURKA after synchronization with nocodazole followed by release and treatment with 60 nM LN3350 or DMSO as control for the indicated timepoints. (n = 1 each)

To validate the results of the Co-IP kinetics, I performed the same experiment with NMP53$^{-/-}$ and NMP19$^{-/-}$ cells stably expressing the DOX-inducible FLAG-TPX2 construct (see Figure 15 B and C). Again, I found an increased AURKA/TPX2 binding in NMP53$^{-/-}$ cells (Figure 22 A), as well as a stabilization of TPX2 (Figure 22 B) up to 8 h and AURKA up to 6 h post treatment. Similarly, in NMP19$^{-/-}$ cells, I also observed an enforced AURKA/TPX2 complex formation (Figure 22 C) and a stabilization of AURKA and TPX2 in the input samples until 6h and 8 h post treatment (Figure 22 D).

The deregulation of the mitotic spindle dynamics leads to the prolonged activation of the SAC. Thereby, duration and intensity of the SAC determines cell fate by downregulating cyclin B (via APC/C) or MCL1 (via p38, JNK or CKII). Dependent on which protein reaches the threshold first, MCL1 upon strong SAC activation or cyclin B upon weak SAC activation, cells undergo either cell death or mitotic slippage[120].
To examine, if the difference in the sensitivity of NMP53$^{-/-}$ and NMP19$^{-/-}$ cells towards the AURKA-ligands could be determined by different levels of SAC activation, I analyzed cyclin B, phospho p38 (T180/Y182), p38, MCL1 and apoptosis marker cleaved caspase 3 levels in input lysates of the FLAG-TPX2 Co-IP kinetics. NMP53$^{-/-}$ cells exhibited increased cyclin B levels, starting to decline again 6 h post treatment with LN3350, indicating transient mitotic arrest. Simultaneously, treated cells show increased phosphorylation of p38 at T180/Y182 accompanied with decreased levels of MCL1 and induction of cleaved caspase 3 levels starting 4 h and peaking at 8 h post treatment. The same pattern of cyclin B, phospho p38 and cleaved caspase 3 upregulation and MCL1 downregulation appeared 12 h post treatment, suggesting mitotic catastrophe in NMP53$^{-/-}$ cells (Figure 22 B, lower panel).
NMP19$^{-/-}$ cells treated with LN3350 also transiently arrest in M phase, as indicated by increased cyclin B levels which start to decrease at 8 h post treatment. However, although I also observed an induction of phospho p38 and cleaved caspase 3 around 4 to 10 h post treatment, MCL1 levels are constant over time, suggesting that induction of cell death is not primarily related to mitotic catastrophe (Figure 22 D, lower panel).

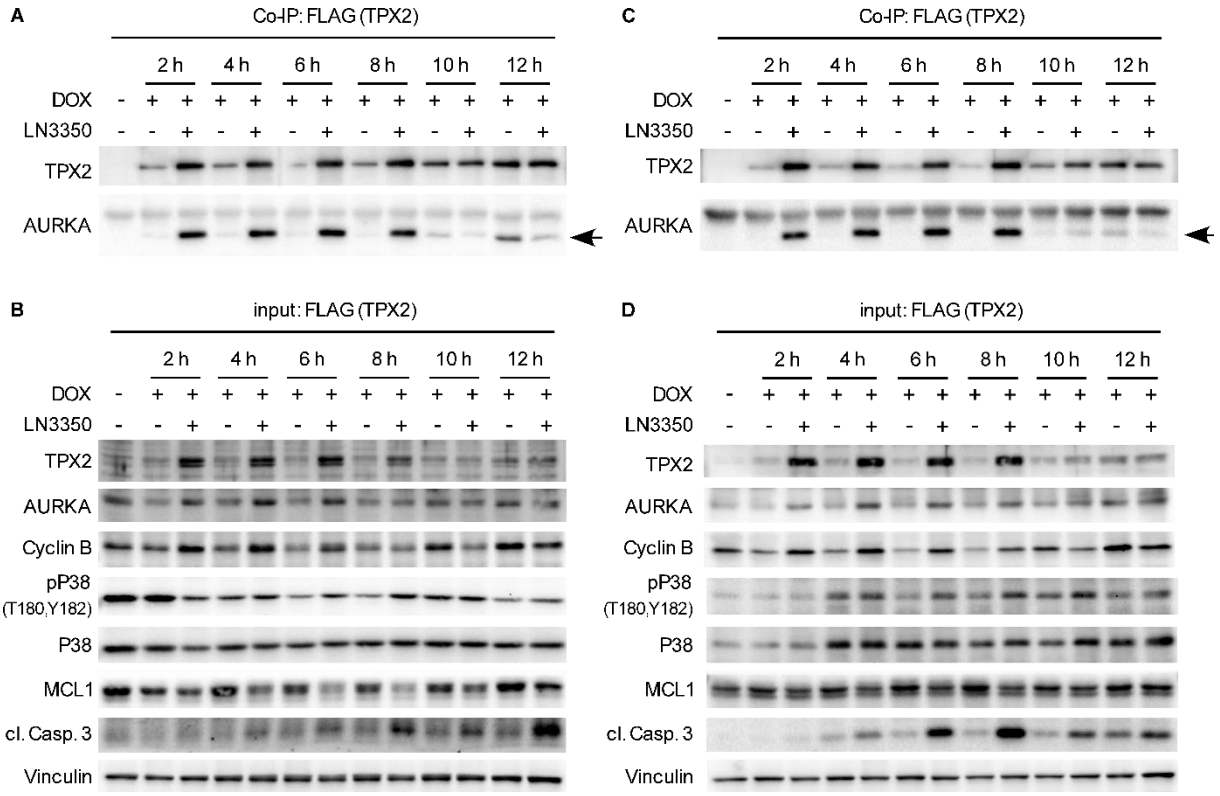

Figure 22: A and B) Western blot for TPX2 and AURKA of Co-IP kinetic lysates (A) and TPX2, AURKA, Cyclin B, phospho P38 (T180, Y182), P38, MCL1 and cleaved caspase 3 for the corresponding input lysates (B) from NMP53$^{-/-}$ cells stably expressing DOX-inducible FLAG-TPX2 after synchronization with nocodazole followed by treatment with 60 nM LN3350 or DMSO as control for the indicated timepoint. (n = 1 each) **C and D)** Western blot for TPX2 and AURKA of Co-IP kinetic lysates (C) and TPX2, AURKA, Cyclin B, pP38 (T180, Y182), P38, MCL1 and cleaved caspase 3 for the corresponding input lysates (D) from NMP19$^{-/-}$ cells stably expressing DOX-inducible FLAG-TPX2 after synchronization with nocodazole followed by treatment with 60 nM LN3350 or DMSO as control for the indicated timepoint. (n = 1 each)

To further examine if cell death is dependent on the SAC intensity and MCL1 levels, I assessed the synergy of the AURKA-ligands with additional MCL1 inhibition. For this I conducted combinatorial treatments of LN3350, LN3352 and MLN8237 with the MCL1 inhibitor S63845 in NMP53$^{-/-}$ and NMP19$^{-/-}$ cells. I treated the cells with different concentrations of S63845 and a 2-fold serial dilution of either LN3350 (7.5 nM – 60 nM), LN3352 (30 nM – 240 nM) or MLN8237 (30 nM – 240 nM). Additionally, each dilution of S63845 was then combined with each dilution of LN3350, LN3352 or MLN8237 (Figure 23 A). Three days after treatment XTT assays were performed and synergism calculated using the software SynergyFinder 2.0[121] and the HSA synergy model. Synergy distribution of the tested conditions is shown in a plot, whereby synergistic areas are depicted as red and antagonistic areas as green. The color code above the plot assigns values to the color gradient shown in the plot. The closer the value is to 10 or above, the more trustful the synergism. Additionally, the most synergistic area is highlighted in the plot and two synergy scores are calculated

estimating the synergism of the most synergistic area and the overall synergism of all tested conditions.

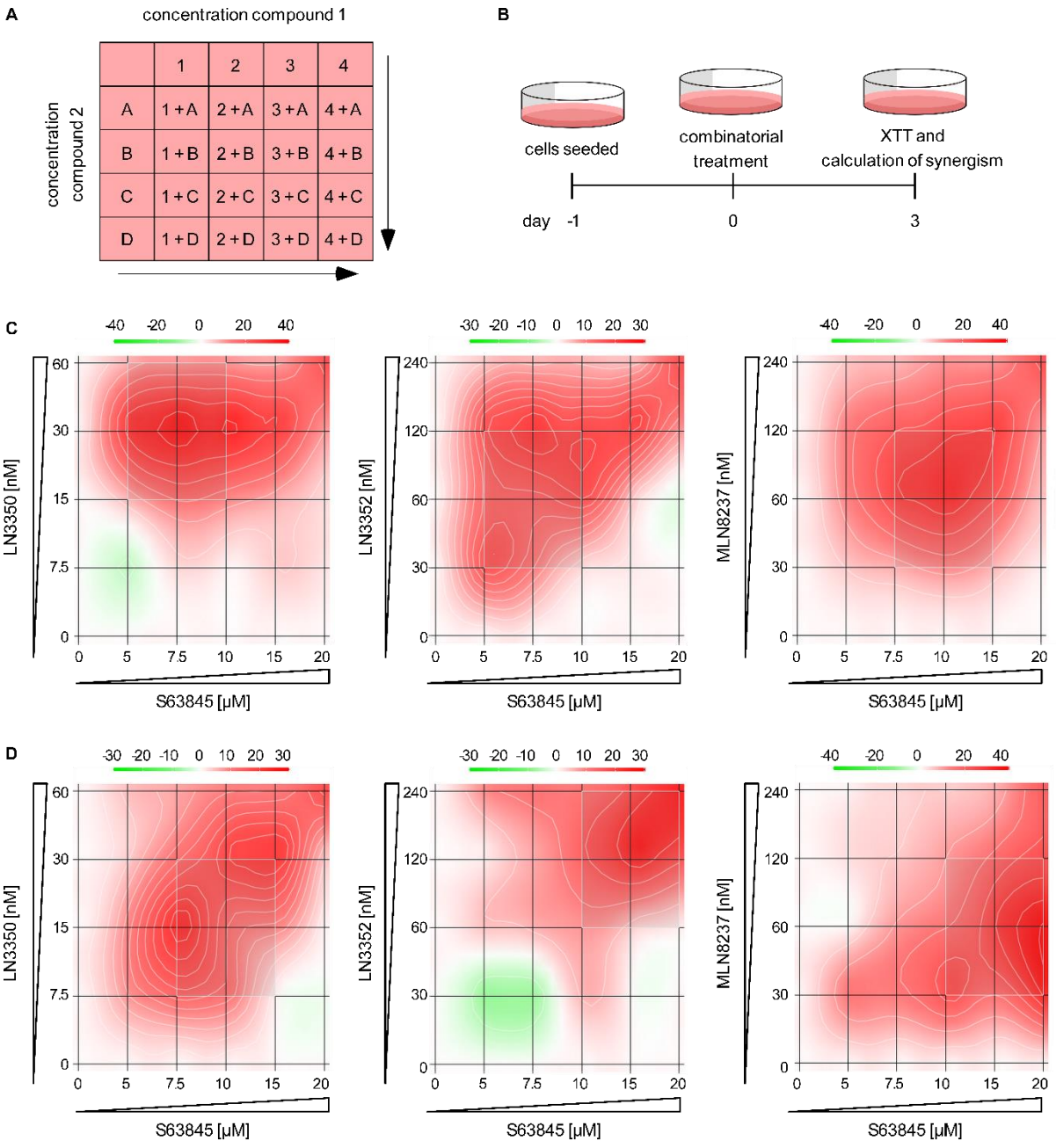

Figure 23: A) Treatment scheme for the combinatorial treatment. **B)** Experimental timeline for the XTT viability assay. **C and D)** Synergy plot of NMP53$^{-/-}$ cells (C) and NMP19$^{-/-}$ cells (D) after the combinatorial treatment with the MCL1 inhibitor S63845 and LN3350 (left), LN3352 (middle) and MLN8237 (right) as calculated with the software SynergyFinder 2.0 using the HAS model. Shown is the mean of 2 independent experiments for all combinations in NMP53$^{-/-}$ cells and 1 experiment each for all combinations in NMP19$^{-/-}$ cells. Red indicates synergism, green indicates antagonism. The most synergistic area is highlighted in the plot.

Indeed, in NMP53$^{-/-}$ cells I found that the combination treatment with S63845 and either LN3350, LN3352 or MLN8237 is synergistic with scores of 20.69, 15.76 and 23.45 in the most synergistic areas, as shown in the plots (Figure 23 C). The overall synergy

scores comprising all tested conditions are 13.46 for LN3350, 9.85 for LN3352 and 15.91 for MLN8237. Also in NMP19$^{-/-}$ cells the treatment with S63845 and either LN3350, LN3352 or MLN8237 had synergistic effects, showing most synergistic area scores of 13.2, 13.7 and 22.7, as well as overall synergy scores of 8.9, 6.9 and 14.1, respectively (Figure 23 D).

This suggests, that MCL1 inhibition sensitizes NMP19$^{-/-}$ cells towards the AURKA-ligands making them as responsive as NMP53$^{-/-}$ cells.

3.6 Sensitivity towards AURKA-ligands of *Trp53*-deficient cells is not affected by p19^{ARF}

To clarify, if the knockout of *Trp53* is essential for the sensitivity or if the knockout of *Cdkn2a^{ARF}* (p19^{ARF}) is mediating resistance, I took advantage of the double knockout cell line NMP19$^{-/-}$x53$^{-/-}$, that was generated by Dr. Ramona Rudalska from murine tumor tissue previously. For a direct comparison, I treated all three cell lines with LN3350, LN3352 and MLN8237 for 5 days (Figure 24 A). The macroscopic phenotype of NMP19$^{-/-}$x53$^{-/-}$ cells after treatment with LN3350 and LN3352 was comparable to treated NMP53$^{-/-}$ cells. Both cell lines showed massive detachment of cells while the majority of remaining cells appeared to be multinucleated (Figure 24 B, lower panels). NMP19$^{-/-}$ cells only showed a lower number compared to DMSO control but almost no cell detachment or multinucleation could be observed. MLN8237, however, led to cell detachment and multinucleated appearance in all three cell lines (Figure 24 B). Cell death analysis using PI staining and subsequent flow cytometry analysis confirmed that LN3350 and LN3352 led to an induction of around 60% and 65% cell death in NMP19$^{-/-}$x53$^{-/-}$ cells (Figure 24 C and D). MLN8237 also induced a comparable cell death induction of around 70%, respectively (Figure 24 E).

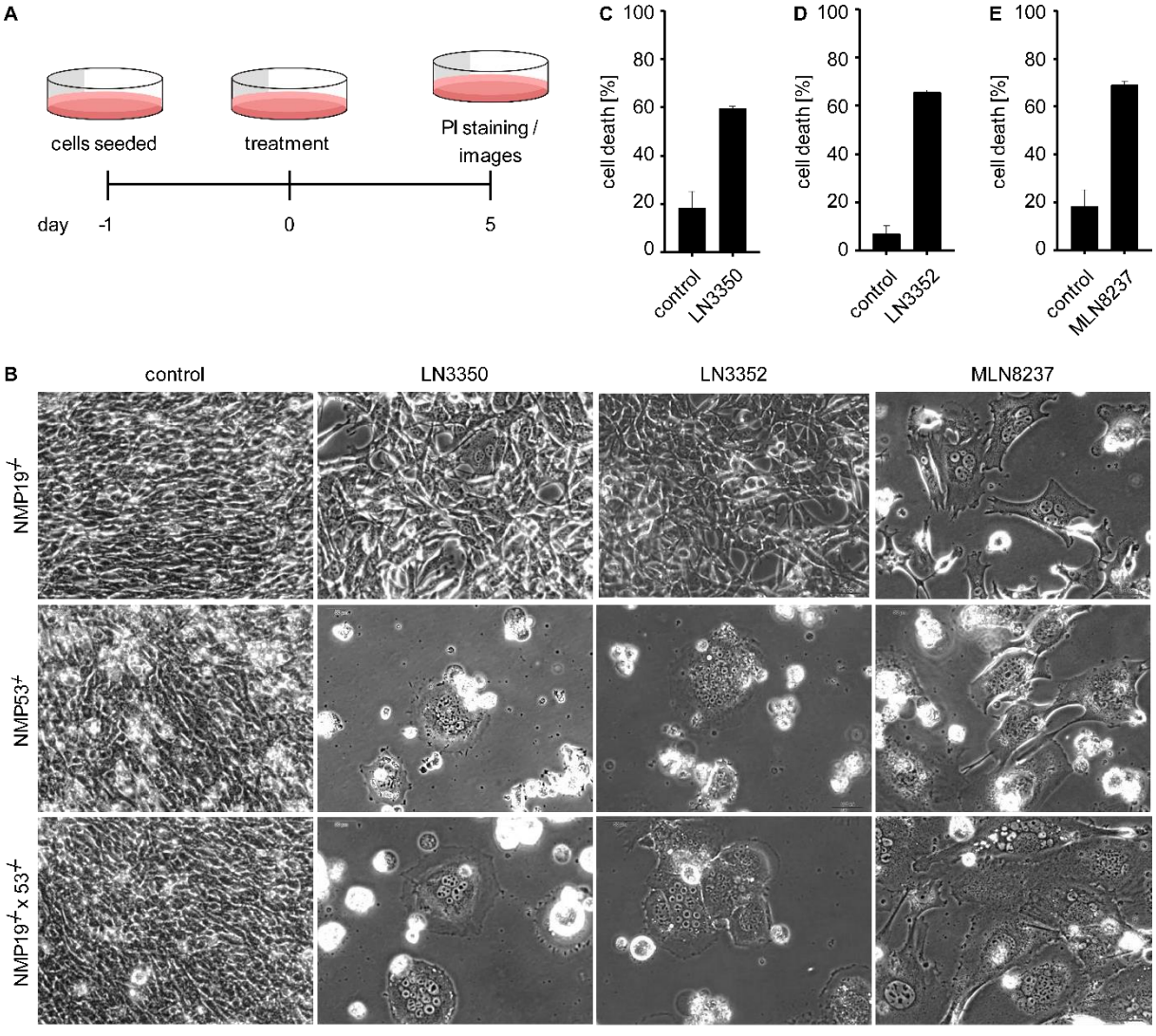

Figure 24: A) Experimental outline of cell death determination with propidium iodide upon treatment is shown. **B)** Representative photographs of NMP19$^{-/-}$ (top), NMP53$^{-/-}$ (middle) and NMP19$^{-/-}$x53$^{-/-}$ (bottom) cells after 5 d of treatment with 60 nM LN3350, 240 nM LN3352, 200 nM MLN8237 or DMSO as control. **C-E)** Quantification of propidium iodide positive NMP19$^{-/-}$x53$^{-/-}$ cells after 5 d of treatment with 60 nM LN3350 (C), 240 nM LN3352 (D), 200 nM MLN8237 (E), or the corresponding DMSO concentrations. Mean with SEM is shown (n = 1; 2 technical replicates).

To further characterize the effect of the AURKA-ligands on NMP19$^{-/-}$x53$^{-/-}$ cells, I calculated the percentage of abnormal spindles upon treatment as shown in Figure 20 A and B. 1 h after treatment with LN3350, LN3352 and MLN8237, I observed the formation of abnormal spindles in 85% - 100% of all mitotic cells (Figure 25 A-C). This phenotype was stably maintained until 48 h post treatment and showed no recovery as seen in NMP19$^{-/-}$ cells (Figure 20 F and G). Accordingly, cell cycle analysis revealed that LN3350 and LN3352 led to a profound G2/M arrest from 6 h up to 16 h, followed by an increasing amount of cell death (subG1) and polyploid cells at 24 h and 48 h post treatment (Figure 25 D and E).

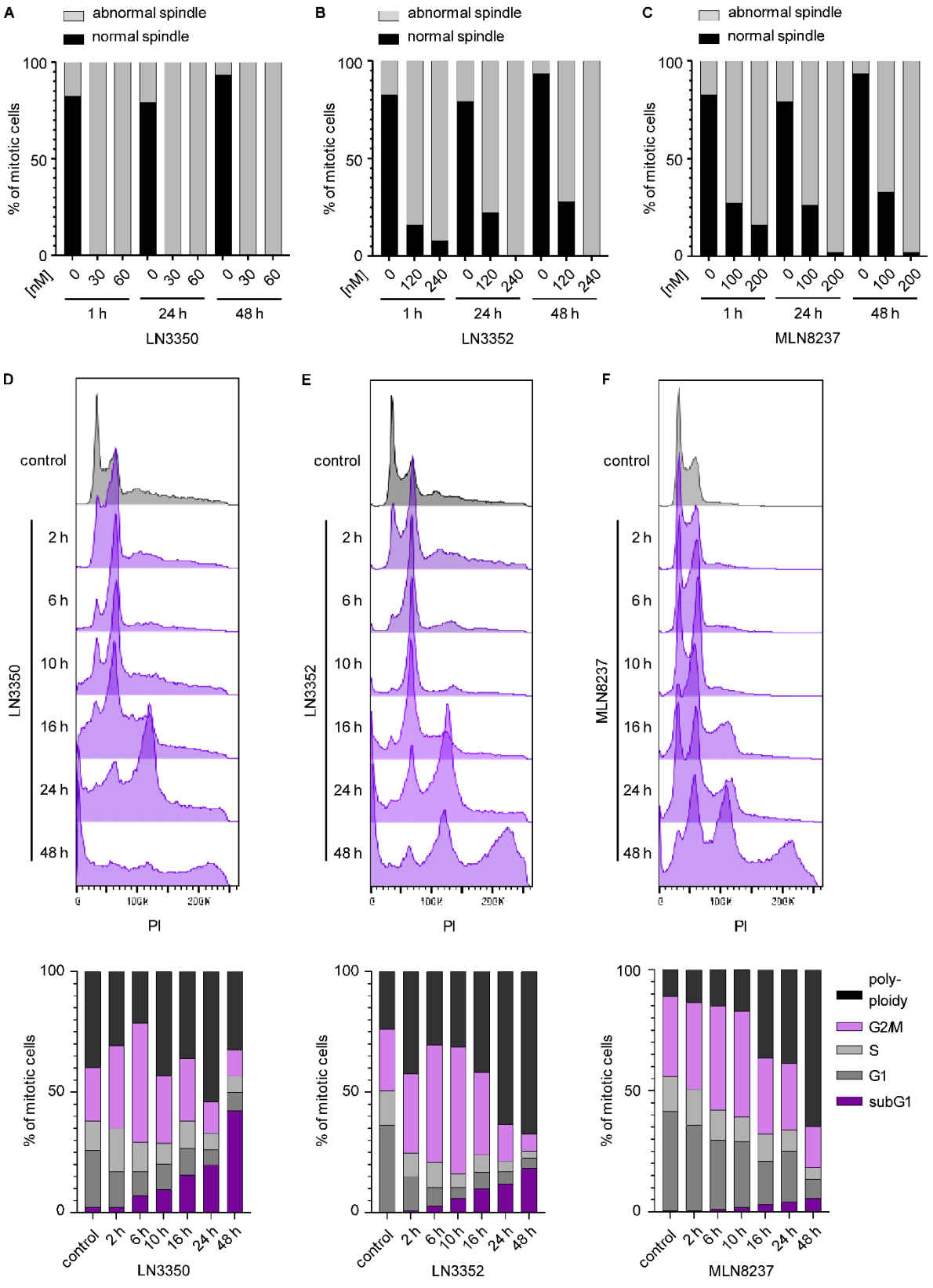

Figure 25: A-C) Quantification of normal or abnormal spindles in mitotic NMP19$^{-/-}$x53$^{-/-}$ cells after 1 h, 24 h and 48 h post treatment with the indicated concentrations of LN3350 (A), LN3352 (B), MLN8237 (C) or the highest corresponding DMSO concentration. (n = 1). 20 to 33 cells per condition were counted. **D-F)** Representative cell cycle analysis and quantification of cell cycle distribution, as determined by DNA staining with propidium iodide, of NMP19$^{-/-}$x53$^{-/-}$ cells at the indicated time points after treatment with 60 nM LN3350 (B), 240 nM LN3352 (C), 200 nM MLN8237 (D) or DMSO as control. (n = 2 for LN3350 and MLN8237, n = 1 for LN3352).

Also for MLN8237 I observed a pronounced G2/M arrest and the induction of polyploidy starting from 16 h up to 48 h (Figure 25 F). However, there was only a slight increase in cell death up to 48 h.

Taken together, the similarity in the treatment response of NMP19$^{-/-}$x53$^{-/-}$ cells and NMP53$^{-/-}$ cells suggests that the sensitivity of cells towards the AURKA-ligands is dependent on the loss of *Trp53* and not the presence of *Cdkn2a*^{ARF}. Overall my data suggest that in *Trp53*-deficient cells AURKA-ligands induce cell death by mitotic catastrophe. In those cells, LN3350 and LN3352 favor the formation of abnormal spindles in mitotic cells which subsequently leads to mitotic arrest most likely due to the activation of the SAC. The activated SAC induces the downregulation of MCL1, which in turn leads to cell death (see Figure 26 left). In *Trp53* wildtype cells the AURKA-ligands initially also induce the formation of abnormal spindles, activation of the SAC and mitotic arrest. However, in contrast to *Trp53*-deficient cells, they maintain a stable MCL1 protein level and can rescue the spindle phenotype, leading to normal cell division (Figure 26 right).

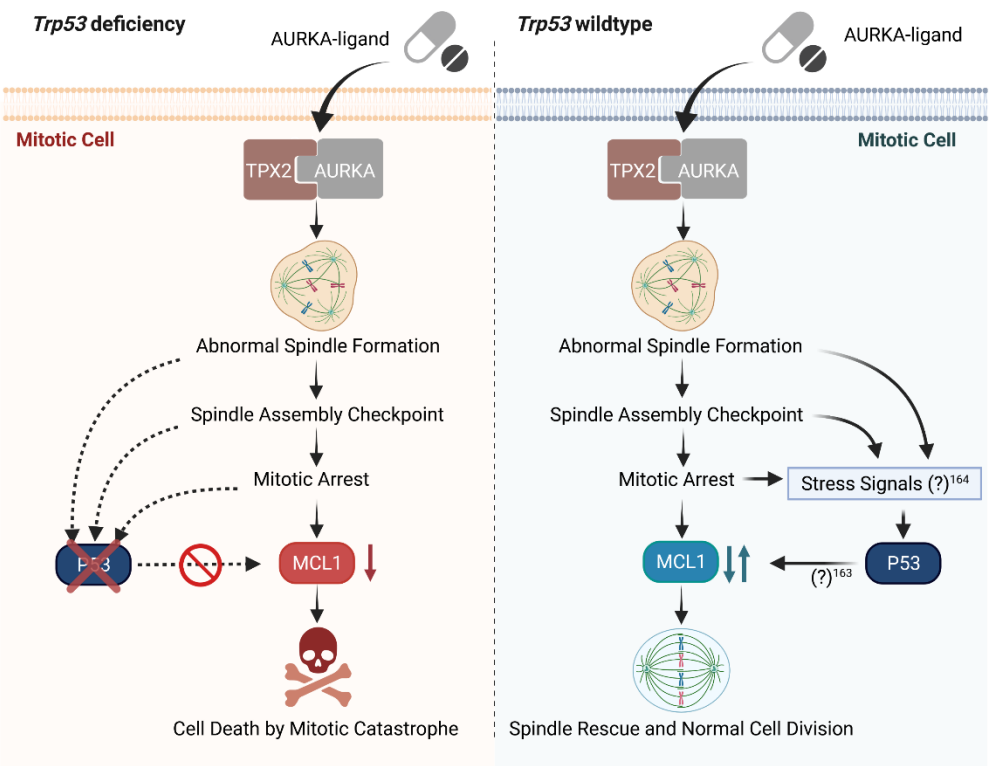

Figure 26: Summary of the observed phenotype in *Trp53*-deficient and *Trp53* wildtype cells upon treatment with AURKA-ligands (generated with Biorender).

3.7 AURKA-ligands also induce growth inhibition and abnormal spindles in human *TP53*-altered liver cancer cells

Since I could show, that the loss of *Trp53* confers sensitivity of murine HCC cells towards AURKA-ligands, I next wanted to test their therapeutic potential in human liver cancer cells. I screened a panel of 6 human liver cancer cell lines with different *TP53* status, as determined by the cancer cell line encyclopedia (CCLE) by the broad institute of MIT and Harvard. The *TP53* status was ranging between *TP53* wildtype (JHH1, HepG2), null (Hep3B) or mutated (Huh7 [Y220C], HLF [G244A], HLE [G244A], both mutations are functionally inactive as assessed by IARC *TP53* database of the international agency for the research of cancer) (Figure 27 A). Using XTT assays, I generated dose-response curves for LN3350, LN3352 and MLN8237 for all 6 cell lines. Next, I calculated the IC_{95} for each compound for the most sensitive cell line Huh7 (LN3350: 85.4 nM, LN3352: 298.5 nM) (Figure 27 B and C). This analysis, however, was not possible for MLN8237, since none of the cell lines reached an inhibition of 95% upon treatment (Figure 27 D). I then determined the inhibitory effect of LN3350 and LN3352 using these IC_{95} concentrations on the other 5 cell lines. While JHH1 and HepG2 only showed a slight growth inhibition of 15.9% and 8.8% for LN3350 and 24.6% and 14.1% for LN3352, respectively, Hep3B, HLE, HLF and Huh7 showed inhibitions ranging from 67.8% to 96.1% for LN3350 and 71.2% to 94.4% for LN3352 (Figure 27 E and F). I then grouped the calculated inhibition values (%) of the *TP53* wildtype cells (JHH1 and HepG2) and the TP53-altered cell lines (Huh7, HLE, HLF and Hep3B) for each compound and plotted them against each other. This showed that both, LN3350 and LN3352, were significantly more effective in *TP53*-altered human liver cancer cell lines, with 83.3% ± 14.9% and 80.7% ± 15.7% inhibition, compared to *TP53* wildtype lines, with 13.3% ± 7.8% and 20.6% ± 14% inhibition, respectively (Figure 27 G and H).

A

cell line	Huh7	HLF	HLE	Hep3B	JHH1	HepG2
TP53 status	mut (Y220C)	mut (G244A)	mut (G244A)	null	wt	wt

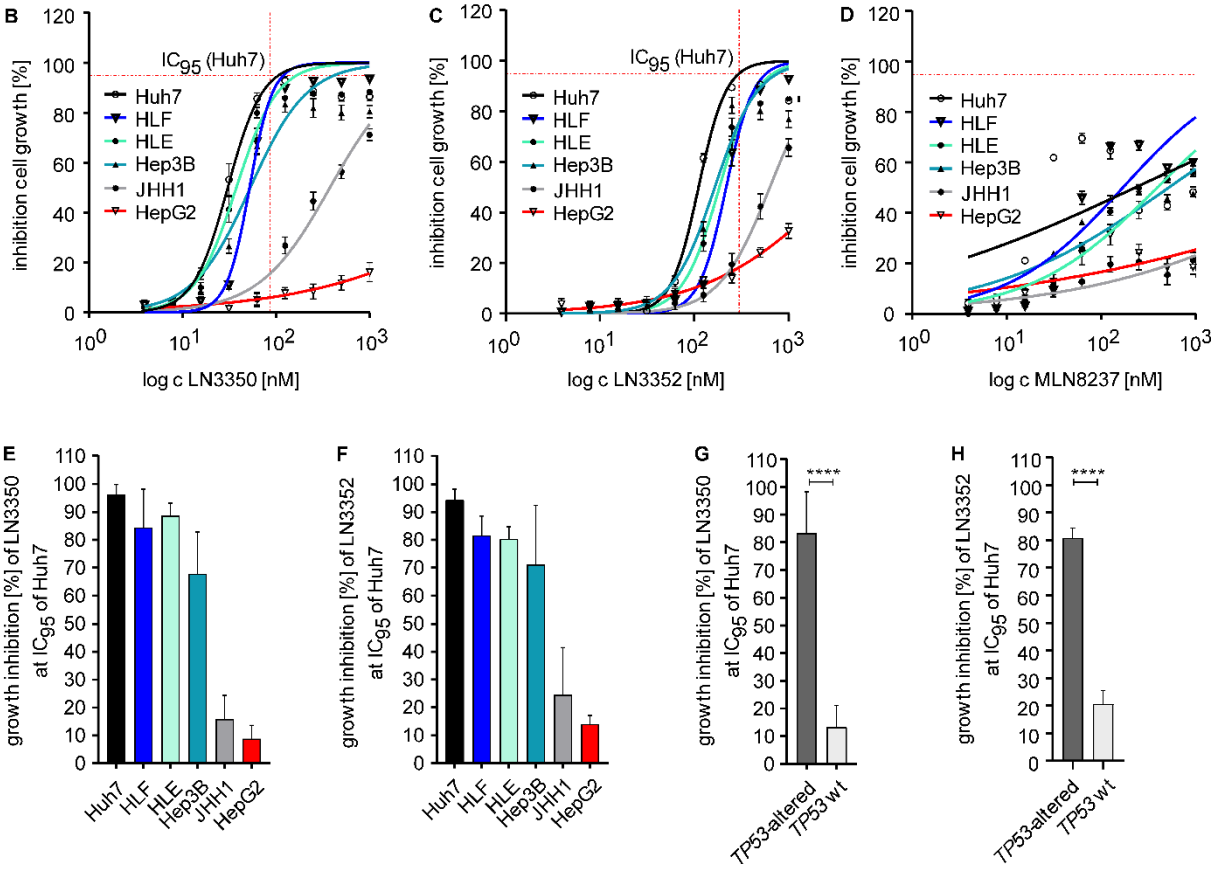

Figure 27: A) Tested human liver cancer cell lines and their *TP53* status. mut = mutated, null = knockout, wt = wildtype. **B-D)** Dose-response curves using XTT viability assays of the cell lines shown in A after 3 d treatment with a 2-fold serial dilution of LN3350 (B), LN3352 (C) and MLN8237 (D), starting from 1 µM. Shown is the summary of 3-5 independent measurements with SEM, as well as the interpolated IC_{95} for the Huh7 cells (red dashed lines). **E and F)** Quantification of the growth inhibition of LN3350 (E) and LN3352 (F) in Huh7, HLH, HLE, Hep3B, JHH1 and HepG2 cells at the IC_{95} concentrations of each compound in Huh7 cells as determined in B and C. Shown is the mean with SEM. n = 3-5 each. **G and H)** Comparison of the growth inhibition of LN3350 (G) and LN3352 (H) in the human liver cancer cell lines shown in E and G grouped into *TP53*-altered (Huh7, HLF, HLE, Hep3B) and *TP53* wildtype (JHH1 and HepG2) at the IC_{95} concentrations of each compound in Huh7 cells as determined in B and C. Shown is the mean with SEM. Significance was calculated using the student's t-test, n = 3-5 each, **** p<0.0001

I next wanted to test, if the long-term spindle phenotype observed in murine *Trp53*-deficient HCC cells upon treatment with the AURKA-ligands also occurs in human liver cancer cells. For this I compared spindle phenotypes of the *TP53* null cell line Hep3B and the *TP53* wildtype cell line HepG2 upon treatment. I stained α-Tubulin and counted mitotic cells with normal and abnormal spindles as described in Figure 20 A and B. At 24 h, I observed in Hep3B cells a concentration-dependent formation of abnormal spindles in up to 100% of mitotic cells for LN3350 and 97% of mitotic cells for LN3352 at the highest concentration tested (Figure 28 A and B). This phenotype was

maintained until 48 h post treatment. Also in HepG2 cells, LN3350 and LN3352 led to concentration-dependent spindle defects in up to 93% and 100% of mitotic cells after 24 h, respectively (Figure 28 D and E). However, HepG2 cells could recover from the defects, revealing only 25% - 50% of mitotic cells harboring abnormal spindles at 48 h post treatment.

As observed in murine HCC cells (compare Figure 20 E and H), MLN8237 provoked the formation of abnormal spindles that were stable until 48 h in *TP53* null and wildtype human cells, indicating that the mechanism of action of MLN8237 on the spindles is not dependent on the *TP53* status (Figure 28 C and F).

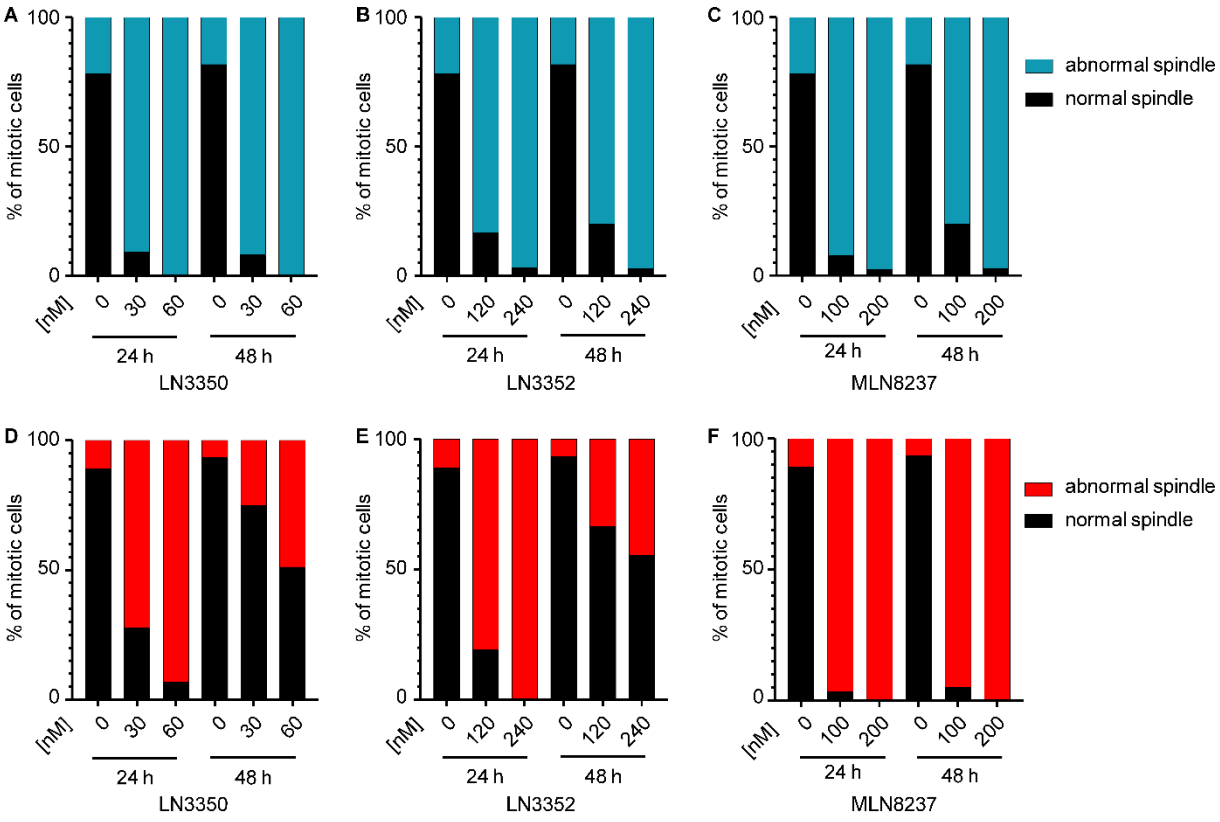

Figure 28: Quantification of normal or abnormal spindles in mitotic *TP53* null Hep3B **(A)** and *TP53* wildtype HepG2 **(B)** cells after 24 h and 48 h after treatment with the indicated concentration of LN3350, LN3352, MLN8237 or the highest corresponding DMSO concentration. (n = 1)

3.8 *RB1* alteration increases sensitivity of *TP53*-altered human lung cancer cells towards AURKA-ligands

It was recently published, that lung cancer cells with loss of the tumor suppressor *RB1* are hypersensitive towards AURKA inhibition[109]. *RB1* loss leads to an E2F-dependent upregulation of stathmin, which in turn induces the destabilization of the spindle

microtubules and activation of the SAC[122]. Further, the tested *RB1*-deficient lung cancer cells also have mutated *TP53*, as assessed by the COSMIC database, thus, I reasoned that the AURKA-ligands might also inhibit lung cancer cells depending on their *TP53* and *RB1* status.

To test this hypothesis, I screened a panel of 6 NSCLCs (NCI-H460, A549, NCI-H226, NCI-H1299, Calu-1, NCI-H23) and 4 SCLCs cell lines (DMS-53, NCI-H446, NCI-H69, COR-L279). According to COSMIC database I then annotated their *TP53* and *RB1* mutation status, with the exception of Calu-1, which was not listed in the COSMIC database (Table 9 and Table 10).

Table 9: *TP53* and *RB1* status of the NSCLC cell lines

NSCLC line	**NCI-H460**	**A549**	**NCI-H226**	**NCI-H1299**	**Calu-1**	**NCI-H23**
TP53 status	wt	wt	wt	null	null[123]	mut (p.M246I)
RB1 status	wt	wt	wt	wt	wt[109]	wt

Table 10: *TP53* and *RB1* status of the SCLC cell lines. [#]CCLE = cancer cell line encyclopedia

SCLC line	**DMS-53**	**NCI-H446**	**NCI-H69**	**COR-L279**
TP53 status	mut p.E56* (het) p.S241F (het)	mut p.G154V (hom)	mut p.E171* (hom)	mut c.376-4_384del (hom) p.TVL126fs (CCLE[#])
RB1 status	wt	mut (c.1961-2A>T)	mut p.E748* (hom)	mut c.1498+5G>C (hom) c.1050-15C>T (hom)

I first generated dose-response curves using XTT assays for all cell lines with LN3350, LN3352 and MLN8237. I then calculated the IC_{95} of each compound for the most sensitive cell line, which was COR-L279 for LN3350 (IC_{95} = 78.6 nM) and LN3352 (IC_{95} = 232.6 nM), and NCI-H446 for MLN8237 (IC_{95} = 29 nM) (Figure 29 A-C). Next, I determined for each compound the percentage of growth inhibition at the calculated IC_{95} for all cell lines. I observed growth inhibition rates ranging from 15% to 95% among all cell lines (Figure 29 D-F). To evaluate the effect of *TP53* and *RB1*, I grouped the calculated inhibition values (%) of the cell lines according to the mutation status, showing that *TP53* mutation alone does not confer sensitivity towards the AURKA-ligands. For LN3350 the average inhibition of 33.8% ± 12.3% in double wildtype cells

was only increased to 36.2% ± 12.2% in *TP53*-altered cells (Figure 29 G). A similar result was obtained for LN3352, where the average inhibition of 32.3% ± 17.1% in double wildtype cells was increased to only 36.7% ± 12.6% in *TP53*-altered cells (Figure 29 H). However, in *TP53* and *RB1* double mutated cells, which are all SCLC, treatment with LN3350 and LN3352 induced an average inhibition of 94.3% ± 3.2% and 92.9% ± 4.7%, respectively. For MLN8237 the average inhibition of 20.5% ± 9.7% in double wildtype cells could not be increased in *TP53*-mutated cells (21.6% ± 11.2%). *RB1* and *TP53* double mutated cells showed the highest response towards MLN8237 with 91.7% ± 8.9%, which was significantly better than wildtype or *TP53*-mutated cells (Figure 29 I).

Taken together, I could show that the AURKA-ligands could be a potential therapeutic option not only for *TP53*-altered liver cancers, but also for *TP53*-and *RB1*-mutated lung cancer cells and potentially other *TP53*-altered cancer entities harboring additional mutations.

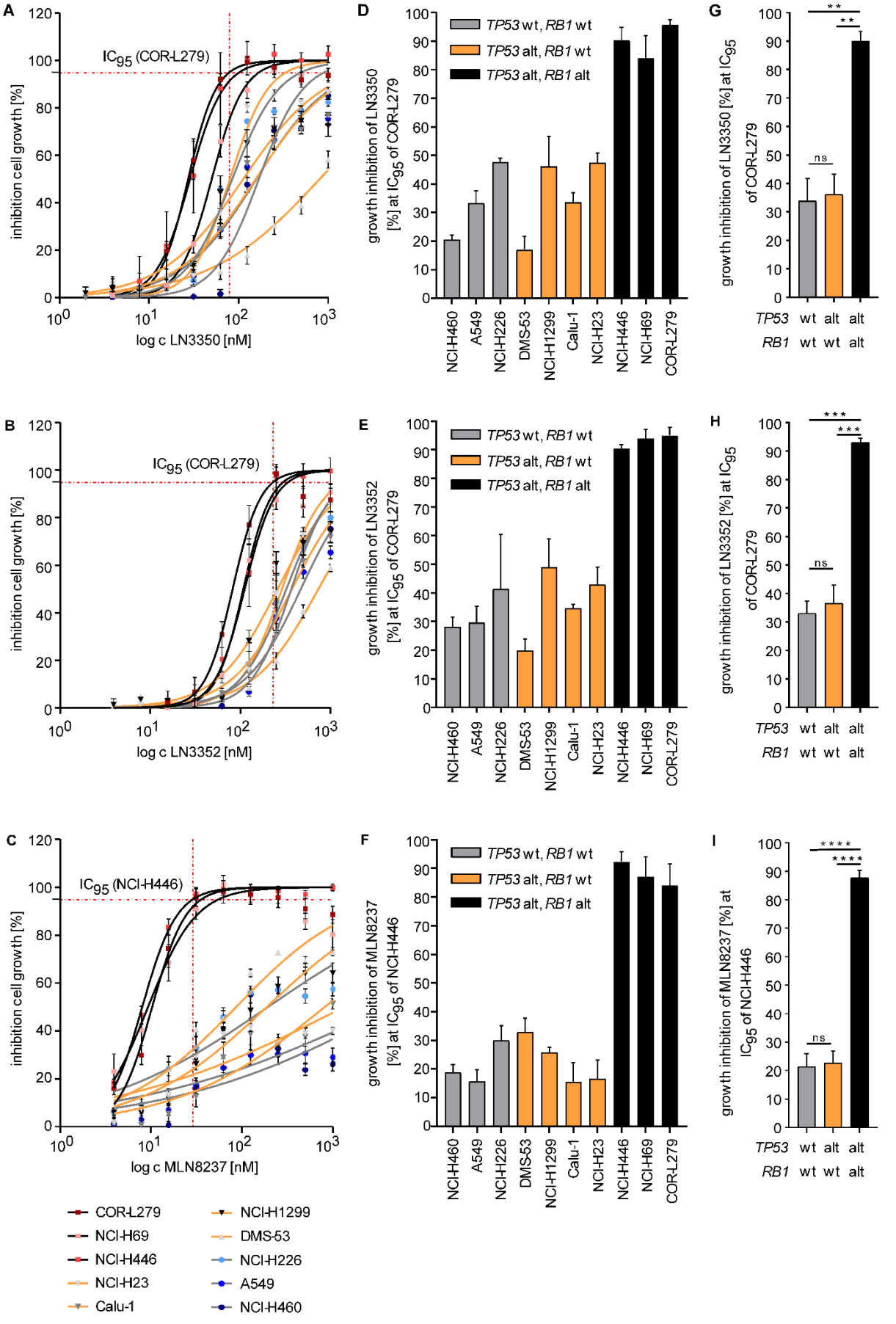
A
B
C
D
E
F
G
H
I
IC95 (COR-L279)
IC95 (NCI-H446)
inhibition cell growth [%]
log c LN3350 [nM]
log c LN3352 [nM]
log c MLN8237 [nM]
growth inhibition of LN3350 [%] at IC95 of COR-L279
growth inhibition of LN3352 [%] at IC95 of COR-L279
growth inhibition of MLN8237 [%] at IC95 of NCI-H446
TP53 wt, RB1 wt
TP53 alt, RB1 wt
TP53 alt, RB1 alt
NCI-H460
A549
NCI-H226
DMS-53
NCI-H1299
Calu-1
NCI-H23
NCI-H446
NCI-H69
COR-L279
TP53 wt alt alt
RB1 wt wt alt
ns
**
***
****

Figure 29: A-C) Growth inhibition dose-response curves conducted with XTT viability assays of the indicated cell lines (see bottom) after 3-5 d treatment with a 2-fold serial dilution of LN3350 (A), LN3352 (B) and MLN8237 (C), starting from 1 µM. Shown is the summary of 3-5 independent measurements with SEM, as well as the interpolated IC_{95} for most sensitive cell line (COR-L279 for A and B, NCI-H446 for C; red dashed lines). **D-F)** Quantification of the growth inhibition of LN3350 (D), LN3352 (E) and MLN8237 (F) in the indicated cell lines at the IC_{95} concentrations of each compound in COR-L279 (D and E) or NCI-H446 (F) cells as determined in A-C. Color code indicates the status for *TP53* and *RB1* (grey = *TP53* and *RB1* wildtype; blue = *TP53* wildtype, *RB1*-altered; orange = *TP53*-altered, *RB1* wildtype; black = *TP53*- and *RB*-altered). Shown is the mean with SEM. n = 3-5 each. **G-I)** Comparison of the growth inhibition of LN3350 (G), LN3352 (H) and MLN8237 (I) in the human lung cancer cell lines grouped according to their *TP53* and *RB1* status as shown in D-E. Shown is the mean with SEM. Significance was calculated using ANOVA and the Holm-Sidak's multiple comparisons test, ** $p<0.01$, *** $p<0.001$, **** $p<0.0001$, ns = not significant

4 Discussion

HCC, due to the high mortality rates and increasing incidences, represents a major global health problem. However, there is no accurate surveillance system to detect tumors at an early stage when they are eligible for curative therapy, known to prolong survival[2]. A main target for surveillance would be patients with cirrhosis, since the annual incidence of HCC development amongst those patients reached the threshold of 1.5%, making surveillance cost-effective[2, 124]. However, the results arguing for a survival benefit associated with HCC surveillance in cirrhosis patients are controversial[125, 126]. To date, no high-quality randomized, controlled trials on the effectiveness of HCC screening on cirrhosis patients have been conducted[2]. Therefore, in contrast to patients with liver dysfunction amenable for liver transplantation, patients with cirrhosis are not eligible for cancer surveillance[2].

Upon HCC diagnosis the only potentially curative treatment options are surgical resection or liver transplantation[11, 127]. However, patients with HCC are often in a poor health state, limiting the option to undergo surgery. Additionally, although liver transplantations are the second most common solid organ transplantations, the limited amount of donor organs is a huge problem and meets only 10% of global demands[127]. Compared with other European countries, the liver donation rate in Germany is very low[128]. According to the “Deutsche Stiftung Organtransplantationen” (DSO), 1416 patients were (re-)added on the German liver transplantation list in 2020. However, only 826 transplantations were conducted out of which only 52 living donations of the liver were made. In the same year, 217 listed patients died while waiting for an organ. Upon successful liver transplantation, the general 5-year survival rate is approximately 70%, however, obesity (an BMI ≥35 kg/m^2) and age (>60 years) can have a negative influence on the mortality[129, 130]. This might suggest a decrease in future survival rates due to the steady increase in obesity and the aging of society.

Another problem is that liver transplantation is only feasible for early stage HCC, but most patients present with an advanced HCC stage[1, 12]. Unfortunately, all currently approved first- or second-line drugs for advanced HCC prolong survival only for a few months and have severe side-effects, thereby highly impacting the life of patients[16-22]. Accordingly, aiming to improve efficacy and safety, several inhibitors against molecular targets have been tested in clinical studies, some of which progressed to phase III

trials, however with negative results[131]. For example, the EGFR-inhibitor erlotinib, the VEGFR and PDGFR inhibitors sunitinib and linifanib, as well as the VEGFR, PDGFR and FGFR inhibitor brivanib did not confer any benefit compared to sorafenib in phase III superiority trials, with linifanib even inducing more grade 3-4 adverse events[132-135]. Similarly, the mTOR inhibitor everolimus and the cMET inhibitor tivantinib failed to improve survival compared to placebo-treated patients in phase III clinical trials[136, 137]. Therefore, there is a high unmet need for novel therapeutic approaches for HCC.

One putative target might be AURKA which is often overexpressed in HCC[24]. Although clinical trials with the AURKA inhibitor MLN8237 in other tumor entities showed promising results, it became clear that the catalytic inhibition of AURKA leads to dose-limiting toxicities[106, 107]. Interestingly, a study published by our group revealed, that *TP53*-deficient HCC are highly sensitive towards a subset of AURKA-inhibitors, that additionally change the conformation of AURKA[70]. Thus, we reasoned that small molecules changing the conformation of AURKA, without inhibiting its kinase activity would minimize the toxic side effects observed with MLN8237.

Together with the group of Prof. Dr. Stefan Laufer and Dr. Tatu Pantsar, we were able to develop first of its kind AURKA-ligands, LN3350 and LN3352. In the TSA a good binding to AURKA could be proven for LN3352, most likely due to its ability to bind to AURKAs ATP-binding pocket, as shown by its kinase inhibition. The hydrogen bonds between LN3352's hingebinder and AURKA's hinge region stabilize the kinase most probably, thereby causing the thermal shift. An additional methyl-group in LN3350's hingebinder most likely blocks the binding to the hinge region, which is also resembled by the prevented kinase inhibition. However, the low thermal shift for LN3350 might be misleading. It could be explained by the highly dynamic character of AURKA and the absence of a crucial interaction of LN3350 to the ordered, highly conserved hinge region of AURKA[138-140]. LN3350 is designed to mainly interact with residues in the highly flexible R-spine region of AURKA and it is known that the TSA has limitations on flexible proteins, since the increase of temperature affects flexible proteins more than rigid ones, which makes it harder to detect a stabilization[141]. Also, an interaction of the ligand with the unfolded protein can also lead to false negative results[142].
Since both compounds, LN3350 and LN3352, contain a fluorine atom, which is usually not found in biomolecules and therefore not present in the AURKA protein, we also

planned to conduct a ^{19}F-NMR to prove binding. Here, the signal detected of the fluorine atom in the AURKA-ligands should be weakened upon binding to AURKA[143]. However, since the compounds are very lipophilic and NMR experiments are conducted with aqueous solutions, the compounds were not soluble enough to perform this experiment.

Second-harmonic generation (SHG) could be another option to prove binding of LN3350 to AURKA. With this method a ligand-induced conformational shift of AURKA could be detected[144]. Here, AURKA is conjugated to a second-harmonic (SH)-active molecule and immobilized on a supported lipid bilayer. Upon laser-induced excitation of the SH-active dye a SHG-signal is detected, whose intensity is strongly dependent on the orientation of the SH-active molecule with respect to the surface. Due to a conformational change, the orientation of the SH-active dye is altered, which results in a signal change.

Another possibility is that the AURKA-ligands prefer binding AURKA efficiently in complex with another protein, e.g. TPX2. To test this hypothesis, *in vitro* PPI-assays with isolated proteins, like ELISA or fluorescent polarization assays could be performed[145, 146].

The ultimate goal to prove binding and picture the binding mode and the induced conformational shift, however, is the generation of a crystal structure of the complex between AURKA and the newly developed ligands, which so far was not successful. Nevertheless, since both compounds, LN3350 and LN3352, showed comparable results in all other conducted assays and structurally only differ in the presence of one methyl-group, it is very likely that both compounds work in the same manner and bind AURKA.

The results of the present study prove that it is possible to uncouple the alteration of the AURKA interactome from its kinase inhibition. Compared to MLN8237, which has a 15-times lower IC_{50} for the isolated kinase than the cellular IC_{50}, LN3352 inhibited isolated AURKA with an IC_{50} of around 260 nM, more than 4 times higher than the cellular IC_{50}. Thereby, it has to be considered that for the isolated kinase drugs do not have to pass any membrane or cannot bind any factors in the cell culture medium, like serum proteins (BSA), as it is possible in a cellular assay *in vitro*[147]. Since LN3352, as well as LN3350, are lipophilic, it is possible that they are able to pass the cellular phospholipid membrane via passive diffusion[148]. However, an experimental validation

is needed to rule out a transporter-dependent uptake. Further, it cannot be excluded that the compounds get at least partially retained at the membrane[149]. Additionally, due to their lipophilicity, they are likely prone to bind unspecifically to BSA or other proteins.

Besides the results on the isolated kinase, I showed, that LN3350 and LN3352 do not inhibit AURKA but rather lead to its kinase activation seen by phosphorylation of AURKA and PLK1 in the cells. This increased activation could be explained with my data showing that AURKA-ligands favor AURKA/TPX2 complex formation, thereby stabilizing TPX2 and AURKA. This is in line with published data, revealing that TPX2 binding stabilizes AURKA[150]. There, it was shown that RNAi-mediated knockdown of *TPX2* leads to proteasome-mediated AURKA degradation. However, the reintroduction of either full-length TPX2 or the AURKA-binding domain of TPX2, but not a truncated TPX2 version lacking the AURKA-binding domain, could restore AURKA levels and even impair its cell cycle-dependent degradation in telophase[150]. It is known that the binding of AURKA to TPX2 does not directly induce the phosphorylation of AURKA, however, TPX2 renders AURKA in an active conformation so that AURKA can autophosphorylate itself and is more accessible to substrates[85, 151]. Besides that, the binding to TPX2 prevents the dephosphorylation of AURKA on Thr288 by PP1[85].

Interestingly, TPX2 and AURKA have been shown to correlate with chromosome instability (CIN), a common feature of solid tumors. In a recent study, the authors determined a CIN score for 10.151 genes using 18 data expression sets[152]. TPX2 and AURKA were among the top 70 candidates with TPX2 even having the highest CIN score. CIN is one of the main features leading to aneuploidy. This is in line with other studies showing that overexpression of TPX2 and AURKA results in the induction of polyploid and multinucleated cells[153, 154]. Indeed, I could also show that LN3350 and LN3352 can induce polyploidy. A main reason for induced polyploidy is a deregulation of spindles. It is known that the deregulation of mitotic spindle dynamics leads to improper attachment of the spindles to the kinetochores[155-157]. This is in line with my data showing that enforced TPX2/AURKA complex formation and subsequent AURKA activation disturb spindle dynamics. Interestingly, this effect is specific for LN3350 and LN3352. MLN8237 also induces abnormal spindle formation and polyploidy, however, it does not induce tethering of the AURKA/TPX2 complex. Instead, it prevents the co-localization of AURKA to TPX2 and the mitotic spindles.

Errors in correct spindle formation can cause improper chromosome segregation. In order to prevent this, cells usually induce a prolonged activation of the SAC[155, 156]. Hereby, the mitotic checkpoint complex (MCC), consisting of MAD2, BUB3, BUBR1 and CDC20 inhibits the APC/C complex and prevents not only the separation of sister chromatids, but also the degradation of cyclin B, which keeps cells arrested in M phase[158, 159]. Consistently, I found increased levels of cyclin B upon treatment with AURKA-ligands. The mitotic arrest induces the activation of p38, CKII and JNK, which in turn phosphorylate the anti-apoptotic factor MCL1, provoking its FBW7-mediated proteasomal degradation and induction of apoptosis[120, 160]. My data imply that this mechanism occurs in a fraction of NMP53$^{-/-}$ cells, since they show increased p38 activation, with simultaneous MCL1 downregulation and induction of cleaved caspase 3. However, at early timepoints NMP19$^{-/-}$ cells also show increased activation of p38 as well as a temporary induction of apoptosis but without downregulation of MCL1. On the one hand it is possible that p38 is not the main factor mediating MCL1 downregulation and subsequent apoptosis in NMP53$^{-/-}$ cells. To shed light into this, the activation status of JNK and CKII should be analyzed in both genotypes as well. Further, it could be tested if the pharmacological inhibition of p38, JNK or CKII prevents downregulation of MCL1 and induction of apoptosis in *Trp53*-deficient cells upon treatment with AURKA-ligands. Vice versa, an increased activation, e.g. by inducible active mutants of p38, JNK or CKII could be used to examine induced sensitization of cells towards treatment with AURKA-ligands[161, 162].

On the other hand it was previously shown that MCL1 is a direct transcriptional target of P53 and that upon induction of stress signals, like the treatment with ABT-737 the pro-apoptotic activity is diminished due to the maintenance of MCL1 levels in a P53-dependent manner[163]. Further it was shown that also mitotic spindle damage can lead to P53 activation[164]. Therefore, it could be possible, that in NMP19$^{-/-}$ cells the abnormal spindle formation, SAC activation and mitotic arrest upon treatment with AURKA-ligands induce stress signals that lead to the activation of P53. This in turn could induce the transcriptional upregulation of MCL1, counteracting the induction of cell death, which is absent in *Trp53*-deficient cells.

However, the duration and intensity of the SAC determine cell fate. An incomplete inhibition of the APC/C complex results in slow but continuous degradation of cyclin B, leading to mitotic exit without proper chromosome segregation (mitotic slippage)[120, 165,

[166]. Therefore, the fate of cells arrested in mitosis is decided by the degradation rate of MCL1 and cyclin B. If MCL1 protein levels are too low to inhibit anti-apoptotic proteins, cells will undergo cell death, in contrast, if cyclin B levels become too low to inhibit mitotic exit, cells will undergo mitotic slippage[120, 165]. The latter seems indeed to be the case for another subset of NMP53$^{-/-}$ cells upon AURKA-ligand treatment as cell death increased over time accompanied by induction of polyploid cells. It can be suggested that these cells, due to endoreduplication and centrosome amplification, already have higher SAC induction per se, leading to increased mitotic catastrophe and cell death rates each round of mitosis.

The results of this study give the first hint that a difference in SAC intensity could make the difference between apoptosis and mitotic slippage upon treatment with AURKA-ligands. To further strengthen this hypothesis, knockout or inhibition of MPS1, the upstream regulator of the SAC[167], could be used to determine, if lowering of the SAC intensity prevents mitotic catastrophe and favors mitotic slippage of *Trp53*-deficient cells upon treatment with AURKA-ligands. Vice versa, combinatorial treatment with the APC/C-inhibitor proTAME, mimicking a strengthened SAC by preventing cyclin B degradation, could reveal if cells are more prone to cell death[168, 169].

However, besides AURKA inhibitors several other anti-mitotic drugs inducing SAC and apoptosis have been used in preclinical and clinical studies with the aim to treat cancer[170, 171]. Amongst those are the clinically used spindle poisons eribulin, which belongs to the group of vinca alkaloids and prevents polymerization of microtubules, and paclitaxel, which belongs to the group of taxanes and stabilizes microtubules[171]. Although those drugs confer a survival benefit for patients, they are accompanied with severe side-effects, like neutropenia, anemia, peripheral neuropathy, nausea, fatigue and hair loss, highly affecting the patient's life quality[171-173]. The reason for this is that spindle-poisons affect all fast-dividing, mitotic cells and therefore have no selectivity.

Another exploited antimitotic target is PLK1, with volasertib, an ATP-competitive drug, being the most advanced inhibitor[174]. Clinical phase I and II trials revealed, that the most common adverse grade 3-4 events were neutropenia, thrombocytopenia and anemia, leading to dose-limiting toxicities and a rather modest overall anti-tumor activity[174-179]. Since PLK1, like AURKA, is an important mitotic kinase, whose catalytic activity is involved in several signaling pathways and biomarker stratifying patients are still missing, those results are not surprising[74]. Nevertheless, it is currently being tested

in combination with cytarabine, an antimetabolite analogue of cytidine, in a clinical phase III trial as first-line treatment for acute myeloid leukemia (AML) patients, which is supposed to be completed in 2021 (NCT01721876).
In contrast to microtubule-affecting drugs or volasertib the AURKA-ligands appear to have a high selectivity for *TP53*-altered cells, thereby promising an improved tolerability.

Interestingly, this *TP53* mutation-dependency upon treatment with the AURKA-ligands is mainly correlated to induction of cell death. Although also in human cells there was a strong tendency that *TP53*-altered cell lines are more sensitive towards MLN8237 than *TP53* wildtype cells, cell viability analysis revealed that in contrast to the treatment with AURKA-ligands, MLN8237 could not inhibit cell growth of the *TP53*-altered human HCC cell lines close to 100%. An explanation for this could be the induction of senescence, which is a known, cell line-dependent outcome of MLN8237 treatment[180], but this needs further confirmation.
Using genetically-defined murine HCC cell lines being deficient for *Trp53*, *Cdkn2a*^{Arf} or both, I could prove that sensitivity towards the AURKA-ligands is mediated by *Trp53*-deficiency. *Trp53* wildtype HCC cells, instead, are resistant towards these small molecules. This is surprising, as my data imply, that upon treatment also *Trp53* wildtype cells showed a stabilized AURKA/TPX2 complex, activated AURKA and PLK1, disturbed spindle formation and M phase arrested cells. However, I could barely detect mitotic catastrophe and only an early induction of apoptosis but not at later time points. In contrast to *Trp53*-deficient cells, the initial induction of cleaved caspase 3 was not accompanied by MCL1 degradation, arguing against mitotic catastrophe. In line with this, although cyclin B levels were increased at those time points, suggesting an M phase arrest, it cannot be excluded that a few cells already exit mitosis and entered G1 phase probably without proper cytokinesis. Since p53 is functional, it is possible that those few cells undergo apoptosis due to p21-dependent activation of the G1 checkpoint. To test this, co-immunofluorescence staining of cleaved caspase 3 and cyclin B (marker for M phase) or CDT1 (marker for G1 phase)[181] could be performed to determine in which cell cycle phase cells are upon apoptosis induction. Alternatively, cells could be stained with antibodies against those proteins and be analyzed by flow cytometry. Co-immunofluorescence staining of cleaved caspase 3 and p21, as well as

a CRISPR-mediated knockout or shRNA-induced knockdown of *Cdkn1a* (p21) prior to treatment will help to answer the question if cell death is dependent on p21.

Interestingly, most *Trp53* wildtype cells are able to overcome the initial formation of abnormal spindles over time and continue cycling with a normal DNA content. This is surprising, because it is known that in *Trp53* wildtype cells spindle poisons like nocodazole or colcemid can lead to mitotic slippage, however, the irregular DNA content leads to the activation of the G1 checkpoint in order to prevent DNA re-replication and ensure chromosomal integrity[39]. Thereby, p21 is upregulated in a p53-dependent manner and inhibits the cyclinD-CDK4 and cyclinE-CDK2 complexes[32, 40]. This prevents the hyperphosphorylation and release of RB1 from the E2F transcription factor, which in turn inhibits the expression of S phase promoting genes[32, 182]. As a result, cells either arrest in a “pseudo G1”-state with double the DNA content, become senescent or undergo apoptosis[182]. However, I did not observe a continuous G2/M or a “pseudo G1” phase arrest in cell cycle and western blot analysis and only marginally detected cell death. One explanation would be that upon mitotic slippage cells with doubled DNA content are able to divide in G1 phase. Choudhary *et al.* showed that cells, after failed cytokinesis, are able to return to a diploid state by dividing their two nuclei into two daughter cells in interphase without the cytokinesis machinery in order to preserve genomic integrity, a process called cytofission[183]. However, as they only observed it in up to 2% of the cells per day, it seems unlikely that this is the cause for normal cell cycling upon treatment with AURKA-ligands. A second explanation could be that *Trp53* wildtype cells are able to repair the spindle defects before exiting mitosis. I reasoned that a possibility for this could be that the AURKA/TPX2 complex is less stable in *Trp53* wildtype cells upon treatment and gets disrupted earlier than in *Trp53*-deficient cells, therefore allowing the spindles to form normally before mitotic slippage can occur. However, my data show that the AURKA/TPX2 complex has the same stability in both genetic backgrounds, excluding this option. Another possibility is that p53 directly affects mitosis, although it was shown that p53 plays no role in mitotic checkpoint functions upon treatment with nocodazole[39]. However, p53 has an indirect function in mitosis, comprising the transcriptional repression of Mad2 via p21 induction and canonical Rb pathway signaling[57]. This might suggest, that *RB1* mutations further increase sensitivity to the AURKA-ligands.

To prove that theory I tested a cohort of different human SCLC and NSCLC cancer cell lines. Since *TP53* is mutated in 50% of NSCLC and up to 90% in SCLC and *RB1* in

20% of NSCLC and 90% of SCLC these cancer types are another suitable target for the AURKA-ligands[51, 184, 185]. This is interesting, because SCLCs, which comprise 15% of lung cancers, have an exceptionally poor prognosis[185, 186]. Although those tumors respond initially to chemotherapies, they quickly recur and are resistant to further treatments and better therapy options are urgently needed[187]. I found that in lung cancer a *TP53* mutation alone is not a robust marker for their response. However, the three highly responding cell lines also possessed an additional *RB1* mutation, which was not the case for the remaining cell lines. This is in line with the results from Gong et al., showing that SCLC with loss of the tumor suppressor *RB1* are hypersensitive towards AURKA inhibition[109]. A second paper, building on the observation that *RB1* loss is synergistic with AURKA inhibition, unraveled the underlying mechanism. It was shown that *RB1* loss leads to an E2F-dependent upregulation of stathmin, which in turn induces the destabilization of the spindle microtubules and activation of the SAC. Additional AURKA inhibition prevents the phosphorylation of stathmin by AURKA, thereby increasing its activation. This leads to an even stronger disturbance of the spindle microtubule dynamics, resulting SAC hyperactivation and mitotic cell death[122]. Furthermore, it was shown that p53 transcriptionally suppresses stathmin[188].
Thus, although the AURKA-ligands do not inhibit the catalytic function of AURKA, it is conceivable that due to the SAC activation, stathmin could also be the mediator for the sensitivity of *TP53* and *RB1* double mutated lung cancer cells or even *TP53* mutated liver cancer cells. To test this theory, it could be determined if a CRISPR-mediated knockout of *STMN1* (stathmin) in those cells abolishes the efficacy of the AURKA-ligands. Accordingly, since a low abundance and phosphorylation of stathmin lowers the SAC induction, it could be tested if the overexpression of non-phosphorylatable, constitutively active stathmin[189] in *TP53* single mutated or *TP53* wildtype cancer cells sensitizes cells towards AURKA-ligands.

However, those results also highlight the fact, that additional mutations to *TP53* might be essential for treatment response.
Former data from our laboratory using MLN8237 suggested, that overexpression of the oncogene MYC is a susceptibility towards combined AURKA conformation and kinase alteration. Similar to MLN8237 and CD532[70, 110, 111], the AURKA-ligands disrupt the AURKA/MYC complex and lead to MYC degradation. Although we lack a crystal structure for the AURKA/compound complex, molecular modeling performed by Dr.

Tatu Pantsar (data not shown) suggests that the AURKA-ligands most likely act via a structural change of AURKA. However, the present study provides evidence that the change in MYC stability is not solely responsible for the observed phenotype, since LN3350 and LN3352 also induce growth inhibition in stable MYC^{T58A} expressing cells, which is comparable to degradable MYC^{WT}-expressing cells. This is contrary to MLN8237, since it was shown that murine HCC tumors overexpressing the MYC^{T58A} mutant are resistant to MLN8237 treatment[70]. An explanation could be that the shift induced by the AURKA-ligands is different to that of MLN8237 and thereby also affects other interaction partners of AURKA, like TPX2, that are not affected by MLN8237. To prove that theory, crystal structures of the AURKA complex are needed. However, it has to be noted that MLN8237 has only been tested *in vivo* and the AURKA-ligands only *in vitro* on MYC^{T58A} tumor cells and that also this could be a reason for the observed difference.

These data suggest the need for the development of other robust biomarker that allows to stratify different tumor samples into AURKA-ligand responders and non-responders. However, those biomarkers might vary between different tumor entities. By screening a set of 29 breast cancer cell lines, for example, it was shown that the Aurora kinase and FLT3 inhibitor ENMD-2076 has a stronger inhibitory effect on triple negative breast cancer (TNBC) cells, deficient for the estrogen receptor, progesterone receptor and without *HER2* amplification, compared to the other subtypes[190]. Amongst TNBC cells, the most sensitive were *TP53*-mutated cell lines with increased p53-expression, whereas the cell lines having mutated but decreased p53 rather acquire a senescent phenotype[190]. The authors hypothesize, that p53-binding sites in promotors of pro-apoptotic genes have a lower affinity than those of growth arrest inducing genes and that high levels of p53 are needed for binding and apoptosis induction. It is also possible, that *TP53* mutants acquired neomorphic functions, like the ability to inhibit p63 and p73 functions, two other factors of the p53 family[55, 191]. P73 can partially regulate p53 target genes in *TP53*-deficient cells and is often overexpressed in breast cancer[192, 193]. Additionally, it was found that in oral squamous carcinoma and hepatic carcinomas, *TP53* with gain-of-function mutations, but not wildtype *TP53*, can induce stathmin expression[194, 195]. Therefore, it would be worth it to analyze if TNBC cell lines with mutated and overexpressed p53 are sensitive towards AURKA-ligands as well.

Besides identification of reliable biomarker, putative side effects of the AURKA-ligands are important for a transfer as a targeted therapy into the clinic. One reason for side effects of drug treatments are off-targets of the compounds. By performing a kinome screen consisting of 320 wildtype kinases, we did not identify any off-targets for LN3350 and only 6 kinases, including AURKA, for LN3352 that were inhibited more than 50% at the high concentration of 500 nM. If we take into consideration that this assay is also performed on isolated enzymes and the cellular IC_{50} of LN3352 is with around 60 nM more than 8 time lower, we can reason, that those off-targets play no role in the cellular setup. Further evidence for the lack of off-targets and side effects are supported by the specific cell growth inhibition of tumor cell lines compared to immortalized, non-tumorigenic cell lines. My data imply, that the AURKA-ligands LN3350 and LN3352 might possess an improved therapeutic index compared to MLN8237. This would be an important aspect for a potential clinical translation of the AURKA-ligands, since it suggests, that in contrast to MLN8237, a more continuous treatment could be feasible. My data suggest, that several rounds of mitoses are necessary to accumulate damage and induce apoptosis in a substantial number of cells. Additionally, tumor cells are not synchronized and therefore reach M phase at different time points, showing the need for a continuous treatment with M phase disturbing compounds. One estimation to calculate the pattern of M phases is the tumor volume doubling time (TVDT) which was determined for HCC in several studies, showing a correlation with the initial tumor diameter[196-198]. In 2021, Nathani et al. published a systemic review and meta-analysis of 20 studies including 1374 HCC lesions in 1334 patients[199]. The pooled median TVDT was 4.6 months, with the individual studies ranging from a median TVDT of 2.2 to 11.3 months. MLN8237, however, can only be given 7 days in a 21-day cycle due to the adverse events it causes. This implies, that not all mitotic tumor cells can be targeted, likely leading to tumor progression. Thus, a continuous treatment scheme of the AURKA-ligands could be an advantage.

However, it is difficult to correlate results from *in vitro* toxicity studies with actual *in vivo* responses. The most observed 3-4 grade adverse effects of MLN8237 in clinical trials, for example, affect hematopoiesis and comprise (febrile) neutropenia, leukopenia, thrombocytopenia, with the affected cell types not being present in simple *in vitro* experiments. A higher predictive power for the risk for clinical myelosuppression might be achieved by challenging *in vitro* grown human bone marrow or umbilical cord blood

derived granulocyte-macrophages (CFU-GM, colony forming unit granulocyte-macrophages) with those compounds[109, 200, 201]. Making use of this CFU-GM assay, a predictive model was established for estimating the human maximum tolerated dose (MTD). It was shown that with this model out of 23 antineoplastic and antiviral drugs, pesticides and drugs for other therapeutic indications, the human MTD of 20 drugs was predicted correctly based on the calculated actual IC_{90} or the extrapolated IC_{90}[200, 201]. Therefore, an additional comparison of the AURKA-ligands with MLN8237 using tumor cells and a CFU-GM assay could give a more precise picture of the different therapeutic indices.

The best possible way to preclinically determine effectiveness and tolerability, however, are *in vivo* studies. Pharmacokinetic studies in mice showed an insufficient bioavailability of LN3350 and LN3352 (data not shown). This suggests, that the small molecules do not get absorbed in the stomach upon oral delivery. Furthermore, plasma concentrations of both compounds after intravenous injection imply, that they are metabolically instable. We could identify the metabolites of LN3350 and LN3352, which are the cleavage products of the amide bond that both compounds contain (data not shown). Therefore, it is likely that they get cleaved by amidases, independently of cytochrome P450 enzymes, which catalyze the oxidative biotransformation of 70-80% of all clinical drugs[202]. After having tested the identified metabolites *in vitro*, we can exclude that they are biologically active (data not shown). However, several attempts of bioisosteric replacements are currently in progress to improve the metabolic stability of the AURKA-ligands.

Additionally, an alternative to improve the bioavailability and possibly prevent cleavage of LN3350 and LN3352 by amidases upon intravenous application is their encapsulation with albumin-nanoparticles. This strategy was already used for paclitaxel (nAb paclitaxel or abraxane), to reduce the toxicity associated with Cremophor EL, an ingredient of the formulation[203], and increase the intratumoral concentration of the active drug. In line with this, several clinical studies for (metastatic) breast cancer found that nAb paclitaxel is superior compared to conventional paclitaxel, with regard to overall response rate, time to tumor progression and toxicity[203-207].

Since albumin is an essential carrier of biomolecules through endothelial cells, mainly via receptor-mediated transcytosis, an additional advantage of this formulation are the albumin transport routes that would efficiently traffic the compounds to the tumor[208-211]. Therefore, albumin encapsulation represents a good chance to increase the bioavailability of LN3350 and LN3352, by forming micelles that shield the compounds from cleavage by amidases and might allow a more efficient transport to the tumor. In cooperation with Prof. Dr. Rolf Daniels, we already generated albumin nanoparticle-bound LN3350 and LN3352. First results from pharmacokinetic studies, conducted by Pharmacelsus, revealed intriguing improvements compared to LN3350 and LN3352 without albumin-formulation (data not shown). The next step will be to test the efficacy of the albumin-encapsulated LN3350 and LN3352 *in vivo*. We formerly established highly tractable mosaic HCC mouse models by taking advantage of direct and stable intrahepatic gene transfer via hydrodynamic tail vein injection of transposon vectors[47, 70, 212-214]. Importantly, these tumors mimic histology and pathology as well as therapy resistance of human HCCs, representing an ideal model for testing the novel AURKA-ligands[212].

In conclusion, this work generated promising results for a novel AURKA-ligand based therapy option for the treatment of *TP53*-altered HCC and possibly other tumor entities like *TP53* and *RB1* double mutated SCLC.

5 Acknowledgement

First of all, I would like to thank my supervisor Lars Zender for the great opportunity to perform this study in his lab, for his scientific guidance and input.

Further, I am grateful to Stefan Laufer for the fruitful collaboration and for being a referent for my PhD thesis.

This project would not have been possible without my beloved “Team Aurora”: Dirk Flötgen, Juliander Reiner, Tatu Pantsar and Benedikt Wagner. Working with you not only made me grow scientifically, but also was always a pleasure. Our “Knaipi”-evenings and other non-lab-related activities just made us become an even better team.

I want to thank especially my former colleague Marco Seehawer, who not only is a great friend, but was always a reliable pillar with regard to scientific input and discussion. I really appreciate the effort you put in proof-reading my thesis and giving me valuable feedback.

I would like to thank Daniel Dauch and Ramona Rudalska for their previous work leading to this project, the generation of the murine cell lines and the scientific discussion.

The extraordinary management, effort and support of Elke Rist, the good soul of the lab, deserve my highest appreciation and gratitude. Thank you so much for all your time, motivation and help!

A huge thank you belongs to Pearl Schiemann, who, together with Elke Rist, keeps the lab and the mouse husbandry running. I also want to thank Lea Herrmann and Aylin Heinrich for general lab organization and spreading good mood. Many thanks also to Tae-Won Kang for his support with regulations and administrative procedures. This was supported by the secretary team, Eva Enzinger, Gisela Wälder, Jasmin Sander, Tanja Loch, Inês Paixão and Susann Walter

I am thankful to Thales Kronenberger for helping with the bioinformatical analysis and Katharina Bauer for performing the ADP-Glo™ assay.

I want to thank our cooperation partners Stefan Knapp and Martin Schröder for conducting the TSA assays, as well as Rolf Daniels for performing the albumin encapsulation.

Further, I would like to thank Sabrina Klotz, Jule Harbig, Athina Moschopoulou, Luana D'Artista, Clemens Hinterleitner, Stefan Zwirner and Stella Asmanidou for all their help and scientific discussions. I am very grateful for your friendship, which made work so much easier. In general, the whole Zender lab deserves a big thank you for providing great working conditions and a great atmosphere also outside the lab.

I am really appreciative to Luana D'Artista and Dirk Flötgen for proof-reading my thesis.

A big thanks to all my friends, especially Michael Kaleja, Christian Wenzel, Tim Fennel, Lisa Mergelmeyer, Wadim Furs and Dirk Ehmann-Harbig, who supported me throughout the years and cheered me up in difficult times.

And finally, I want to thank my parents with all of my heart for their never-ending, unconditional support and understanding. Thank you so much that I can always count on you!

6 References

1. Llovet, J.M. *et al.* Hepatocellular carcinoma. *Nature Reviews Disease Primers* **7**, 6 (2021).
2. Villanueva, A. Hepatocellular Carcinoma. *N Engl J Med* **380**, 1450-1462 (2019).
3. Farazi, P.A. & DePinho, R.A. Hepatocellular carcinoma pathogenesis: from genes to environment. *Nat Rev Cancer* **6**, 674-687 (2006).
4. Schulz, P.O. *et al.* Association of nonalcoholic fatty liver disease and liver cancer. *World J Gastroenterol* **21**, 913-918 (2015).
5. Global Burden of Disease Liver Cancer, C. *et al.* The Burden of Primary Liver Cancer and Underlying Etiologies From 1990 to 2015 at the Global, Regional, and National Level: Results From the Global Burden of Disease Study 2015. *JAMA Oncol* **3**, 1683-1691 (2017).
6. Yuen, M.F. *et al.* Hepatitis B virus infection. *Nat Rev Dis Primers* **4**, 18035 (2018).
7. Estes, C., Razavi, H., Loomba, R., Younossi, Z. & Sanyal, A.J. Modeling the epidemic of nonalcoholic fatty liver disease demonstrates an exponential increase in burden of disease. *Hepatology* **67**, 123-133 (2018).
8. McGlynn, K.A., Petrick, J.L. & London, W.T. Global epidemiology of hepatocellular carcinoma: an emphasis on demographic and regional variability. *Clin Liver Dis* **19**, 223-238 (2015).
9. Younossi, Z. *et al.* Nonalcoholic Steatohepatitis Is the Fastest Growing Cause of Hepatocellular Carcinoma in Liver Transplant Candidates. *Clin Gastroenterol Hepatol* **17**, 748-755.e743 (2019).
10. Zeuzem, S. Decade in review-HCV: hepatitis C therapy-a fast and competitive race. *Nat Rev Gastroenterol Hepatol* **11**, 644-645 (2014).
11. Livraghi, T., Mäkisalo, H. & Line, P.D. Treatment options in hepatocellular carcinoma today. *Scand J Surg* **100**, 22-29 (2011).
12. Chua, C.W. & Choo, S.P. Targeted therapy in hepatocellular carcinoma. *Int J Hepatol* **2011**, 348297 (2011).
13. Llovet, J.M., Schwartz, M. & Mazzaferro, V. Resection and liver transplantation for hepatocellular carcinoma. *Semin Liver Dis* **25**, 181-200 (2005).
14. EASL-EORTC clinical practice guidelines: management of hepatocellular carcinoma. *J Hepatol* **56**, 908-943 (2012).
15. Lachenmayer, A., Alsinet, C., Chang, C.Y. & Llovet, J.M. Molecular approaches to treatment of hepatocellular carcinoma. *Dig Liver Dis* **42 Suppl 3**, S264-272 (2010).
16. Llovet, J.M. *et al.* Sorafenib in Advanced Hepatocellular Carcinoma. *New England Journal of Medicine* **359**, 378-390 (2008).
17. Kudo, M. *et al.* Lenvatinib versus sorafenib in first-line treatment of patients with unresectable hepatocellular carcinoma: a randomised phase 3 non-inferiority trial. *Lancet* **391**, 1163-1173 (2018).

18. Finn, R.S. *et al.* Atezolizumab plus Bevacizumab in Unresectable Hepatocellular Carcinoma. *New England Journal of Medicine* **382**, 1894-1905 (2020).
19. Bruix, J. *et al.* Regorafenib for patients with hepatocellular carcinoma who progressed on sorafenib treatment (RESORCE): a randomised, double-blind, placebo-controlled, phase 3 trial. *Lancet* **389**, 56-66 (2017).
20. Abou-Alfa, G.K. *et al.* Cabozantinib in Patients with Advanced and Progressing Hepatocellular Carcinoma. *New England Journal of Medicine* **379**, 54-63 (2018).
21. Zhu, A.X. *et al.* Ramucirumab after sorafenib in patients with advanced hepatocellular carcinoma and increased α-fetoprotein concentrations (REACH-2): a randomised, double-blind, placebo-controlled, phase 3 trial. *Lancet Oncol* **20**, 282-296 (2019).
22. El-Khoueiry, A.B. *et al.* Nivolumab in patients with advanced hepatocellular carcinoma (CheckMate 040): an open-label, non-comparative, phase 1/2 dose escalation and expansion trial. *Lancet* **389**, 2492-2502 (2017).
23. Zucman-Rossi, J., Villanueva, A., Nault, J.C. & Llovet, J.M. Genetic Landscape and Biomarkers of Hepatocellular Carcinoma. *Gastroenterology* **149**, 1226-1239.e1224 (2015).
24. Jeng, Y.M., Peng, S.Y., Lin, C.Y. & Hsu, H.C. Overexpression and amplification of Aurora-A in hepatocellular carcinoma. *Clin Cancer Res* **10**, 2065-2071 (2004).
25. Haupt, Y., Maya, R., Kazaz, A. & Oren, M. Mdm2 promotes the rapid degradation of p53. *Nature* **387**, 296-299 (1997).
26. Kubbutat, M.H.G., Jones, S.N. & Vousden, K.H. Regulation of p53 stability by Mdm2. *Nature* **387**, 299-303 (1997).
27. Honda, R., Tanaka, H. & Yasuda, H. Oncoprotein MDM2 is a ubiquitin ligase E3 for tumor suppressor p53. *FEBS Lett* **420**, 25-27 (1997).
28. Vousden, K.H. & Prives, C. Blinded by the Light: The Growing Complexity of p53. *Cell* **137**, 413-431 (2009).
29. Shieh, S.Y., Ikeda, M., Taya, Y. & Prives, C. DNA damage-induced phosphorylation of p53 alleviates inhibition by MDM2. *Cell* **91**, 325-334 (1997).
30. Williams, A.B. & Schumacher, B. p53 in the DNA-Damage-Repair Process. *Cold Spring Harb Perspect Med* **6**, a026070 (2016).
31. Kastan, M.B., Onyekwere, O., Sidransky, D., Vogelstein, B. & Craig, R.W. Participation of p53 Protein in the Cellular Response to DNA Damage. *Cancer Research* **51**, 6304-6311 (1991).
32. Harper, J.W., Adami, G.R., Wei, N., Keyomarsi, K. & Elledge, S.J. The p21 Cdk-interacting protein Cip1 is a potent inhibitor of G1 cyclin-dependent kinases. *Cell* **75**, 805-816 (1993).
33. Serrano, M., Lin, A.W., McCurrach, M.E., Beach, D. & Lowe, S.W. Oncogenic ras Provokes Premature Cell Senescence Associated with Accumulation of p53 and p16INK4a. *Cell* **88**, 593-602 (1997).

34. Shay, J.W., Pereira-Smith, O.M. & Wright, W.E. A role for both RB and p53 in the regulation of human cellular senescence. *Exp Cell Res* **196**, 33-39 (1991).
35. Clarke, A.R. *et al.* Thymocyte apoptosis induced by p53-dependent and independent pathways. *Nature* **362**, 849-852 (1993).
36. Lowe, S.W., Schmitt, E.M., Smith, S.W., Osborne, B.A. & Jacks, T. p53 is required for radiation-induced apoptosis in mouse thymocytes. *Nature* **362**, 847-849 (1993).
37. Villunger, A. *et al.* p53- and Drug-Induced Apoptotic Responses Mediated by BH3-Only Proteins Puma and Noxa. *Science* **302**, 1036-1038 (2003).
38. Miyashita, T. *et al.* Tumor suppressor p53 is a regulator of bcl-2 and bax gene expression in vitro and in vivo. *Oncogene* **9**, 1799-1805 (1994).
39. Lanni, J.S. & Jacks, T. Characterization of the p53-dependent postmitotic checkpoint following spindle disruption. *Mol Cell Biol* **18**, 1055-1064 (1998).
40. el-Deiry, W.S. *et al.* WAF1, a potential mediator of p53 tumor suppression. *Cell* **75**, 817-825 (1993).
41. Niculescu, A.B., 3rd *et al.* Effects of p21(Cip1/Waf1) at both the G1/S and the G2/M cell cycle transitions: pRb is a critical determinant in blocking DNA replication and in preventing endoreduplication. *Mol Cell Biol* **18**, 629-643 (1998).
42. Beauséjour, C.M. *et al.* Reversal of human cellular senescence: roles of the p53 and p16 pathways. *The EMBO Journal* **22**, 4212-4222 (2003).
43. Lee, S. & Schmitt, C.A. The dynamic nature of senescence in cancer. *Nature Cell Biology* **21**, 94-101 (2019).
44. Milanovic, M. *et al.* Senescence-associated reprogramming promotes cancer stemness. *Nature* **553**, 96-100 (2018).
45. Campisi, J. Senescent cells, tumor suppression, and organismal aging: good citizens, bad neighbors. *Cell* **120**, 513-522 (2005).
46. Shay, J.W., Pereira-Smith, O.M. & Wright, W.E. A role for both RB and p53 in the regulation of human cellular senescence. *Experimental Cell Research* **196**, 33-39 (1991).
47. Kang, T.-W. *et al.* Senescence surveillance of pre-malignant hepatocytes limits liver cancer development. *Nature* **479**, 547-551 (2011).
48. Kastenhuber, E.R. & Lowe, S.W. Putting p53 in Context. *Cell* **170**, 1062-1078 (2017).
49. Aubrey, B.J., Kelly, G.L., Janic, A., Herold, M.J. & Strasser, A. How does p53 induce apoptosis and how does this relate to p53-mediated tumour suppression? *Cell Death & Differentiation* **25**, 104-113 (2018).
50. Kandoth, C. *et al.* Mutational landscape and significance across 12 major cancer types. *Nature* **502**, 333-339 (2013).
51. Minna, J.D., Roth, J.A. & Gazdar, A.F. Focus on lung cancer. *Cancer Cell* **1**, 49-52 (2002).
52. Bykov, V.J.N., Eriksson, S.E., Bianchi, J. & Wiman, K.G. Targeting mutant p53 for efficient cancer therapy. *Nat Rev Cancer* **18**, 89-102 (2018).

53. Soussi, T. & Wiman, K.G. TP53: an oncogene in disguise. *Cell Death Differ* **22**, 1239-1249 (2015).
54. Muller, P.A.J. *et al.* Mutant p53 enhances MET trafficking and signalling to drive cell scattering and invasion. *Oncogene* **32**, 1252-1265 (2013).
55. Weissmueller, S. *et al.* Mutant p53 drives pancreatic cancer metastasis through cell-autonomous PDGF receptor β signaling. *Cell* **157**, 382-394 (2014).
56. Shirole, N.H. *et al.* TP53 exon-6 truncating mutations produce separation of function isoforms with pro-tumorigenic functions. *eLife* **5**, e17929 (2016).
57. Schvartzman, J.M., Duijf, P.H., Sotillo, R., Coker, C. & Benezra, R. Mad2 is a critical mediator of the chromosome instability observed upon Rb and p53 pathway inhibition. *Cancer Cell* **19**, 701-714 (2011).
58. Martins, C.P., Brown-Swigart, L. & Evan, G.I. Modeling the therapeutic efficacy of p53 restoration in tumors. *Cell* **127**, 1323-1334 (2006).
59. Ventura, A. *et al.* Restoration of p53 function leads to tumour regression in vivo. *Nature* **445**, 661-665 (2007).
60. Xue, W. *et al.* Senescence and tumour clearance is triggered by p53 restoration in murine liver carcinomas. *Nature* **445**, 656-660 (2007).
61. Brosh, R. & Rotter, V. When mutants gain new powers: news from the mutant p53 field. *Nat Rev Cancer* **9**, 701-713 (2009).
62. Terzian, T. *et al.* The inherent instability of mutant p53 is alleviated by Mdm2 or p16INK4a loss. *Genes & development* **22**, 1337-1344 (2008).
63. Lehmann, S. *et al.* Targeting p53 in vivo: a first-in-human study with p53-targeting compound APR-246 in refractory hematologic malignancies and prostate cancer. *J Clin Oncol* **30**, 3633-3639 (2012).
64. Deneberg, S. *et al.* An open-label phase I dose-finding study of APR-246 in hematological malignancies. *Blood Cancer J* **6**, e447-e447 (2016).
65. Lindemann, A. *et al.* COTI-2, A Novel Thiosemicarbazone Derivative, Exhibits Antitumor Activity in HNSCC through p53-dependent and -independent Mechanisms. *Clin Cancer Res* **25**, 5650-5662 (2019).
66. Heffeter, P. *et al.* Anticancer Thiosemicarbazones: Chemical Properties, Interaction with Iron Metabolism, and Resistance Development. *Antioxid Redox Signal* **30**, 1062-1082 (2019).
67. Chasov, V. *et al.* Key Players in the Mutant p53 Team: Small Molecules, Gene Editing, Immunotherapy. *Frontiers in Oncology* **10** (2020).
68. Lambert, J.M.R. *et al.* PRIMA-1 Reactivates Mutant p53 by Covalent Binding to the Core Domain. *Cancer Cell* **15**, 376-388 (2009).
69. Tessoulin, B. *et al.* PRIMA-1Met induces myeloma cell death independent of p53 by impairing the GSH/ROS balance. *Blood* **124**, 1626-1636 (2014).
70. Dauch, D. *et al.* A MYC-aurora kinase A protein complex represents an actionable drug target in p53-altered liver cancer. *Nat Med* **22**, 744-753 (2016).
71. Willems, E. *et al.* The functional diversity of Aurora kinases: a comprehensive review. *Cell Div* **13**, 7-7 (2018).

72. Nikonova, A.S., Astsaturov, I., Serebriiskii, I.G., Dunbrack, R.L. & Golemis, E.A. Aurora A kinase (AURKA) in normal and pathological cell division. *Cell Mol Life Sci* **70**, 661-687 (2013).
73. Lindqvist, A., Rodríguez-Bravo, V. & Medema, R.H. The decision to enter mitosis: feedback and redundancy in the mitotic entry network. *J Cell Biol* **185**, 193-202 (2009).
74. Joukov, V. & De Nicolo, A. Aurora-PLK1 cascades as key signaling modules in the regulation of mitosis. *Science Signaling* **11**, eaar4195 (2018).
75. Macůrek, L. *et al.* Polo-like kinase-1 is activated by aurora A to promote checkpoint recovery. *Nature* **455**, 119-123 (2008).
76. Seki, A., Coppinger, J.A., Jang, C.-Y., Yates, J.R. & Fang, G. Bora and the kinase Aurora a cooperatively activate the kinase Plk1 and control mitotic entry. *Science* **320**, 1655-1658 (2008).
77. Chan, E.H.Y., Santamaria, A., Silljé, H.H.W. & Nigg, E.A. Plk1 regulates mitotic Aurora A function through betaTrCP-dependent degradation of hBora. *Chromosoma* **117**, 457-469 (2008).
78. Seki, A. *et al.* Plk1- and beta-TrCP-dependent degradation of Bora controls mitotic progression. *J Cell Biol* **181**, 65-78 (2008).
79. Joukov, V., Walter, J.C. & De Nicolo, A. The Cep192-organized aurora A-Plk1 cascade is essential for centrosome cycle and bipolar spindle assembly. *Mol Cell* **55**, 578-591 (2014).
80. Joukov, V., De Nicolo, A., Rodriguez, A., Walter, J.C. & Livingston, D.M. Centrosomal protein of 192 kDa (Cep192) promotes centrosome-driven spindle assembly by engaging in organelle-specific Aurora A activation. *Proc Natl Acad Sci U S A* **107**, 21022-21027 (2010).
81. Nigg, E.A. & Raff, J.W. Centrioles, Centrosomes, and Cilia in Health and Disease. *Cell* **139**, 663-678 (2009).
82. Bettencourt-Dias, M. & Glover, D.M. Centrosome biogenesis and function: centrosomics brings new understanding. *Nature Reviews Molecular Cell Biology* **8**, 451-463 (2007).
83. Meng, L. *et al.* Bimodal Interaction of Mammalian Polo-Like Kinase 1 and a Centrosomal Scaffold, Cep192, in the Regulation of Bipolar Spindle Formation. *Molecular and Cellular Biology* **35**, 2626-2640 (2015).
84. Kufer, T.A. *et al.* Human TPX2 is required for targeting Aurora-A kinase to the spindle. *J Cell Biol* **158**, 617-623 (2002).
85. Bayliss, R., Sardon, T., Vernos, I. & Conti, E. Structural basis of Aurora-A activation by TPX2 at the mitotic spindle. *Mol Cell* **12**, 851-862 (2003).
86. Groen, A.C. *et al.* XRHAMM functions in ran-dependent microtubule nucleation and pole formation during anastral spindle assembly. *Curr Biol* **14**, 1801-1811 (2004).
87. Scrofani, J., Sardon, T., Meunier, S. & Vernos, I. Microtubule Nucleation in Mitosis by a RanGTP-Dependent Protein Complex. *Current Biology* **25**, 131-140 (2015).

88. Pinyol, R., Scrofani, J. & Vernos, I. The role of NEDD1 phosphorylation by Aurora A in chromosomal microtubule nucleation and spindle function. *Curr Biol* **23**, 143-149 (2013).
89. Petry, S., Groen, Aaron C., Ishihara, K., Mitchison, Timothy J. & Vale, Ronald D. Branching Microtubule Nucleation in Xenopus Egg Extracts Mediated by Augmin and TPX2. *Cell* **152**, 768-777 (2013).
90. Du, R., Huang, C., Liu, K., Li, X. & Dong, Z. Targeting AURKA in Cancer: molecular mechanisms and opportunities for Cancer therapy. *Mol Cancer* **20**, 15-15 (2021).
91. Marumoto, T., Zhang, D. & Saya, H. Aurora-A — A guardian of poles. *Nature Reviews Cancer* **5**, 42-50 (2005).
92. Zhang, M.-Y. *et al.* Elevated mRNA Levels of AURKA, CDC20 and TPX2 are associated with poor prognosis of smoking related lung adenocarcinoma using bioinformatics analysis. *International Journal of Medical Sciences* **15**, 1676-1685 (2018).
93. Schneider, M.A. *et al.* AURKA, DLGAP5, TPX2, KIF11 and CKAP5: Five specific mitosis-associated genes correlate with poor prognosis for non-small cell lung cancer patients. *Int J Oncol* **50**, 365-372 (2017).
94. Guo, M. *et al.* Increased AURKA promotes cell proliferation and predicts poor prognosis in bladder cancer. *BMC Syst Biol* **12**, 118-118 (2018).
95. Xie, Y. *et al.* Inhibition of Aurora Kinase A Induces Necroptosis in Pancreatic Carcinoma. *Gastroenterology* **153**, 1429-1443.e1425 (2017).
96. Marumoto, T. *et al.* Roles of aurora-A kinase in mitotic entry and G2 checkpoint in mammalian cells. *Genes to cells : devoted to molecular & cellular mechanisms* **7**, 1173-1182 (2002).
97. Anand, S., Penrhyn-Lowe, S. & Venkitaraman, A.R. AURORA-A amplification overrides the mitotic spindle assembly checkpoint, inducing resistance to Taxol. *Cancer Cell* **3**, 51-62 (2003).
98. Jiang, Y., Zhang, Y., Lees, E. & Seghezzi, W. AuroraA overexpression overrides the mitotic spindle checkpoint triggered by nocodazole, a microtubule destabilizer. *Oncogene* **22**, 8293-8301 (2003).
99. Meraldi, P., Honda, R. & Nigg, E.A. Aurora-A overexpression reveals tetraploidization as a major route to centrosome amplification in p53-/- cells. *Embo j* **21**, 483-492 (2002).
100. Otto, T. *et al.* Stabilization of N-Myc is a critical function of Aurora A in human neuroblastoma. *Cancer Cell* **15**, 67-78 (2009).
101. Lin, X. *et al.* The role of Aurora-A in human cancers and future therapeutics. *Am J Cancer Res* **10**, 2705-2729 (2020).
102. Melichar, B. *et al.* Safety and activity of alisertib, an investigational aurora kinase A inhibitor, in patients with breast cancer, small-cell lung cancer, non-small-cell lung cancer, head and neck squamous-cell carcinoma, and gastro-oesophageal adenocarcinoma: a five-arm phase 2 study. *Lancet Oncol* **16**, 395-405 (2015).

103. Beltran, H. *et al.* A Phase II Trial of the Aurora Kinase A Inhibitor Alisertib for Patients with Castration-resistant and Neuroendocrine Prostate Cancer: Efficacy and Biomarkers. *Clin Cancer Res* **25**, 43-51 (2019).
104. Barr, P.M. *et al.* Phase II Intergroup Trial of Alisertib in Relapsed and Refractory Peripheral T-Cell Lymphoma and Transformed Mycosis Fungoides: SWOG 1108. *J Clin Oncol* **33**, 2399-2404 (2015).
105. Dickson, M.A. *et al.* Phase II study of MLN8237 (Alisertib) in advanced/metastatic sarcoma. *Ann Oncol* **27**, 1855-1860 (2016).
106. Kelly, K.R. *et al.* Phase I study of MLN8237--investigational Aurora A kinase inhibitor--in relapsed/refractory multiple myeloma, non-Hodgkin lymphoma and chronic lymphocytic leukemia. *Invest New Drugs* **32**, 489-499 (2014).
107. Dees, E.C. *et al.* Phase I study of aurora A kinase inhibitor MLN8237 in advanced solid tumors: safety, pharmacokinetics, pharmacodynamics, and bioavailability of two oral formulations. *Clin Cancer Res* **18**, 4775-4784 (2012).
108. Müller, S., Chaikuad, A., Gray, N.S. & Knapp, S. The ins and outs of selective kinase inhibitor development. *Nature Chemical Biology* **11**, 818-821 (2015).
109. Gong, X. *et al.* Aurora A Kinase Inhibition Is Synthetic Lethal with Loss of the RB1 Tumor Suppressor Gene. *Cancer Discovery* **9**, 248-263 (2019).
110. Brockmann, M. *et al.* Small molecule inhibitors of aurora-a induce proteasomal degradation of N-myc in childhood neuroblastoma. *Cancer Cell* **24**, 75-89 (2013).
111. Gustafson, W.C. *et al.* Drugging MYCN through an allosteric transition in Aurora kinase A. *Cancer Cell* **26**, 414-427 (2014).
112. Fellmann, C. *et al.* An optimized microRNA backbone for effective single-copy RNAi. *Cell Rep* **5**, 1704-1713 (2013).
113. Schmitt, M. *et al.* Quantitative Proteomics Links the Intermediate Filament Nestin to Resistance to Targeted BRAF Inhibition in Melanoma Cells. *Molecular & cellular proteomics : MCP* **18**, 1096-1109 (2019).
114. Wentsch, H.K. *et al.* Optimized Target Residence Time: Type I1/2 Inhibitors for p38α MAP Kinase with Improved Binding Kinetics through Direct Interaction with the R-Spine. *Angew Chem Int Ed Engl* **56**, 5363-5367 (2017).
115. Walter, N.M. *et al.* Design, Synthesis, and Biological Evaluation of Novel Type I(1)/(2) p38α MAP Kinase Inhibitors with Excellent Selectivity, High Potency, and Prolonged Target Residence Time by Interfering with the R-Spine. *J Med Chem* **60**, 8027-8054 (2017).
116. Flötgen, D., Vol. unpublished doctoral (University of Tuebingen, Tuebingen, Germany, unpublished; 2020).
117. Fedorov, O., Niesen, F.H. & Knapp, S. Kinase inhibitor selectivity profiling using differential scanning fluorimetry. *Methods Mol Biol* **795**, 109-118 (2012).
118. Bahram, F., von der Lehr, N., Cetinkaya, C. & Larsson, L.-G. c-Myc hot spot mutations in lymphomas result in inefficient ubiquitination and decreased proteasome-mediated turnover. *Blood* **95**, 2104-2110 (2000).

119. Sears, R.C. The life cycle of C-myc: from synthesis to degradation. *Cell Cycle* **3**, 1133-1137 (2004).
120. Matson, D.R. & Stukenberg, P.T. Spindle poisons and cell fate: a tale of two pathways. *Mol Interv* **11**, 141-150 (2011).
121. Ianevski, A., Giri, A.K. & Aittokallio, T. SynergyFinder 2.0: visual analytics of multi-drug combination synergies. *Nucleic Acids Research* **48**, W488-W493 (2020).
122. Lyu, J. *et al.* Synthetic lethality of RB1 and aurora A is driven by stathmin-mediated disruption of microtubule dynamics. *Nat Commun* **11**, 5105-5105 (2020).
123. Cavazzoni, A. *et al.* Effect of inducible FHIT and p53 expression in the Calu-1 lung cancer cell line. *Cancer Letters* **246**, 69-81 (2007).
124. Sarasin, F.P., Giostra, E. & Hadengue, A. Cost-effectiveness of screening for detection of small hepatocellular carcinoma in western patients with Child-Pugh class A cirrhosis. *Am J Med* **101**, 422-434 (1996).
125. Screening for Hepatocellular Carcinoma in Chronic Liver Disease. *Annals of Internal Medicine* **161**, 261-269 (2014).
126. Singal, A.G., Lampertico, P. & Nahon, P. Epidemiology and surveillance for hepatocellular carcinoma: New trends. *J Hepatol* **72**, 250-261 (2020).
127. Asrani, S.K., Devarbhavi, H., Eaton, J. & Kamath, P.S. Burden of liver diseases in the world. *Journal of Hepatology* **70**, 151-171 (2019).
128. Tacke, F., Kroy, D.C., Barreiros, A.P. & Neumann, U.P. Liver transplantation in Germany. *Liver Transplantation* **22**, 1136-1142 (2016).
129. Nair, S., Verma, S. & Thuluvath, P.J. Obesity and its effect on survival in patients undergoing orthotopic liver transplantation in the United States. *Hepatology* **35**, 105-109 (2002).
130. Dolnikov, S., Adam, R., Cherqui, D. & Allard, M.A. Liver transplantation in elderly patients: what do we know at the beginning of 2020? *Surgery Today* **50**, 533-539 (2020).
131. Huang, A., Yang, X.-R., Chung, W.-Y., Dennison, A.R. & Zhou, J. Targeted therapy for hepatocellular carcinoma. *Signal Transduction and Targeted Therapy* **5**, 146 (2020).
132. Zhu, A.X. *et al.* SEARCH: a phase III, randomized, double-blind, placebo-controlled trial of sorafenib plus erlotinib in patients with advanced hepatocellular carcinoma. *J Clin Oncol* **33**, 559-566 (2015).
133. Cheng, A.L. *et al.* Sunitinib versus sorafenib in advanced hepatocellular cancer: results of a randomized phase III trial. *J Clin Oncol* **31**, 4067-4075 (2013).
134. Cainap, C. *et al.* Linifanib versus Sorafenib in patients with advanced hepatocellular carcinoma: results of a randomized phase III trial. *J Clin Oncol* **33**, 172-179 (2015).
135. Johnson, P.J. *et al.* Brivanib versus sorafenib as first-line therapy in patients with unresectable, advanced hepatocellular carcinoma: results from the randomized phase III BRISK-FL study. *J Clin Oncol* **31**, 3517-3524 (2013).

136. Zhu, A.X. *et al.* Effect of everolimus on survival in advanced hepatocellular carcinoma after failure of sorafenib: the EVOLVE-1 randomized clinical trial. *Jama* **312**, 57-67 (2014).
137. Rimassa, L. *et al.* Tivantinib for second-line treatment of MET-high, advanced hepatocellular carcinoma (METIV-HCC): a final analysis of a phase 3, randomised, placebo-controlled study. *Lancet Oncol* **19**, 682-693 (2018).
138. Pitsawong, W. *et al.* Dynamics of human protein kinase Aurora A linked to drug selectivity. *Elife* **7** (2018).
139. Gilburt, J.A.H. *et al.* Dynamic Equilibrium of the Aurora A Kinase Activation Loop Revealed by Single-Molecule Spectroscopy. *Angew Chem Int Ed Engl* **56**, 11409-11414 (2017).
140. Lake, E.W. *et al.* Quantitative conformational profiling of kinase inhibitors reveals origins of selectivity for Aurora kinase activation states. *Proc Natl Acad Sci U S A* **115**, E11894-e11903 (2018).
141. Douse, C.H., Vrielink, N., Wenlin, Z., Cota, E. & Tate, E.W. Targeting a dynamic protein-protein interaction: fragment screening against the malaria myosin A motor complex. *ChemMedChem* **10**, 134-143 (2015).
142. Gao, K., Oerlemans, R. & Groves, M.R. Theory and applications of differential scanning fluorimetry in early-stage drug discovery. *Biophys Rev* **12**, 85-104 (2020).
143. Norton, R.S., Leung, E.W., Chandrashekaran, I.R. & MacRaild, C.A. Applications of (19)F-NMR in Fragment-Based Drug Discovery. *Molecules* **21** (2016).
144. Birman, Y., Khorsand, S., Tu, E., Mortensen, R.B. & Butko, M.T. Second-harmonic generation-based methods to detect and characterize ligand-induced RNA conformational changes. *Methods* **167**, 92-104 (2019).
145. Richards, M.W. *et al.* Structural basis of N-Myc binding by Aurora-A and its destabilization by kinase inhibitors. *Proceedings of the National Academy of Sciences* **113**, 13726-13731 (2016).
146. Rossi, A.M. & Taylor, C.W. Analysis of protein-ligand interactions by fluorescence polarization. *Nature Protocols* **6**, 365-387 (2011).
147. Knight, Z.A. & Shokat, K.M. Features of Selective Kinase Inhibitors. *Chemistry & Biology* **12**, 621-637 (2005).
148. Yang, N.J. & Hinner, M.J. Getting across the cell membrane: an overview for small molecules, peptides, and proteins. *Methods in molecular biology (Clifton, N.J.)* **1266**, 29-53 (2015).
149. Liu, X., Testa, B. & Fahr, A. Lipophilicity and Its Relationship with Passive Drug Permeation. *Pharmaceutical Research* **28**, 962-977 (2011).
150. Giubettini, M. *et al.* Control of Aurora-A stability through interaction with TPX2. *J Cell Sci* **124**, 113-122 (2011).
151. Eyers, P.A., Erikson, E., Chen, L.G. & Maller, J.L. A Novel Mechanism for Activation of the Protein Kinase Aurora A. *Current Biology* **13**, 691-697 (2003).
152. Carter, S.L., Eklund, A.C., Kohane, I.S., Harris, L.N. & Szallasi, Z. A signature of chromosomal instability inferred from gene expression profiles predicts

clinical outcome in multiple human cancers. *Nature Genetics* **38**, 1043-1048 (2006).
153. Heidebrecht, H.J. *et al.* repp86: A human protein associated in the progression of mitosis. *Mol Cancer Res* **1**, 271-279 (2003).
154. Meraldi, P., Honda, R. & Nigg, E.A. Aurora-A overexpression reveals tetraploidization as a major route to centrosome amplification in p53-/- cells. *The EMBO journal* **21**, 483-492 (2002).
155. Cleveland, D.W., Mao, Y. & Sullivan, K.F. Centromeres and kinetochores: from epigenetics to mitotic checkpoint signaling. *Cell* **112**, 407-421 (2003).
156. Gascoigne, K.E. & Taylor, S.S. How do anti-mitotic drugs kill cancer cells? *Journal of Cell Science* **122**, 2579-2585 (2009).
157. Shannon, K.B., Canman, J.C. & Salmon, E.D. Mad2 and BubR1 function in a single checkpoint pathway that responds to a loss of tension. *Mol Biol Cell* **13**, 3706-3719 (2002).
158. Di Fiore, B., Wurzenberger, C., Davey, N.E. & Pines, J. The Mitotic Checkpoint Complex Requires an Evolutionary Conserved Cassette to Bind and Inhibit Active APC/C. *Molecular cell* **64**, 1144-1153 (2016).
159. Lara-Gonzalez, P., Westhorpe, Frederick G. & Taylor, Stephen S. The Spindle Assembly Checkpoint. *Current Biology* **22**, R966-R980 (2012).
160. Wertz, I.E. *et al.* Sensitivity to antitubulin chemotherapeutics is regulated by MCL1 and FBW7. *Nature* **471**, 110-114 (2011).
161. Darlyuk-Saadon, I. *et al.* Expression of a constitutively active p38α mutant in mice causes early death, anemia, and accumulation of immunosuppressive cells. *Febs j* **288**, 3978-3999 (2021).
162. Diskin, R., Askari, N., Capone, R., Engelberg, D. & Livnah, O. Active Mutants of the Human p38α Mitogen-activated Protein Kinase *. *Journal of Biological Chemistry* **279**, 47040-47049 (2004).
163. Tagscherer, K.E., Fassl, A., Sinkovic, T., Combs, S.E. & Roth, W. p53-dependent regulation of Mcl-1 contributes to synergistic cell death by ionizing radiation and the Bcl-2/Bcl-XL inhibitor ABT-737. *Apoptosis* **17**, 187-199 (2012).
164. Ha, G.-H. *et al.* p53 Activation in Response to Mitotic Spindle Damage Requires Signaling via BubR1-Mediated Phosphorylation. *Cancer Research* **67**, 7155-7164 (2007).
165. Gascoigne, K.E. & Taylor, S.S. How do anti-mitotic drugs kill cancer cells? *J Cell Sci* **122**, 2579-2585 (2009).
166. Brito, D.A. & Rieder, C.L. Mitotic Checkpoint Slippage in Humans Occurs via Cyclin B Destruction in the Presence of an Active Checkpoint. *Current Biology* **16**, 1194-1200 (2006).
167. Musacchio, A. The Molecular Biology of Spindle Assembly Checkpoint Signaling Dynamics. *Current Biology* **25**, R1002-R1018 (2015).
168. Zeng, X. & King, R.W. An APC/C inhibitor stabilizes cyclin B1 by prematurely terminating ubiquitination. *Nat Chem Biol* **8**, 383-392 (2012).

169. Zeng, X. *et al.* Pharmacologic Inhibition of the Anaphase-Promoting Complex Induces A Spindle Checkpoint-Dependent Mitotic Arrest in the Absence of Spindle Damage. *Cancer Cell* **18**, 382-395 (2010).
170. Chan, K.S., Koh, C.G. & Li, H.Y. Mitosis-targeted anti-cancer therapies: where they stand. *Cell Death & Disease* **3**, e411-e411 (2012).
171. van Vuuren, R.J., Visagie, M.H., Theron, A.E. & Joubert, A.M. Antimitotic drugs in the treatment of cancer. *Cancer Chemother Pharmacol* **76**, 1101-1112 (2015).
172. Untch, M. *et al.* Nab-paclitaxel versus solvent-based paclitaxel in neoadjuvant chemotherapy for early breast cancer (GeparSepto-GBG 69): a randomised, phase 3 trial. *Lancet Oncol* **17**, 345-356 (2016).
173. Yuan, P. *et al.* Eribulin mesilate versus vinorelbine in women with locally recurrent or metastatic breast cancer: A randomised clinical trial. *Eur J Cancer* **112**, 57-65 (2019).
174. Van den Bossche, J. *et al.* Spotlight on Volasertib: Preclinical and Clinical Evaluation of a Promising Plk1 Inhibitor. *Med Res Rev* **36**, 749-786 (2016).
175. Stadler, W.M. *et al.* An open-label, single-arm, phase 2 trial of the Polo-like kinase inhibitor volasertib (BI 6727) in patients with locally advanced or metastatic urothelial cancer. *Cancer* **120**, 976-982 (2014).
176. Pujade-Lauraine, E. *et al.* Volasertib Versus Chemotherapy in Platinum-Resistant or -Refractory Ovarian Cancer: A Randomized Phase II Groupe des Investigateurs Nationaux pour l'Etude des Cancers de l'Ovaire Study. *J Clin Oncol* **34**, 706-713 (2016).
177. Awada, A. *et al.* Phase I trial of volasertib, a Polo-like kinase inhibitor, plus platinum agents in solid tumors: safety, pharmacokinetics and activity. *Invest New Drugs* **33**, 611-620 (2015).
178. Machiels, J.P. *et al.* A phase I study of volasertib combined with afatinib, in advanced solid tumors. *Cancer Chemother Pharmacol* **76**, 843-851 (2015).
179. Nokihara, H. *et al.* Phase I trial of volasertib, a Polo-like kinase inhibitor, in Japanese patients with advanced solid tumors. *Invest New Drugs* **34**, 66-74 (2016).
180. Wang, C. *et al.* Inducing and exploiting vulnerabilities for the treatment of liver cancer. *Nature* **574**, 268-272 (2019).
181. Sakaue-Sawano, A. *et al.* Visualizing Spatiotemporal Dynamics of Multicellular Cell-Cycle Progression. *Cell* **132**, 487-498 (2008).
182. Chen, J. The Cell-Cycle Arrest and Apoptotic Functions of p53 in Tumor Initiation and Progression. *Cold Spring Harb Perspect Med* **6**, a026104-a026104 (2016).
183. Choudhary, A. *et al.* Interphase cytofission maintains genomic integrity of human cells after failed cytokinesis. *Proc Natl Acad Sci U S A* **110**, 13026-13031 (2013).
184. Herbst, R.S., Morgensztern, D. & Boshoff, C. The biology and management of non-small cell lung cancer. *Nature* **553**, 446-454 (2018).

185. Rudin, C.M., Brambilla, E., Faivre-Finn, C. & Sage, J. Small-cell lung cancer. *Nat Rev Dis Primers* **7**, 3 (2021).
186. Gazdar, A.F., Bunn, P.A. & Minna, J.D. Small-cell lung cancer: what we know, what we need to know and the path forward. *Nature Reviews Cancer* **17**, 725-737 (2017).
187. Bunn, P.A., Jr. *et al.* Small Cell Lung Cancer: Can Recent Advances in Biology and Molecular Biology Be Translated into Improved Outcomes? *J Thorac Oncol* **11**, 453-474 (2016).
188. Ahn, J. *et al.* Down-regulation of the stathmin/Op18 and FKBP25 genes following p53 induction. *Oncogene* **18**, 5954-5958 (1999).
189. Küntziger, T., Gavet, O., Sobel, A. & Bornens, M. Differential Effect of Two Stathmin/Op18 Phosphorylation Mutants on Xenopus Embryo Development *. *Journal of Biological Chemistry* **276**, 22979-22984 (2001).
190. Diamond, J.R. *et al.* Predictive biomarkers of sensitivity to the aurora and angiogenic kinase inhibitor ENMD-2076 in preclinical breast cancer models. *Clin Cancer Res* **19**, 291-303 (2013).
191. Adorno, M. *et al.* A Mutant-p53/Smad complex opposes p63 to empower TGFbeta-induced metastasis. *Cell* **137**, 87-98 (2009).
192. Zaika, A.I., Kovalev, S., Marchenko, N.D. & Moll, U.M. Overexpression of the Wild Type p73 Gene in Breast Cancer Tissues and Cell Lines. *Cancer Research* **59**, 3257-3263 (1999).
193. Levrero, M. *et al.* The p53/p63/p73 family of transcription factors: overlapping and distinct functions. *J Cell Sci* **113 (Pt 10)**, 1661-1670 (2000).
194. Ma, H.-l. *et al.* Stathmin is overexpressed and regulated by mutant p53 in oral squamous cell carcinoma. *Journal of Experimental & Clinical Cancer Research* **36**, 109 (2017).
195. Singer, S. *et al.* Protumorigenic overexpression of stathmin/Op18 by gain-of-function mutation in p53 in human hepatocarcinogenesis. *Hepatology* **46**, 759-768 (2007).
196. Sheu, J.C. *et al.* Growth rate of asymptomatic hepatocellular carcinoma and its clinical implications. *Gastroenterology* **89**, 259-266 (1985).
197. An, C. *et al.* Growth rate of early-stage hepatocellular carcinoma in patients with chronic liver disease. *Clin Mol Hepatol* **21**, 279-286 (2015).
198. Kim, J.K. *et al.* Tumor Volume Doubling Time as a Dynamic Prognostic Marker for Patients with Hepatocellular Carcinoma. *Digestive Diseases and Sciences* **62**, 2923-2931 (2017).
199. Nathani, P. *et al.* Hepatocellular carcinoma tumour volume doubling time: a systematic review and meta-analysis. *Gut* **70**, 401-407 (2021).
200. Pessina, A. *et al.* Prevalidation of a model for predicting acute neutropenia by colony forming unit granulocyte/macrophage (CFU-GM) assay. *Toxicol In Vitro* **15**, 729-740 (2001).
201. Pessina, A. *et al.* Application of the CFU-GM Assay to Predict Acute Drug-Induced Neutropenia: An International Blind Trial to Validate a Prediction Model

for the Maximum Tolerated Dose (MTD) of Myelosuppressive Xenobiotics. *Toxicological Sciences* **75**, 355-367 (2003).

202. Zanger, U.M. & Schwab, M. Cytochrome P450 enzymes in drug metabolism: Regulation of gene expression, enzyme activities, and impact of genetic variation. *Pharmacology & Therapeutics* **138**, 103-141 (2013).
203. Gradishar, W.J. *et al.* Phase III trial of nanoparticle albumin-bound paclitaxel compared with polyethylated castor oil-based paclitaxel in women with breast cancer. *J Clin Oncol* **23**, 7794-7803 (2005).
204. Lee, H. *et al.* Efficacy and safety of nanoparticle-albumin-bound paclitaxel compared with solvent-based taxanes for metastatic breast cancer: A meta-analysis. *Scientific Reports* **10**, 530 (2020).
205. Guan, Z.-Z. *et al.* Superior efficacy of a Cremophor-free albumin-bound paclitaxel compared with solvent-based paclitaxel in Chinese patients with metastatic breast cancer. *Asia-Pacific Journal of Clinical Oncology* **5**, 165-174 (2009).
206. Gradishar, W.J. *et al.* Significantly Longer Progression-Free Survival With nab-Paclitaxel Compared With Docetaxel As First-Line Therapy for Metastatic Breast Cancer. *Journal of Clinical Oncology* **27**, 3611-3619 (2009).
207. Gradishar, W.J. *et al.* Phase II trial of nab-paclitaxel compared with docetaxel as first-line chemotherapy in patients with metastatic breast cancer: final analysis of overall survival. *Clin Breast Cancer* **12**, 313-321 (2012).
208. Desai, N. *et al.* Increased antitumor activity, intratumor paclitaxel concentrations, and endothelial cell transport of cremophor-free, albumin-bound paclitaxel, ABI-007, compared with cremophor-based paclitaxel. *Clin Cancer Res* **12**, 1317-1324 (2006).
209. Desai, N., Trieu, V., Damascelli, B. & Soon-Shiong, P. SPARC Expression Correlates with Tumor Response to Albumin-Bound Paclitaxel in Head and Neck Cancer Patients. *Transl Oncol* **2**, 59-64 (2009).
210. Simionescu, M., Gafencu, A. & Antohe, F. Transcytosis of plasma macromolecules in endothelial cells: a cell biological survey. *Microsc Res Tech* **57**, 269-288 (2002).
211. John, T.A., Vogel, S.M., Tiruppathi, C., Malik, A.B. & Minshall, R.D. Quantitative analysis of albumin uptake and transport in the rat microvessel endothelial monolayer. *Am J Physiol Lung Cell Mol Physiol* **284**, L187-196 (2003).
212. Rudalska, R. *et al.* In vivo RNAi screening identifies a mechanism of sorafenib resistance in liver cancer. *Nat Med* **20**, 1138-1146 (2014).
213. Seehawer, M. *et al.* Necroptosis microenvironment directs lineage commitment in liver cancer. *Nature* **562**, 69-75 (2018).
214. Bell, J.B. *et al.* Preferential delivery of the Sleeping Beauty transposon system to livers of mice by hydrodynamic injection. *Nat Protoc* **2**, 3153-3165 (2007).